Implications of Permeability Uncertainty During Three-phase CO_2 Flow in a Basalt Fracture Network

Alec Owen Gierzynski

Thesis submitted to the faculty of the Virginia Polytechnic Institute and State University in partial fulfillment of the requirements for the degree of

Master of Science
In
Geosciences

Ryan M. Pollyea
Madeline E. Schreiber
Robert P. Lowell

6 December 2016
Blacksburg, Virginia

Keywords: Basalt, fracture permeability, TOUGH3, ECO2M, Geologic Carbon Sequestration

Implications of Permeability Uncertainty During Three-phase CO_2 Flow in a Basalt Fracture Network

Alec Owen Gierzynski

ABSTRACT

Recent studies suggest that continental flood basalts may be suitable for geologic carbon sequestration due to fluid-rock reactions that mineralize injected CO_2 on relatively short time-scales. Flood basalts also possess a permeability structure favorable for injection, with alternating high-permeability (flow margin) and low-permeability (flow interior) layers. However, little information exists on the behavior of CO_2 as it leaks through fractures characteristic of the flow interior, particularly at conditions near the critical point for CO_2. In this study, a two-dimensional 5 × 5 m model of a fracture network is built based on high-resolution LiDAR scans of a Columbia River Basalt flow interior taken near Starbuck, WA. Three-phase CO_2 flow is simulated using TOUGH3 (beta) with equation of state ECO2M for 10 years simulation time. Initial conditions comprise a hydrostatic pressure profile corresponding to 750-755 m below ground surface and a constant temperature of 32° C. Under these conditions, the critical point for CO_2 occurs 1.5 meters above the bottom of the domain. Matrix permeability is assumed to be constant, based on literature values for the Columbia River Basalt. Fracture permeability is assigned based on a lognormal distribution of random values with mean and standard deviation based on measured fracture aperture values and *in situ* permeability values from literature. In order to account for fracture permeability uncertainty, CO_2 leakage is simulated in 50 equally probable realizations of the same fracture network with spatially random permeability constrained by the lognormal permeability distribution. Results suggest that fracture permeability uncertainty has some effect on the distribution of CO_2 within the fractures, but network geometry is the primary control in determining flow paths. Fracture permeability uncertainty has a larger influence on fluid pressure, and can affect the location of the critical point within ~1.5 m. Uncertainty in fluid pressure was found to be highest along major flow paths below channel constrictions, indicating permeability at a few key points can have a large influence on fluid pressure distribution.

Implications of Permeability Uncertainty During Three-phase CO_2 Flow in a Basalt Fracture Network

Alec Owen Gierzynski

GENERAL AUDIENCE ABSTRACT

Geologic carbon sequestration (GCS) is a means of reducing greenhouse gas emissions using currently available technology. It consists of trapping carbon dioxide (CO_2) released by the burning of fossil fuels at a large emitter, such as a coal fired power plant, and injecting it deep beneath the earth's surface for permanent storage. This research builds on an increasing body of evidence that suggests that the Columbia River Basalt Group (GRBG), a large lava formation located in the northwestern United States, may be a suitable target for GCS. This is largely because CO_2 reacts with basalt rocks within a few years of injection to form stable minerals, after which it is permanently immobilized. This basalt province also contains alternating layers of rock, some of which have high permeability, meaning that they can accept CO_2 injections, and some of which have low permeability, meaning that they would block CO_2 rising from the injection layers. Layers with low permeability are called confining layers, and in the CRBG, they contain fractures that formed when the lava initially cooled. While some information about these fractures is known, it is impossible to know how easily fluid might flow through them at any given point (permeability) at the depths of interest for GCS. This study seeks to quantify the effects of that uncertainty, by building a model of CO_2 flow through a CRBG fracture set, and running that same model 50 times with all variables held constant, except the exact location of permeability values within the fracture network. Chemical reactions are not considered, so this model represents behavior in the network very soon after CO_2 is injected, before minerals start to form. The results of this model suggest that uncertainty in permeability values within fractures influences predictions of fluid pressure within the confining layer. This is important, because fluid pressure has a large influence on whether or not CO_2 will leak through the confining layer. This research will be useful in informing the model design of future researchers attempting to simulate GCS efforts in the CRBG and similar geologic formations.

Acknowledgements

This work was supported by the U.S. Department of Energy National Energy Technology Laboratory through cooperative agreement DE-FE0023381. Additional funding was provided by the Geological Society of America Student Research Grant. Thank you to my committee, Madeline Schreiber, and Bob Lowell. Thank you to Ryan Pollyea, for guiding me through this process and believing in me. Special thanks to Diana Strode, who sparked my interest in hydrogeology and set me going on this journey.

Table of Contents

List of Figures

List of Tables

CHAPTER 1: INTRODUCTION

Introduction

The Columbia River Basalt Group (CRBG) in the Pacific Northwest is among the best-studied continental flood basalt provinces on Earth. It was the focus of intensive research in the 1980's, as the United States Department of Energy worked to evaluate its suitability for a nuclear waste repository (Thorne and Spane 1985, Strait et al 1982, Gephart et al 1983). The waste repository project was eventually abandoned, but the research done in the area did much to advance knowledge on flow and contaminant transport in fractured rocks. Today, interest in the CRBG continues due to its importance to regional aquifers (Burns et al 2010, Kahle et al 2011, Burns et al 2012), and geologic carbon sequestration (GCS) in basalt (McGrail et al., 2006).

With climate change looming as a major threat to global stability and food supplies, it is essential to explore all options for curtailing anthropogenic CO_2 emissions. Although a complete transition from fossil fuels to clean energy is ideal, such a transition will not occur rapidly enough to avoid dangerous threshold values of atmospheric CO_2 (IEA 2012). As such, the process of GCS offers an intermediate option, in which large amounts of waste CO_2 are safely stored using technology currently in use for enhanced oil recovery (Pascala and Socalow 2004). In GCS, CO_2 emissions are captured from large point source emitters, such as coal fired power plants, and permanently stored in deep geologic formations. This practice could considerably curtail greenhouse gas emissions, since coal is still a major source of energy globally. For example, in 2010-2011, India's coal plants accounted for about 66% of its generated electricity, emitting approximately 665 million tons of CO_2 (Guttikunda and Jawahar 2014). In 2009, United States coal plants emitted about 36% of the total CO_2 output, and in China, coal accounted for around 82% of carbon emissions (Bacon et al 2014). In addition to storing CO_2 generated by coal plants, GCS could be implemented in the manufacturing sector, e.g., fertilizer plants (Kapila and Haszeldine 2009), and even at biomass-burning power plants (McGrail et al 2010). In 2012, the International Energy Agency found that GCS could potentially reduce global carbon emissions by as much as 20% by 2050 (IEA 2012). Due to cost, implementation of this technology is not currently widespread; however, the United States Department of Energy estimates that the United States could store up to 3,000 megatons of CO_2, 500 times the amount created annually by energy production, in deep saline aquifers using only existing technologies (USGS 2013).

Conventional geologic reservoirs for GCS comprise carbonate or siliciclastic formations, often spent oil and natural gas reservoirs. In these types of reservoirs, CO_2 isolation occurs by physical mechanisms, such as capillary and/or residual trapping, and permanent mineralization takes anywhere from hundreds to thousands of years (Bachu 2008). Unfortunately, while CO_2 trapped in such reservoirs is relatively secure, leakage due to a seismic event or slow leakage through some discontinuity in a caprock layer will always be a risk as long as CO_2 remains a free phase, i.e. not dissolved in water or fixed in mineral form (Zoback and Gorelick 2012). One potential alternative to such traditional targets is to inject the CO_2 into continental flood basalt (CFB) formations, which have the requisite physical structure (i.e., zones of high and low permeability) for GCS, as well as one additional advantage – basaltic glass and minerals react quickly with CO_2 to form stable carbonate minerals (McGrail et al 2006). Much research has gone into exploration of CFB's as potential CO_2 storage reservoirs, with particular emphasis on basalt chemistry (McGrail et al 2006, Prasad et al 2009, Schaef et al 2011, Rosenbauer et al 2012, Aradóttir et al 2012a, Aradóttir et al 2012b, McGrail et al 2014, Bacon et al 2014). However, reactive chemistry in basalt does not instantaneously immobilize all CO_2 (Matter et al 2016). More study is therefore required of CO_2 leakage through confining layers in the basalt at time-scales for which geochemical reactions are not the dominant trapping process, i.e., < 10 yr.

Numerical models provide a means of studying such phenomena, by simulating conditions where direct observation is impossible. Faybishenko et al (2001) proposed a hierarchy of scales for studying fluid flow in fractured basalt formations – elemental scale models include a single element, such as one fracture or a block of homogeneous media; small-scale models include one or a few fractures plus matrix; medium scale models represent a single basalt flow, with fractures and other features; and finally, large-scale models represent multiple basalt flows with the surrounding network of rubble zones and sedimentary layers. This hierarchy is necessary because fluid-flow in variably saturated fractured media behaves differently at different scales. The goal of this research is to investigate the effects of uncertainty in the spatial distribution of fracture permeability defined over Faybishenko's "small" scale, using 5×5 meter maps of fractures from basalt flow interiors in the Columbia River Basalt Group in the northwestern United States. A small-scale experiment is the most useful for exploring this type of uncertainty, as it allows investigation of the effects of uncertainty on CO_2 fluxes and fluid pressure on a scale relevant to individual leakage pathways. Effects of uncertainty on fluid

pressure are of particular interest in this research, since the simulation is set near the critical pressure for CO_2, where CO_2 injected as a sub-critical liquid will undergo phase change to a sub-critical liquid, and then gas phase. CO_2 leakage through fractures can depend strongly on its phase, since CO_2 expands as it transitions to gas, and different phases have different capillary entry pressure. A small-scale experiment also has the potential of producing scalable results – if spatial uncertainty seems to have little or no discernable effect on fluid fluxes, then the equivalent porous media approximation may be justified over the model length scale. Previous research in the field, however, suggests that uncertainty concerning fluid flow through a fracture due to spatially variable permeability distributions can be significant (Klimczak et al 2009, Kwicklis and Healy 1993). The simulations conducted in this thesis endeavor to account for that uncertainty.

Research Objectives

This study develops a numerical modeling experiment to explore how spatial uncertainty in fracture permeability can influence predictions of CO_2 migration through an outcrop-scale basalt network. Outcrop-scale fracture network models are developed on the basis of LiDAR scan data from a road cut CRBG exposure in southeast Washington State. In order to study the effects of spatial uncertainty in fracture permeability, a Monte Carlo simulation strategy is implemented such that the fracture network is constant for each simulation; however, fracture permeability is spatially random while reproducing a lognormal permeability distribution from the literature. Results from this study will provide insights into the behavior of CO_2 leakage through a basalt flow interior when the permeability distribution is constant, but the corresponding spatial distribution is randomly generated, i.e., maximum spatial uncertainty.

CO_2 Phases in Geologic Carbon Sequestration

In order to understand the physical processes modeled in this simulation, it is necessary to first understand some properties of the fluids involved. As such, this section provides a brief overview of the phases of CO_2 as they are related to GCS.

Figure 1 consists of a phase diagram depicting all phases in which CO_2 can occur between 0 and 100 MPa, and between -80 and 80 °C. In this temperature and pressure range, CO_2 may be a solid, liquid, vapor, or super-critical liquid (Marini 2007). During GCS, CO_2

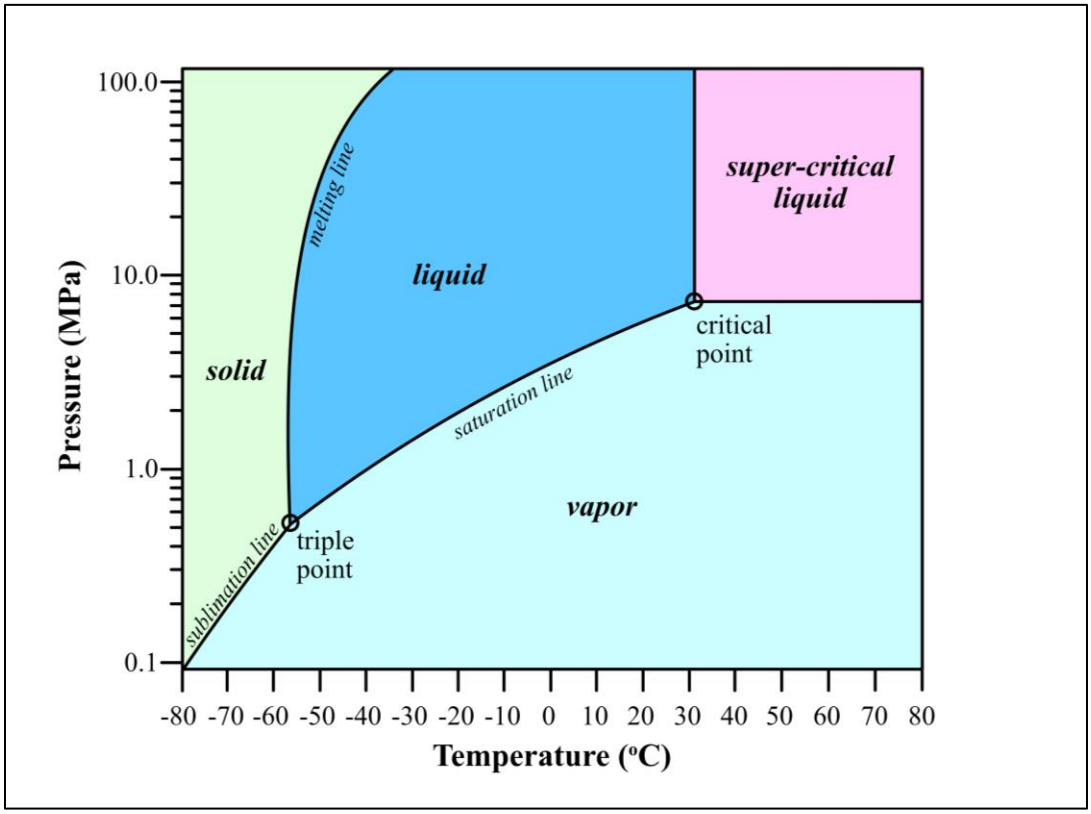

Figure 1: *Phase diagram for CO_2 at temperatures from -80 to 80 °C and pressure between 0.1 and 100.0 MPa, modified from Marini (2007). Triple point occurs at approximately -56.6 °C, 0.518 MPa, critical point occurs at approximately 31.1 °C, 7.39 MPa.*

trapped at an emission source is compressed to a super-critical liquid form, which requires temperatures above 31.1 °C, and pressures above 7.39 MPa (Edlmann et al 2012). Since the super-critical form is denser than the liquid or gas form, this minimizes CO_2 volume during storage, transportation, and injection. Super-critical CO_2 is then injected at depths where temperature and pressure are above the critical point (Schaef et al 2011). Once injected, it begins to rise buoyantly due to the density contrast between super-critical CO_2 and formation brines (Pruess 2005). Should CO_2 rise high enough, it may reach pressures lower than the critical point, at which point it will expand to subcritical liquid, and finally boil to a vapor phase. The presence of such a phase transition will increase pressure in the surrounding rock due to the expansion of the liquid, and decrease temperature as boiling CO_2 absorbs heat (Pruess 2005). This can result in the phase transition zone growing thicker and shallower with time, and can impede upwardly mobile CO_2 (Pruess 2005). Different phases of CO_2 also behave differently as they travel

through formation materials – for example, Edlmann et al (2012) found that vapor phase CO_2 entered fractures in a shale sample, while super-critical phase CO_2 could not.

In addition to injecting CO_2 in a super-critical phase, it is possible to first mix CO_2 with water, and then inject it as an aqueous phase into a geologic formation. This is not usually done, because it is very water-intensive, and CO_2 makes up only a small fraction of the mass being injected with this method (Gislason et al 2014). However, the Carbfix project in Iceland has successfully tested this method in basalt rocks, arguing that dissolving CO_2 in water has the advantage both of negating the buoyancy effects of injecting super-critical CO_2, and increasing reactivity between CO_2 and formation rocks (Aradóttir et al 2012). Other projects involving injection into basalt focus on the injection of super-critical liquid CO_2, which does not require large volumes of water (McGrail et al 2006, 2009, 2010, 2014, 2016).

Geologic Carbon Sequestration

Despite its simple premise, GCS is technically a very complicated process. In order to explore how CO_2 might be permanently stored underground, this section reviews first the types of formations typically targeted for GCS, then the properties required for permanent storage, and finally the types of permanent storage important to GCS.

Target reservoirs for GCS traditionally include deep saline aquifers and spent oilfields comprised either of siliciclastic or carbonate rocks (Bachu 2008). These types of reservoirs have the advantages of known, often extensively studied, physical properties and little utility for any other purpose. They also tend to meet the three requirements that define a suitable GCS reservoir – capacity, injectivity, and confinement (Bachu 2008). That is, they are large, their permeability is adequate to allow sustained injection without pressure buildup near the source, and CO_2 cannot escape the formation once injected. The last of these three requirements, confinement, warrants some further discussion, as it involves multiple interacting confinement mechanisms. The first of these is 'buoyant trapping', where CO_2 in a porous formation is trapped beneath an impermeable cap-rock layer, such as shale, and is unable to flow through it (USGS 2013). Most cap-rocks are bound to have some kind of discontinuity, however, such as an old well, a fault, joints, etc. Therefore buoyant trapping by itself is insufficient to ensure permanent storage, and other mechanisms within the injection formation are required to hold CO_2 in place. These mechanisms comprise three additional forms of permanent trapping: residual trapping,

dissolution of CO_2 in brine, and mineralization (Kumar et al 2004). Residual trapping, also known as capillary trapping, occurs when CO_2 is trapped within the pores as irreducible saturation due to an inability to overcome the capillary entry pressure, and is thus unable to move upward in a formation (Bachu and Bennion 2008). In deep saline formations, capillary trapping tends to be the primary permanent trapping mechanism, and depends on relative permeability, pore size distribution, and interfacial tension (Bachu and Bennion 2008). The second form of permanent trapping, dissolution of CO_2 into brine, depends largely on the salinity of the brine, and tends to be a relatively minor component of storage. Similarly, the final permanent trapping mechanism, mineralization, will proceed very slowly in silicate or carbonate GCS reservoirs, on the order of centuries to millennia (Bachu 2008). Matrix diffusion (Carniero 2009) in fractured media, and surface adsorption, especially with injection into coals and clays (Bachu 2008) are also potential trapping mechanisms, though in most cases less important. With all of these mechanisms in play, much discussion surrounds the relative importance of various factors in determining the likelihood of leakage. Hou and Rockold (2011) performed quasi-Monte Carlo simulations to test the impact of several properties on leakage, finding that in order of importance, the most important factors in assessing leakage potential are caprock thickness, caprock permeability, reservoir permeability, caprock porosity, and reservoir porosity. Similarly, Pollyea (2016) deployed response surface analysis to quantify reservoir performance as a function of relative permeability model parameters. By systematically varying the residual gas saturation and phase interference parameters used in the van Genuchten equations for calculating relative permeability, Pollyea (2016) found that in the modeled homogenous sandstone reservoir, aqueous phase mobility strongly governed reservoir pressure accumulation, while CO_2 mobility was the primary control on plume geometry.

Geologic Carbon Sequestration in Basalt

This section offers a detailed analysis of the process of GCS in continental flood basalts. It begins with a review of the chemical trapping potential of CFB's, followed by a discussion of the physical trapping mechanisms available for containing CO_2 in basalt formations, then concludes with a brief discussion of current pilot-scale GCS projects in basalt.

McGrail et al (2006) first proposed GCS in flood basalt reservoirs on the basis of laboratory experiments showing rapid mineralization rates. The CRBG is high in calcium,

magnesium, and iron, due to the abundance of plagioglase, pyroxene, and olivine (McGrail et al 2006). These cations are crucial to the mineralization of CO_2 upon injection into basalt, which proceeds in the following steps, after McGrail et al (2006):

$$CO_2(g) \overset{K_h}{\leftrightarrow} CO_2(aq) \quad (1)$$

$$CO_2(aq) \overset{K_1}{\leftrightarrow} HCO_3^- + H^+ \quad (2)$$

$$Na_x(Ca,Mg,Fe)_ySi_3AlO_8 + (x+2y+3)H^+ + 4H_2O \overset{K_2}{\rightarrow} \quad (3)$$
$$xNa^+ + y(Ca,Mg,Fe)^{2+} + 3H_4SiO_4(aq) + Al^{3+}$$

$$(Ca,Mg,Fe)^{2+} + HCO_3^- \overset{K_3}{\leftrightarrow} (Ca,Mg,Fe)CO_3 + H^+ \quad (4)$$

In Equation 1, free-phase CO_2 dissolves into formation water, forming carbonic acid; in Equation 2, carbonic acid dissociates into bicarbonate ion and hydrogen; in Equation 3, the hydrogen is consumed by mineral dissolution, releasing, among other things, Ca^{+2}, Mg^{+2}, or Fe^{+2} cations; in Equation 4, the divalent cations released in Equation 3 react with bicarbonate ion to form a carbonate mineral and a hydrogen ion. The carbonate mineral is now stable, and further release of hydrogen drives continued dissolution of feldspar, pyroxene, or olivine. McGrail et al (2006) demonstrated that these reactions occur at room temperature, in a lab setting. Schaef et al (2011) expanded on those results, performing experiments at higher temperatures and pressures more consistent with GCS conditions. Experimenting with both aqueous and supercritical CO_2, they found that rocks exposed to wet supercritical CO_2 at the high temperatures and pressures (greater than 96 ˚C and greater than 21 MPa) showed the most evidence of mineralization (Schaef et al 2011). Geochemical reactions between CO_2 and basalt have also been tested in the field. Matter et al (2007), for example, evaluated the interactions between aqueous CO_2 and basalt using a single well push-pull test in which aqueous CO_2 was injected, allowed to sit, then pumped back out. They found that, as predicted by Equations 1-4, water pumped from the well after injection contained elevated cation concentrations, a sign that mineral dissolution occurred. These chemical reactions result in much higher rates of mineral trapping of CO_2 than conventional GCS targets, such as silicate and carbonate rocks (Van Pham et al 2012).

Clearly, basaltic rocks are chemically very favorable for GCS. However, in order to be suitable for widespread GCS, a continental flood basalt formation must possess a physical structure capable of both accepting and storing CO_2 – i.e., it must meet the physical requirements of capacity, injectivity, and confinement discussed by Bachu (2008). These requisite physical

properties are met by the CRBG because of the size of the province and the structure of its constituent lava flows. The CRBG covers approximately 210,000 km^2 over parts of four states (Figure 2), with an estimated volume of 210,000 km^3 (Reidel 2015). This impressive size reflects the eruptive history of the basalt, where lava flows of up to 1000 km^3 poured out of a series of fissures from 16.7 to 5 Ma (Reidel 2015). Interflow structures within these lava flows define the injectivity and confinement within the CRBG. Figure 3 depicts these structures as they would appear in an idealized basalt column: from bottom to top, flow bottom, lower colonnade, entablature, upper colonnade, and flow margin (Long and Wood 1986). Disregarding the flow bottom, which is usually relatively thin, these features can be divided into two hydrogeologic zones, the flow margin and the flow interior. The flow margin is vesicular and often rubbly, occupying the upper 10-20% of the flow (Reidel 2013). Depending on the size of the flow, a single flow margin can extend for thousands of square kilometers horizontally (Gephart 1983). Many of these large, porous features together serve as regional aquifers (Burns et al 2010, Kahle et al 2011, Burns et al 2012). Permeability values for these features are on the order of 1.00E-07 m^2 (Burns et al 2012) to 1.00E-14 m^2 (McGrail et al 2009). Where lithostatic pressure is greater than the critical threshold for CO_2 and water is not potable, such layers represent ideal injection targets for GCS (McGrail et al 2006). The other hydrogeologic zone of the basalt flow is the flow interior, comprising the upper colonnade, the entablature, and the lower colonnade. This composite zone consists of dense, fractured basalt (Long and Wood 1986, Reidel 2015). The flow interior functions as a confining layer, with effective permeability between 1.00E-15 (Khaleel 1989) and 1.00E-21 m^2 (McGrail et al 2009), and geometric mean permeability around 1.00E-18 m^2. In aggregate, the CRBG comprises many individual lava flows of various sizes, each of which contain some version of these interflow structures – the end result of which is an irregular stack of alternating high and low permeability layers. This structure is highly conducive to physical trapping of CO_2. As discussed in Ambrose et al (2008), anisotropy in the form of layered systems leads to better trapping, because it forces horizontal migration and increases contact between CO_2 and reservoir materials. Therefore CO_2 will be forced horizontally in an injection layer along an impermeable caprock, which will increase buoyancy trapping, as well as reactive surface area for mineralization reactions.

Recent investigators estimate that the Columbia River Basalt Group (CRBG) alone could hold up to 100 Gt of CO_2, based on aerial extent, thickness, and estimates of porosity and

permeability for suitable injection layers (McGrail et al 2009). The Deccan basalts in India could potentially hold even more, covering an area over twice the size of the CRBG (Sullivan et al 2011), with chemistry similarly suitable to GCS (Prasad et al 2009). There are also continental flood basalt provinces in South America, Africa, and Siberia, each in turn capable of holding large amounts of CO_2 (Takaya et al 2013). Despite all of this potential storage volume, only a few pilot-scale injection projects are currently underway in basaltic rocks. One such project is currently underway at the Hellisheidi geothermal field in Iceland. Known as CarbFix, this project proposes permanent storage of CO_2 in basalt, through a process in which CO_2 is dissolved in water prior to injection beneath the surface (Aradóttir et al 2012a, Aradóttir et al 2012b, Gislason et al 2014, Matter et al 2016). As proof of concept, CarbFix conducted a test injection in 2012, and from subsequent analyses report up to 95% mineralization of injected CO_2 (Matter et al 2016). Similarly encouraging results are also emerging from a pilot-scale GCS project in the Columbia River Basalt Group – in 2013, McGrail and others performed a test injection of 1000 Mt of super-critical CO_2 into CRBG basalts at a site near Wallula, Washington (McGrail et al 2014). Site monitoring has shown no evidence of CO_2 leakage, and down-hole water sampling confirmed the dissolution of basalt, which is a pre-requisite to CO_2 mineralization (McGrail et al 2014). Further analysis of drill cores taken near the injection well revealed widespread evidence of carbonate mineralization at the injection site, indicating chemical trapping mechanisms are performing exactly as expected (McGrail et al 2016).

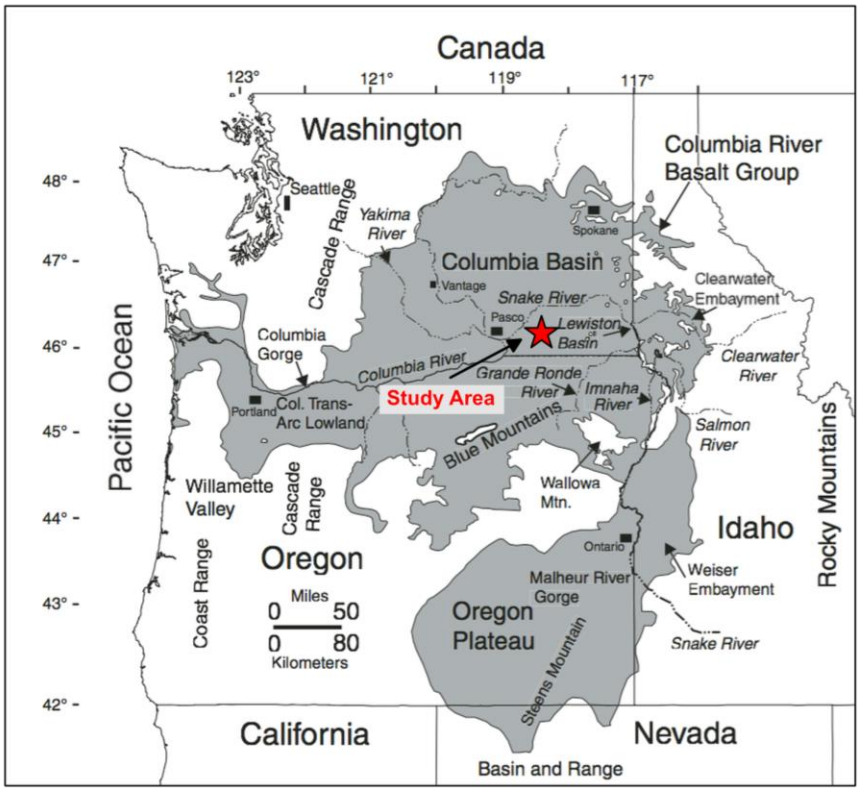

Figure 2: *Aerial extent of the Columbia River Basalt Group, after Reidel et al (2013).*

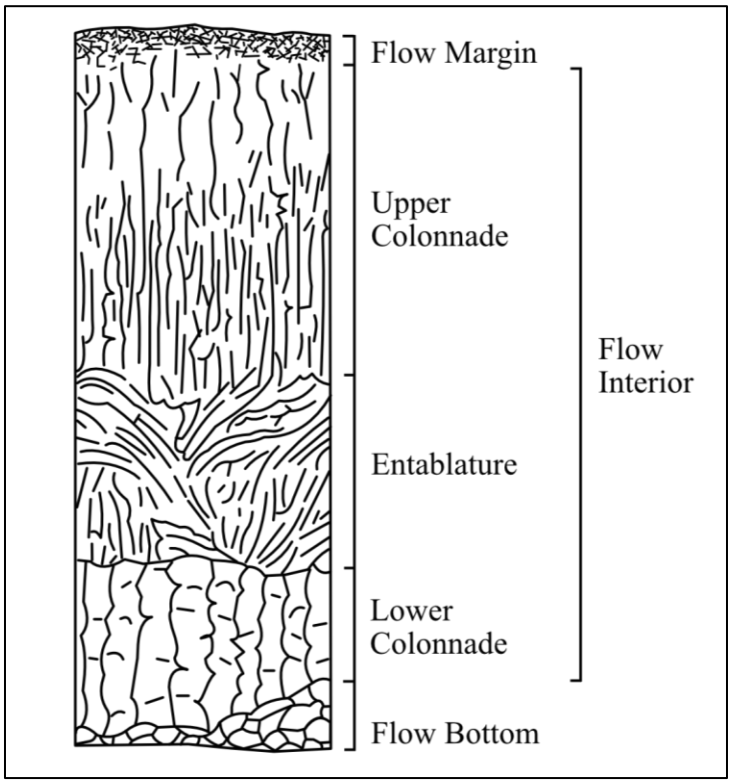

Figure 3: *Intraflow structures of the Columbia River Basalt Group, after Long and Wood (1986).*

Geologic Setting

The geologic setting for this research is the Columbia River Basalt Group, located in the northwestern United States (Figure 2). The CRBG is the world's youngest and smallest flood basalt province, covering approximately 210,000 km^2 in four states, with a volume around 210,000 km^3 (Reidel 2015). The maximum thickness of the CRBG is over 4 km, occurring near the center of the Columbia Basin (Reidel et al 2013). Emplacement of the CRBG began 17.5 Ma, continuing through about 6 Ma (Vye-Brown et al 2011). In total, the CRBG comprises seven members – in stratigraphic order, the Steens Basalt, followed by the Imnaha, the Grande Ronde, Picture Gorge, Prineville, Wanupam, and Saddle Mountains Basalts (Figure 4). These members together include over 350 individual basalt flows, most of which formed by inflation as massive sheet flows (Reidel et al 2013). Inflation is the process by which liquid lava is continually injected into a lobe, after the outer surface has cooled or begun to cool, meaning that the youngest lava is at the center of the flow (Vye-Brown et al 2011). These flows travelled as many as hundreds of kilometers from their sources in as little as six years, with liquid lava travelling beneath the cooled outer crust at even faster rates (Reidel 2015). Composition of the CRBG is generally tholeiitic basalt to basaltic andesite and andesite, with common plagioclase (Ramos 2005). Flows tend to be fine-grained and lack large crystals, with few exceptions (Reidel et al 2013). The main eruptive phase of the CRBG consists of the Steens, Imnaha, and Grande Ronde Basalts, which erupted over the course of 1 Ma, and comprise 94% of the volume of the CRBG (Reidel 2015). The Grande Ronde is the largest of these members, making up 74% of the total volume (Reidel 2015). Individual flows from the Grande Ronde formation often exceed 1000 km^3 in volume (Reidel 2015). The Grande Ronde is primarily basaltic andesite, with 52-57 wt% silica, and 3-6% MgO (Durand 2014).

The main eruptive phase of the CRBG erupted from the Chief Joseph dike swarm, which is generally north trending (Reidel et al 2013). The location of the feeder dikes changed with time, however, beginning further to the south and migrating north (Reidel et al 2013). Recent studies suggest that Columbia River Basalt volcanism was caused by distortion of the Yellowstone hotspot plume head against the Precambrian margin of North America (Camp 1995). The migration of the feeder dykes is therefore likely due to the migration of the North American Plate with respect to the plume head (Camp 1995). The setting for the eruptions is the area of back arc extension between the Cascades and the Rockies (Reidel et al 2013). The

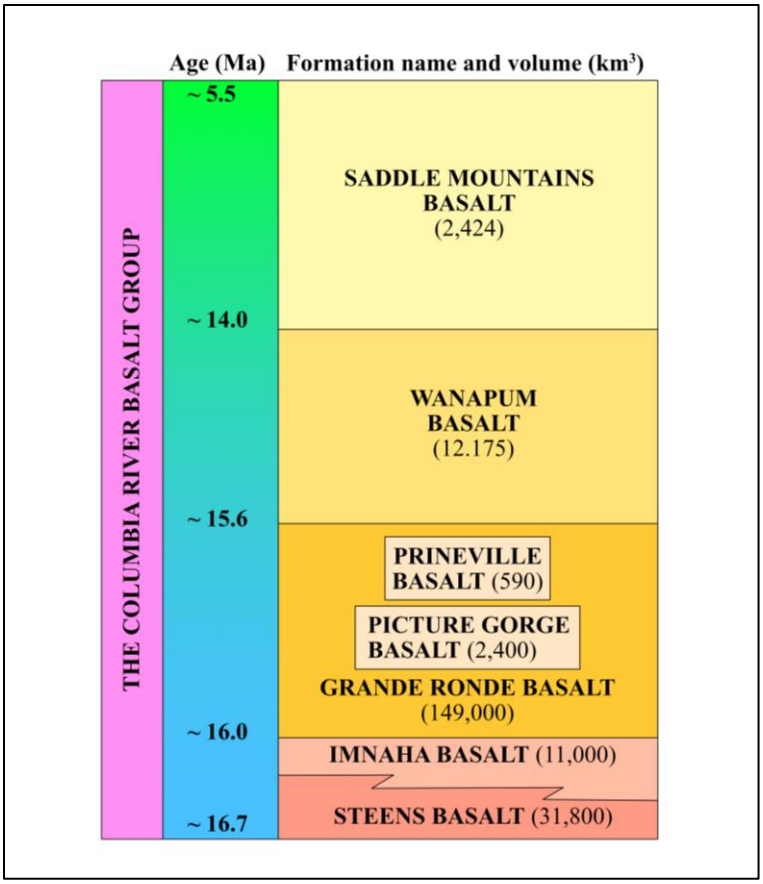

Figure 4: *Stratigraphic column of the Columbia River Basalt Group, after Reidel (2015)*

beginning of flood basalt volcanism in the region, the Steens Basalt, occurred in the projected location of the Yellowstone hot spot at the time of eruption (Hooper 2002). It forms a coherent isotopic group with the Grande Ronde and Imnaha basalts, suggesting that they are all formed from the same initial lava with various amounts of melted crust included (Ramos 2005). Major element, trace element, and isotopic studies show that the plume melted multiple sources, resulting in different bulk properties for members in the formation – different members include remnants of multiple crustal lithologies, plume material, and depleted and enriched mantle (Ramos 2005). Despite these different melt sources, individual members of the CRBG show a bulk geochemical homogeneity that has allowed for fairly accurate stratigraphy (Reidel 2015). In the current tectonic regime, the CRBG is situated in a zone of seismic stability, several hundred kilometers east of the North American plate margin (McGrail et al 2006). Sparse, randomly occurring magnitude 1-2 earthquakes occasionally occur at random across the CRBG, but do not affect aquifer isolation (McGrail et al 2006).

Columbia River Basalt Intraflow Structures

Columbia River Basalt Group flows contain intraflow structures that exert a strong influence on hydrogeology of the formation. Intraflow structures are internal features of a basalt flow, which form during emplacement through cooling, degassing, and interactions with the paleoenvironment (Reidel et al 2013). Generalized intraflow structures are illustrated in Figure 3. These structures include the flow margin, which is vesicular and often rubbly, comprising 10-20% of the flow, and the flow interior, which is dense and fractured, comprising the remainder of the flow (Reidel et al 2013). Flow tops consist either of vesicular basalt or flow-top breccia, which is made up of of angular fragments of vesicular basalt overlying non-fragmented vesicular basalt (Reidel et al 2013). Where present, flow-margin breccia may be highly extensive, up to 30 meters thick (Reidel et al 2013). Flow margins form zones of high permeability and porosity, and sometimes serve as important aquifers. The flow interior, in turn, consists of some combination of upper colonnade and lower colonnade, which have regular, orthogonal fractures, and the entablature, which has fanning, highly irregular fractures (Long and Wood 1986). Where colonnade and entablature are present, the colonnade makes up the lower 10-30 and upper 10-20% of the flow, and the entablature comprises the inner 60-70% of the flow (Long and Wood 1986). A flow bottom may be present as well, which generally consists of pillow basalt or slightly vesicular, rubbly basalt depending on whether the flow was extruded subaqueously (resulting in pillows) or subaerially (resulting in rubble) (Reidel 2013). Flow margins form during emplacement as a result of inflationary flow, as cooling vesicular basalts at the surface of a flow are continually broken up and rafted by the expanding lava beneath (Reidel 2013). Colonnade fractures form by thermal contraction as the flow slowly cools from the outside inward (Long and Wood 1986). Entablature-type fractures in the flow interior are formed as ponded lava flows at topographic lows are inundated by floodwaters during the deranged drainage regime caused by erupted lava (Long and Wood 1986). Water entering a cooling flow through colonnade-type cooling joints reaches the center of the flow, quenching the rock and forming fanning, irregular fractures (Long and Wood 1986). This is supported by petrographic textures – the entablature tends to have more evidence of quenching, such as glassy mesostasis (Long 1978). Flow interiors tend to act as aquicludes, due to their dense, non-vesicular matrix and tight fractures.

Permeability of Fractured Basalt

The goal of this research is to investigate the effect of spatial variation of permeability on the flow of CO_2 through fractured basalt. It is therefore instructive to assess previous methods that have been used to quantify fracture permeability at a variety of scales. The following section summarizes several studies of permeability at scales relevant to this research, from large-scale studies in similar rock types to small-scale studies that investigate flow at the scale of individual fractures.

Over the last few decades, fluid flow in fractured basalt has garnered significant attention for its relevance to contaminant transport at several sites. One such site is the Idaho National Engineering and Environmental Laboratory, situated in the Snake River Plane basalt, a low-volume flood basalt formation with a layered structure similar to the CRBG (Unger et al 2004). Two such studies useful to this research are Benito et al (1999), and Doughty (2000). Benito et al (1999) performed cross-well air injection tests to quantify the pneumatic conductivity of the basalt formation, finding that flow within unsaturated basalt exhibited strongly non-linear behavior, and that connectivity was good within a unit, but not across rubble zones separating basalt flows. This is relevant to the present study, since it indicates good horizontal connectivity within a permeable unit, but poor vertical connectivity across flow interiors, which is desirable for GCS in basalt. Additionally, non-linear flow behavior within an unsaturated formation indicates complicated flow conditions, which this thesis seeks to simulate. Doughty (2000) performed numerical simulations of infiltration tests performed in the Snake River Plain basalt at the outcrop scale. To represent the fractured basalt, the author traced fractures from a cliff face at Box Canyon, and overlaid them onto a TOUGH2 grid (Doughty 2000). In these simulations, fracture permeability was anisotropic and varied across fracture type, but permeability variations due to fracture aperture were not considered. This unsaturated flow experiment demonstrated that at the large scale, localized, vertical flow dominated, with some lateral spreading at rubble lenses in the formation (Doughty 2000). Trapped air played a significant role in guiding flow paths as well, and local responses within the network were dependent on the entire flow path (Doughty 2000). These findings are relevant to this research because multiple interacting phases are present, and properties vary significantly along any flow path in the model.

Additional studies of fluid flow in fractured basalt include the work of Khaleel (1989, 1992, 2001), who attempted to quantify the scale at which Columbia River Basalt flow interiors

may be reasonably approximated using an equivalent porous medium. Using data on the matrix permeability, aperture distribution, and fracture infilling, Khaleel (1989, 1992) found that the equivalent porous media assumption was valid for scales 22 to 27 times the diameter of a column in the colonnade for hydraulic conductivity, with slightly less stringent requirements for porosity. This scale is significantly larger than the 5-meter scale selected for the present study, and therefore this research will investigate effects not included in larger-scale models. Furthermore, Long et al (1982) found that a fracture set behaves most like an equivalent porous medium when the sample size is large, fracture density is high, apertures are constant rather than distributed, and orientations are distributed rather than constant.

In addition to larger-scale models, much discussion has been devoted over the years to the description of flow at the scale of the single fracture, a scale included in this study through the spatial variation of permeability at a fine (0.025 meter) scale. These studies generally invoke the cubic law, which states that in a fracture consisting of two smooth parallel plates, the permeability of a fracture may be uniquely defined by the separation distance between the two plates, otherwise known as the fracture aperture (Witherspoon et al 1980). Several common themes in cubic law research are important to the validity of this model for fracture permeability, including tortuosity, the presence of asperities, and fracture roughness. While numerous studies have found the cubic law to be valid under a variety of circumstances (Witherspoon et al 1980, Renshaw 1995, Ge 1997), concerns about these factors are a continuing matter of discussion in the literature, as they can have large effects on estimates of fracture permeability. For example, Wang et al (2015) found that the cubic law overestimates fluxes by up to 70%, and Zimmerman and Bodvarsson (1996), state that even if corrected for contact area, the cubic law greatly overestimates conductivity. The following is therefore a brief discussion of each of these factors, and how they are handled in the model presented in this research.

The first factor of general concern when applying the cubic law is the tortuosity of the flow path a fluid takes within a fracture. Tortuosity is the deviation from the straight-line path a particle could take between two points, and is not accounted for in the cubic law (Ge 1997). This presents a problem, since the viscous force due to tortuosity is therefore ignored in calculations, an oversight which can cause errors in estimation of fracture permeability (Ge 1997). Tortuosity is also not accounted for in the formulation of the cubic law used in this thesis to approximate permeability at each fractured cell in the model. However, this model takes place in only two

dimensions, meaning that a particle entering a fractured cell will only be able to travel with some vertical and one horizontal component of motion. That being said, fractures paths are not always straight in this model, as they are based on a real fracture type that tends to curve. Therefore, while the model presented in this research does not deal directly with tortuosity, it is roughly approximated by the distribution of the fractured cells.

The second source of uncertainty in using the cubic law to describe the permeability of a fracture is the presence of asperities within a fracture, or areas of contact between the two fracture planes. In a general sense, the cubic law becomes less effective at approximating fluid behavior as the contact area between the two planes increases (Tsang and Tsang 1987). Several studies have offered means of dealing with these asperities, often requiring additional assumptions about the area of contact between the two fracture surfaces (Zimmerman and Bodvarsson 1996). While these methods provide good approximations of fluid flow, the additional terms introduce another potential source of uncertainty. Additionally, approximations of contact area are only useful when simulating three-dimensional fractures. The network studied in this research is recreated two-dimensionally, and therefore the estimates of permeability within the fractures do not directly account for asperities. Rather, asperities are simulated where breaks in the fracture network appear on the LiDAR-derived fracture map used to build the simulation. As with real asperities, these breaks block and redirect flow, resulting in changes to the effective porosity of an entire flow path.

The final source of uncertainty common to the discussion of the cubic law, and the one most central to this research, is the surface roughness of planes forming a fracture. In the sense of a two-dimensional model, surface roughness takes the form of variations in the fracture aperture, which tends to be lognormally distributed (Gale 1987). Several methods exist for dealing with this variation in aperture, including using the mean value of aperture to represent an entire fracture. Renshaw (1995), for example, found that the geometric mean of such a lognormal aperture distribution is a robust estimate of the hydraulic aperture. Other studies, however, suggest that a mean permeability value resulting from such an assumption may result in sizable uncertainties in the flux estimates (Sagar and Runchal 1982). Errors due to this uncertainty are scale-dependent, with deviation from the cubic law increasing with decreasing average aperture (Mokhtari et al 2015, Hou and Benson 2015). In order to account for this uncertainty, a distribution of fracture aperture values may be used (Olsson and Barton 2001, Tsang and Tsang

1987). Fracture permeability is then calculated as a continuum over the domain, representative of the roughness of the fracture surfaces. This is the method applied in this research, and indeed it is the uncertainty associated with the use of an average value of permeability for a fracture set that this study seeks to explore.

CHAPTER 2: METHODS

This section presents the methods and workflow implemented for simulating CO_2 leakage through a basalt flow interior. LiDAR scans of a CRB outcrop were acquired near Starbuck, Washington, in order to map basalt fractures as they appear *in situ*. The LiDAR scans were then converted into binary fracture maps to define the distribution of fractured and unfractured basalt in the model domain. Simulations of CO_2 leakage were then performed using TOUGH3 (Jung et al 2016) with equation of state ECO2M (Pruess 2011). Preliminary models with increasing levels of complexity were developed, beginning with a homogeneous, isotropic model, then moving on to a model that included fractures with constant permeability values, and finally a model in which fracture permeability is assigned to each fractured cell from a lognormal distribution of permeability values. Finally, a Monte Carlo simulation was conducted, in which the spatial distribution of fractured cells remained constant, but the permeability of each cell was randomly assigned from the same lognormal distribution of permeability values in each of 50 simulation runs. The aggregate ensemble of 50 simulations was then analyzed for the mean and variance of CO_2 saturation and pressure in each grid cell, i.e. E-type estimates (Deutsch and Journel 1998).

Field Work - LiDAR Scanning

Ground-based light detection and ranging (LiDAR) scanning was performed on a basalt outcrop near Starbuck, Washington, using a Z+F Imager 5010x, and Z+F Profi targets. LiDAR scanning uses the two-way travel time of light beams to compute the distance from a point in space to the scanner. The Z+F imager 5010x is capable of scanning over one million pixels per second, resulting in an incredibly dense cloud of points (Z+F Laser, n.d.). In ground-based scanning, the scanner (Figure 5A), is mounted on a tripod which is periodically moved along the subject of the scan. Profi targets (Figure 5B) are included in each scan as spatial references for joining the scans together.

A road cut near the Little Goose hydroelectric dam on the Snake River was selected for scanning due to excellent exposure of typical CRB flow interior features, including entablature-type fractures. Some drill holes were visible on the rock face, but were deemed insignificant to the study, since they were relatively small and did not obscure fractures. Five scanning stations

selected along the outcrop provided detailed coverage of the entablature zones. Six Profi target were set up such that several targets would be visible from each of the five scanning stations. A Trimble Geo7x model 88161 GPS unit was used to record GPS locations of each target and scanning station. Figure 6 depicts the location of each target and scanning position in an aerial photo of the study area. At each LiDAR scanning station, a broad, relatively low-resolution scan was acquired, followed by one or more high-resolution scans. Each high-resolution scan included multiple Profi targets, with supplemental high-resolution scans of targets taken as necessary to ensure target accuracy. Large, high-resolution scans were recorded at stations 1, 2, and 5. Overlap between the low-resolution scans taken at stations 3 and 4 was judged sufficient to preclude the necessity of high-resolution scans at those locations.

LiDAR Scan Registration and Data Processing

LiDAR scan registration and data processing were performed using Z+F Laser Control software (Z+F, 2014). Scan registration is the process by which multiple individual scans are stitched together to produce composite representation of the subject of the scan. In order to complete this process, Profi targets are registered in each scan to provide reference points for merging. Upon merging, Z+F Laser control provides statistics regarding the accuracy with which the scans were merged. The average deviation of the Little Goose outcrop scan was 1.7 mm, the standard deviation was 1.0 mm, and the maximum deviation was 5.6 mm.

Following registration, a number of scattered points within the scan did not correspond to the outcrop. Since they appeared to be floating in mid-air above and in front of the outcrop, these points most likely represented LiDAR returns from dust or insects. Others may have been caused by vehicles, which very occasionally crossed the road between the tripod and the outcrop during scanning. In order to correct for these errant points, a filter was applied to the scan using tools in Z+F Laser Control. Finally, the complete scan was exported as an ASCII text file, containing local x, y, and z coordinates for all data points.

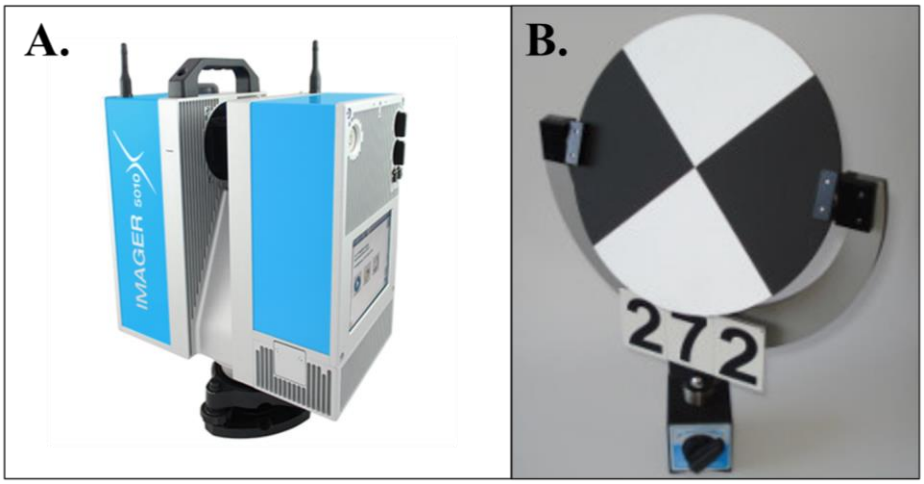

Figure 5: *LiDAR equipment - Z+F Imager 5010x and Z+F profi targets. Images from zf-laser.com*

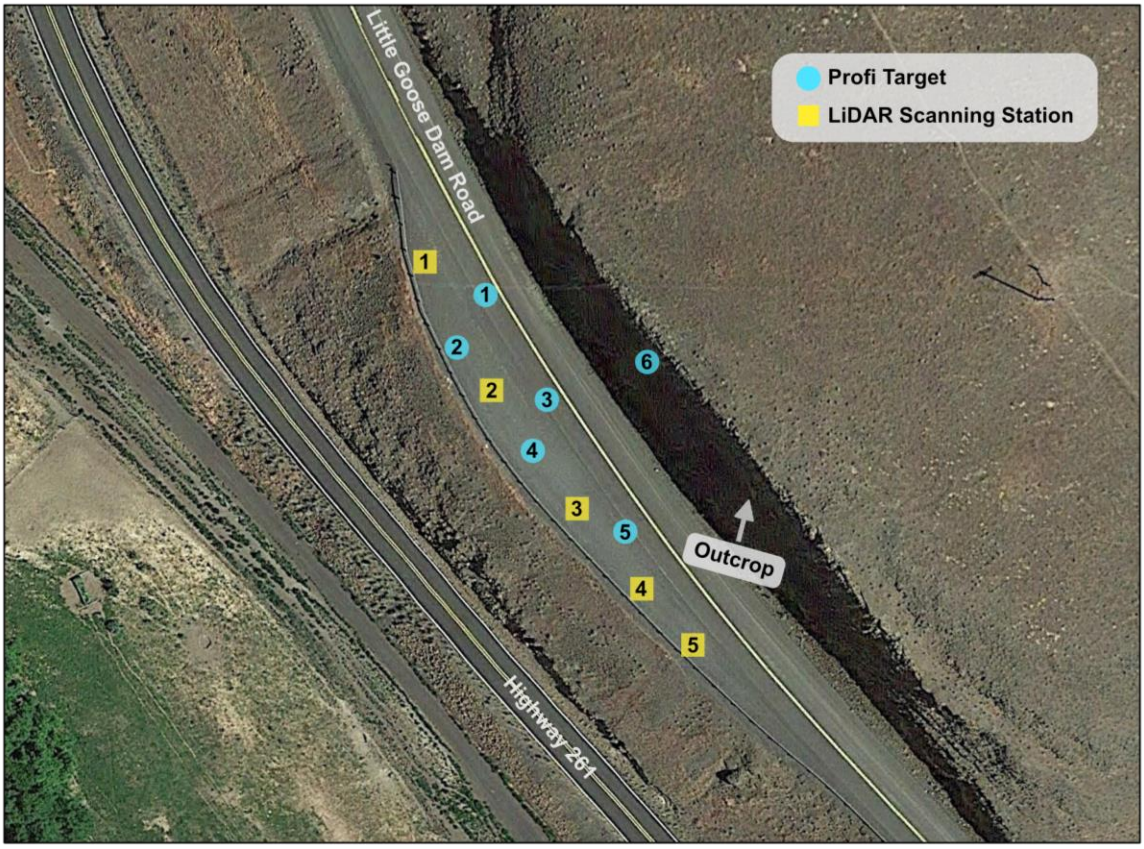

Figure 6: *Map of study area - **l**ocations of scanning station, profi targets, and scanned outcrop. Aerial photo taken from Google Earth.*

Surface Roughness Algorithm

The merged LiDAR scan was analyzed using the methods developed by Pollyea and Fairley (2011, 2012) to derive fracture maps from LiDAR scans using a surface roughness algorithm. This algorithm provides a quantitative, reproducible means of mapping fractures, which is invariant to the orientation of the scanner with respect to the outcrop (Pollyea and Fairley 2011). For a desired grid size, the 'roughness' program written by the authors computes a regression plane through each grid cell. It then computes the orthogonal distance of each point to the regression plane. Finally, the program computes the standard deviation of those distances for all points in each cell, a value called 'surface roughness' (Pollyea and Fairley 2011).

The surface roughness algorithm was run on several 5 × 5 meter sections of the data from the Little Goose outcrop using a grid size of 0.025 meters. Sections were chosen based on presence of entablature-type fractures. After the surface roughness values were computed, they were used to create fracture maps (Figure 7), using a process of normalization and binary transform following Pollyea and Fairley (2011). First, surface roughness values are normalized using the following equation:

$$R_{norm} = \frac{R - R_{min}}{R_{max} - R_{min}} \tag{5}$$

where *R* represents the surface roughness value. A binary transform is then performed on the data, dividing roughness values into two groups, fractured and un-fractured. This transform is based on the histogram of the data for each section, which tends to be log-normally distributed (Figure 7). Values clustering around the mean on the less rough end of the spectrum are labeled as un-fractured, while the most rough values located in the tail of the histogram are labeled fractured. The choice of the threshold value, below which values are labeled as un-fractured, is flexible, ultimately determined by the appearance of the fracture map. Figure 8 shows an example of how a threshold may be altered for more or less fracture connectivity.

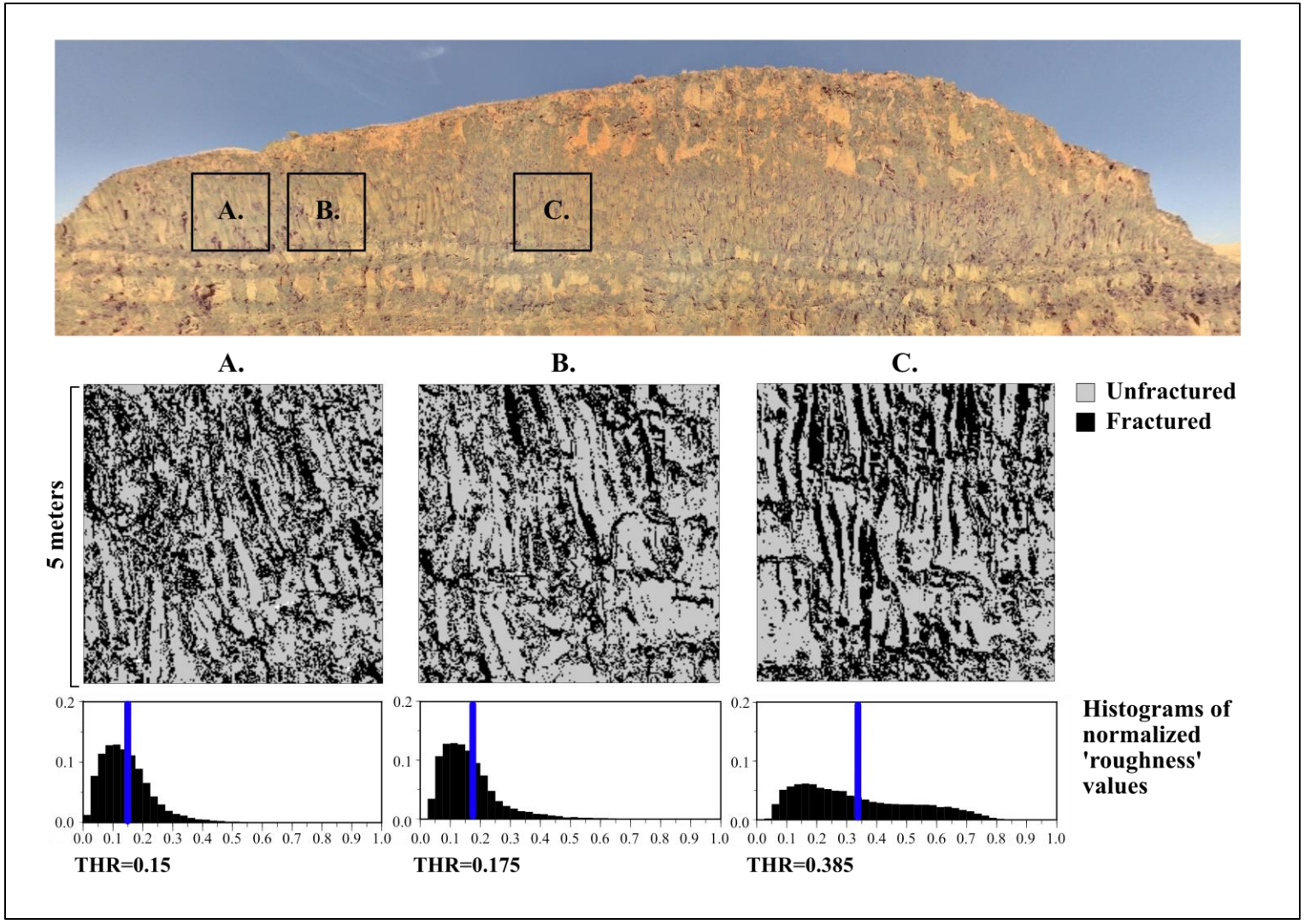

Figure 7: *Diagram of fracture mapping methods. Sections of outcrop selected for model (top), fracture maps created using roughness methods (middle), and histograms of normalized surface roughness for each section, A, B, and C (bottom). Fracture maps represent plots of binary roughness values: roughness of 0 assigned for cell with normalized roughness less than threshold (THR) on histogram, roughness of 1 assigned for each cell with normalized roughness greater than threshold.*

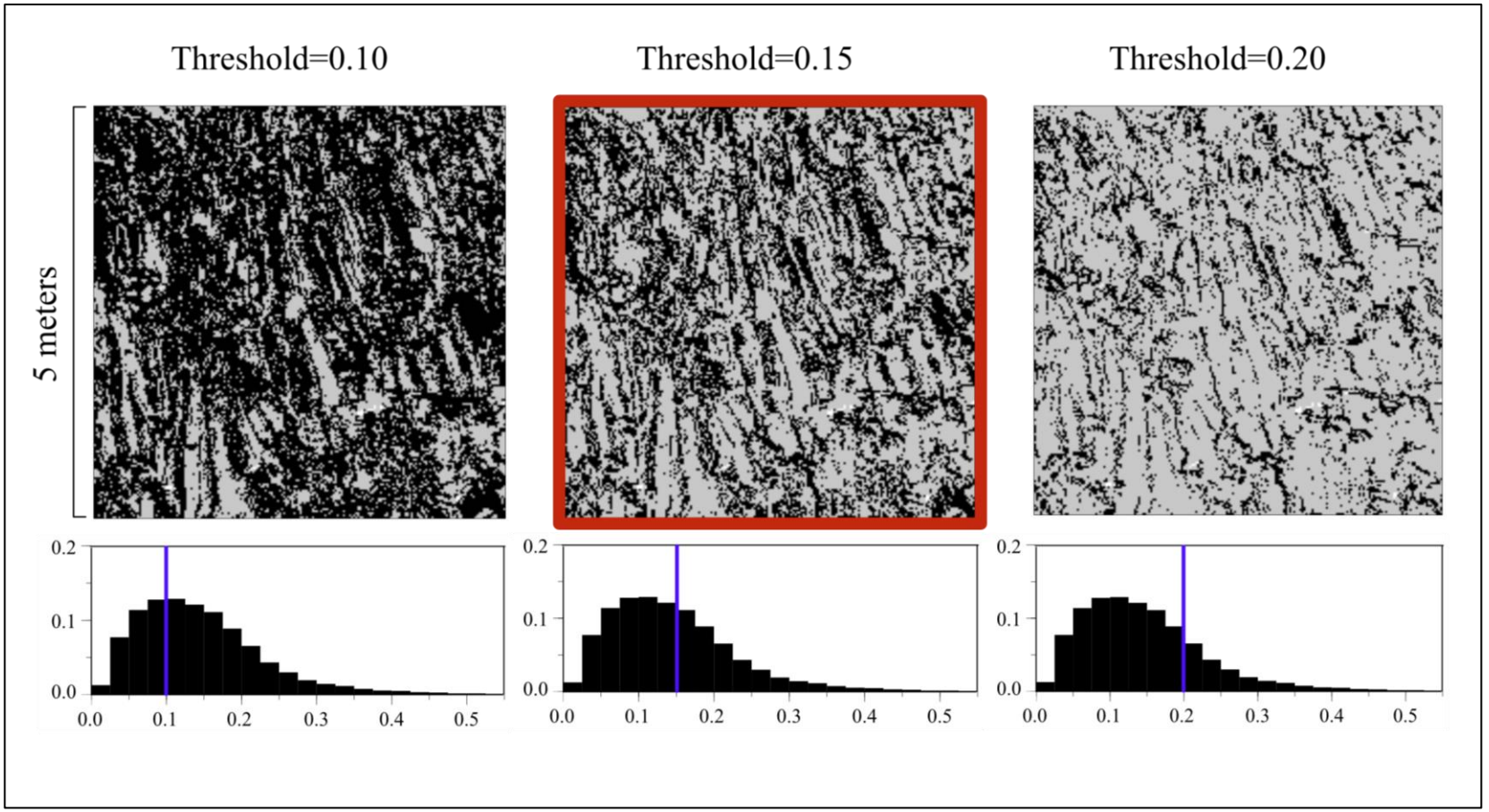

Figure 8: *Effects of roughness threshold on appearance of fracture map. Example thresholds shown for Box A from Figure 7. Histograms are of normalized surface roughness values. Cells with normalized roughness values to the left of the blue line are considered unfractured, cells with normalized roughness values to the right of it are considered fractured. Red box around center fracture map indicates threshold chosen for modeling flow through Box A.*

Code Selection

The TOUGH3 (beta) code was selected for this research, due to its flexibility in handling multi-component, multi-phase, non-isothermal systems (Jung et al., 2016). As with previous versions of the TOUGH software, TOUGH3 offers numerous equations of state for simulating different geologic scenarios and flow conditions. The equation of state ECO2M was chosen for this research, due to its ability to simulate non-isothermal multi-phase CO_2-brine interactions, including phase change between supercritical and subcritical CO_2 (Pruess 2011). This flexibility means that ECO2M contains several features relatively unique among the TOUGH equations of state; however, the basic processes of the code remain unchanged. The following section will review the basic equations underlying the TOUGH program, before moving on to features unique to ECO2M.

Every equation of state in the TOUGH software is based on the integral finite difference method, in which basic conservation equations, i.e. conservation of energy and mass, are not converted to partial differential equations for spatial discretization, and time is discretized as a first order backward finite difference (Pruess et al 1999). TOUGH thus solves mass and energy balance equations of this general type, after Pruess (1999):

$$\frac{d}{dt}\int_{V_n} M^k \, dV_n = \int_{\Gamma_n} \boldsymbol{F}^k \cdot \boldsymbol{n} d\Gamma_n + \int_{V_n} q^k dV_n \qquad (6)$$

In Equation 6, the accumulated mass or energy per some subdomain V_n is equal to the sum of accumulated mass or heat from fluxes, and the accumulation at sources (positive values) and sinks (negative values). V_n is an arbitrary subdomain of the flow system for which mass or heat accumulation is measured, bounded by the closed surface Γ_n. M is the mass or energy of a component per volume, with k=1…NK labeling components. $\boldsymbol{F}$ denotes mass or heat flux and q denotes sinks and sources; $\boldsymbol{n}$ is a normal vector on surface element $d\Gamma_n$, pointing inward into V_n.

The mass accumulation term is calculated as follows, again after Pruess (1999):

$$M^k = \phi \sum_\beta S_\beta \rho_\beta X_\beta^k \qquad (7)$$

Equation 7 states that the total mass of component k is obtained by summing over the fluid phases, where β represents the phase, ϕ is porosity, S_β is the saturation of phase β (fraction of pore space occupied by phase β), ρ_β is the density of phase β, and X_β^k is the mass fraction of component k present in phase β.

The heat accumulation term in a multiphase system is the sum of the heat transfer involving the rock and heat transfer involving the fluid. In the following equation, after Pruess (1999), the first term on the right side represents the rock, and the second term on the right side represents the fluid:

$$M^{NK+1} = (1-\phi)\rho_R C_R T + \phi \sum_\beta S_\beta \rho_\beta u_\beta \quad (8)$$

Where ρ_R is rock grain density, C_R is specific heat of the rock, T is temperature, and u_β is specific internal energy in phase β.

TOUGH calculates the advective mass flux by summing the mass of a component *k* over a flux $\boldsymbol{F}$ of phase β (Pruess 1999):

$$F^k|_{adv} = \sum_\beta X_\beta^k \boldsymbol{F}_\beta \quad (9)$$

Individual phase fluxes in turn are given by a multiphase version of Darcy's law (Pruess 1999):

$$\boldsymbol{F}_\beta = \rho_\beta \boldsymbol{u}_\beta = -k \frac{k_{r\beta}\rho_\beta}{\mu_\beta}(\nabla P_\beta - \rho_\beta \boldsymbol{g}) \quad (10)$$

Where $\mathbf{u}_\beta$ is the Darcy velocity (volume flux) in phase β, *k* is the absolute permeability, $k_{r\beta}$ is the relative permeability to phase β, u_β is viscosity, $\boldsymbol{g}$ is the gravitational vector, and the fluid pressure in phase β is the sum of the pressure (P) of some reference phase and the capillary pressure of phase β, $Pc\,\beta$ (Pruess 1999). The pressure gradient is represented by the term ∇P_β.

These same equations describe the bulk of ECO2M – mass and energy fluxes are solved for in the same ways, for up to 3-component (water, salt, CO_2) fluids consisting of one, two, or three phases, which may include a water-rich aqueous phase, and one or two CO_2 rich phases referred to as liquid and gas (Pruess 2011). For super-critical temperatures, (T > 31.01 °C), the liquid phase refers only to supercritical CO_2, while the gas phase refers to CO_2 at pressures less than the critical pressure (P < 7.39 MPa), which may include both subcritical liquid and gas (Pruess 2011). Subcritical liquid and gas behave differently according to their physical properties, but for the purposes of simplicity they share a label in ECO2M. Each cell can contain any combination of aqueous, liquid, and gas phases, as depicted in Figure 9.

The main differences between ECO2M and other TOUGH equations of state are its ability to simulate salt precipitation and dissolution, and its ability to simulate CO_2 phase changes between super-critical fluid, fluid, and gas. Solid salt precipitation or dissolution in any given cell is determined by local equilibrium solubility (Pruess 2011). Phase partitioning is calculated such that chemical potentials of all components are equal in different phases, from

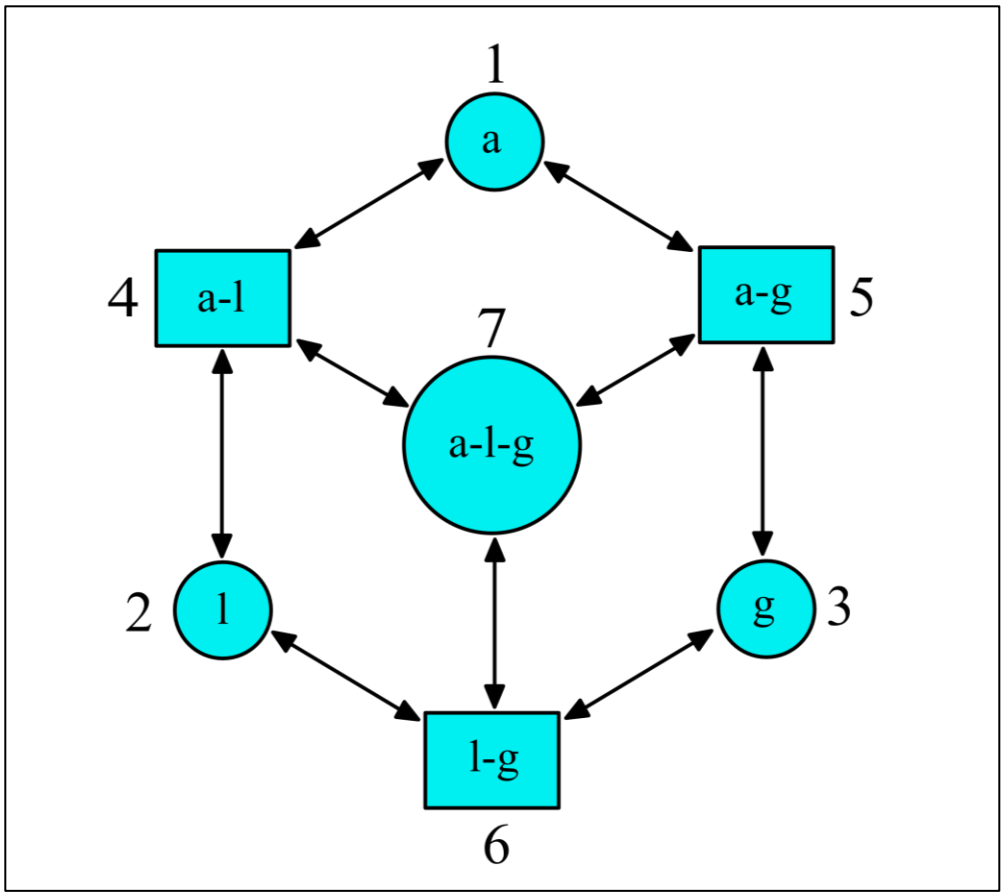

Figure 9: *Phase combinations simulated by TOUGH3-ECO2M, after Pruess (2011). Letters represent phases present - a is aqueous, l is liquid, and g is gas. Numbers represent phase indices used in the input files.*

Altunin's correlations, as used in Spycher and Pruess (2005) (Pruess 2011). These correlations are tabulated in a lookup table containing density, viscosity, and specific enthalpy values for CO_2 on a regular grid of temperature and pressure values. During a simulation, property values for CO_2 are drawn from this table by means of bivariate interpolation (Pruess 2011). ECO2M can thus predict the equilibrium composition of water-rich and CO_2-rich phases as a function of temperature, pressure, and salinity from 12° to 110°C, pressures up to 60 MPa, and salinity up to NaCl brines (Pruess 2011). However, phase partitioning can complicate things numerically because when CO_2 approaches the phase change boundary, temperature and pressure oscillations within a Newton-Raphson iteration may results in phase change within a time step causing convergence failures. In order to compensate for this numerical instability, ECO2M implements a 'finite window' scheme, which was implemented for this research. This 'finite window' means

that a phase change does not occur exactly when the fluid pressure is less than the critical pressure for CO_2, but instead when the fluid pressure is less than the critical pressure of CO_2 times one minus some small value, for this study chosen to be 10^{-3} (Pruess 2011). This distinction allows for greater numerical stability, as it means that CO_2 reaching the critical point from below will already be in the process of changing phases, having already entered the finite phase change window.

Homogeneous Model

A two-dimensional, homogeneous, isotropic model with bulk properties consistent with Columbia River Basalt flow interiors was developed in order to establish a working knowledge of the code, and evaluate simulation results in the context of expected physical behavior, i.e. intuition. Model dimensions were 5 meters by 5 meters, with a horizontal and vertical discretization of 0.025 meters, resulting in 40,000 grid cells.

Important decisions forming the basis of the model included parameters for rock properties, the pressure profile and boundary conditions, the way in which CO_2 was introduced to the model, and the choice of relative permeability and capillary pressure models. Through review of the literature, the parameters listed in Table 1 were found to realistically represent rocks of Columbia River Basalt flow interiors. The pressure profile was based on the hydrostatic gradient from McGrail et al (2009) with the simulated depth of the model such that the critical point for CO_2 would occur approximately 1.5 m above model base at initial conditions. Boundary conditions were chosen to simulate vertical flow through the model, with open conditions at the top. As such, no-flow boundaries were placed at the sides of the model, and a Dirichlet boundary at the top. Figure 10 depicts the initial conditions of the homogeneous model.

In order to simulate a CO_2 plume encountering the base of the basalt flow interior, 0.5 MPa of CO_2 overpressure was assigned to a single cell of infinite volume at the base of the domain, with connections to all of the cells in the row above it. This allowed CO_2 to enter the model at a constant pressure, inducing vertical flow. For this low-permeability model, this method was judged superior to constant-mass injection at the basal cells, because with constant mass injection, the low permeability caused CO_2 to build up in cells near the injection, rapidly increasing pressure. Moreover, the constant pressure injection is more physically realistic because CO_2 does not leak at a constant rate. Rather the leakage rate is dependent on the

Table 1 - Parameters for homogeneous model		
Parameter	**Value**	**Reference**
Total dissolved solids:	270 mg/L	McGrail et al 2009
Hydrostatic pressure gradient:	0.435 psi/ft	McGrail et al 2009
Model domain temperature:	32 °C	
Critical pressure for CO_2:	7.39 Mpa	Edlmann et al 2012
Basalt specific heat:	840 J/kg°C	Burns et al 2015
Basalt thermal conductivity:	2.11 W/m/°C	Eppelbaum et al 2014
Basalt density:	2950 kg/m^3	Burns et al 2015
Basalt matrix compressibility:	1.45E-17 Pa^{-1}	Adams and Gibson 1926
Permeability:	1.00E-18 m^2	Wood and Fernandez, 1988
Porosity:	0.05	Doughty 2000

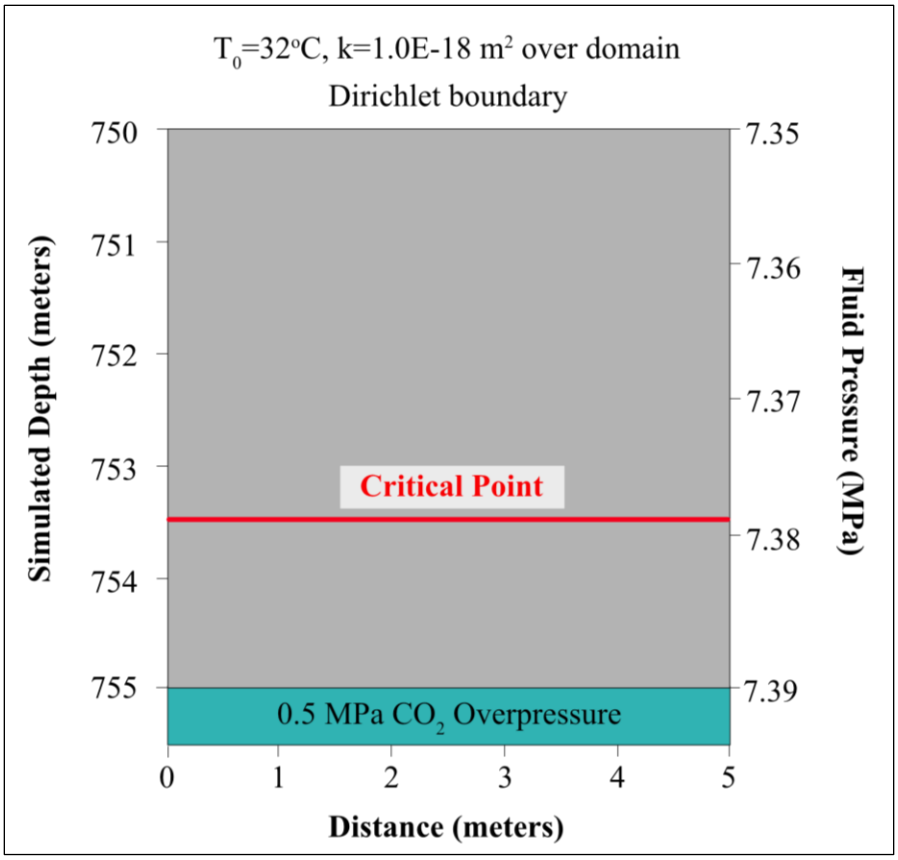

***Figure 10**: Initial conditions of homogeneous, isotropic model. CO_2 is introduced in super-critical form at overpressure of 0.5 MPa at model base. Critical pressure initially occurs 1.5 meters above model base, at 7.39 MPa.*

pressure head driving the plume and the permeability of the rock through which the CO_2 is moving. The mass fluxes into each basal cell, however, compare fairly well to mass fluxes expected near the top of a rising CO_2 plume in basalt, as predicted by the modeling experiments of Pollyea and Fairley (2014). When adjusted for size of grid cell, their model predicted that fluxes on the leading edge of a plume would be on the order of 2.5E-10 kg/s. On average, fluxes into the basal cells of the homogeneous model are around 9.6E-09 kg/s.

The final important step in developing the homogeneous, isotropic model was to choose a relative permeability and capillary pressure model suited to the fluids and materials present. Data for relative permeability was obtained from Bertels et al (2001), in which CT scanning was used to measure the relative permeability of nitrogen and liquid water in a rough-walled fracture through a Columbia River Basalt sample. These data were used to fit curves formed by the equations of Stone (1970), as implemented for three-phase relative permeability in TOUGH3. The Stone (1970) relative permeability model is designed for 3-phase systems, and utilizes the following equations to describe the relative permeability for each phase:

$$k_{rg} = \left[\frac{S_g - S_{gr}}{1 - S_{ar}}\right]^n \tag{11}$$

Where k_{rg} is the relative permeability of the gas phase, S_g is the gas saturation, S_{gr} is the residual gas saturation S_{ar} is the residual aqueous (water-rich) phase saturation, and n is a phase interference parameter.

$$k_{ra} = \left[\frac{S_a - S_{ar}}{1 - S_{ar}}\right]^n \tag{12}$$

Where k_{ra} is the relative permeability of the aqueous phase, S_a is the aqueous phase saturation. Finally,

$$k_{rl} = \left[\frac{1 - S_g - S_a - S_{lr}}{1 - S_g - S_{ar} - S_{lr}}\right]\left[\frac{1 - S_{ar} - S_{lr}}{1 - S_a - S_{lr}}\right]\left[\frac{(1 - S_g - S_{ar} - S_{lr})(1 - S_a)}{(1 - S_{ar})}\right]^n \tag{13}$$

Where k_{rl} is the relative permeability of the non-wetting liquid phase, S_{lr} is the residual liquid phase saturation. When $S_l = 1 - S_a - S_g - S_s$ is near irreducible liquid saturation, $S_{lr} \leq S_l \leq S_{lr} + 0.005$, liquid saturation is taken to be:

$$k'_{rl} = k_{rl}\frac{S_l - S_{lr}}{0.005} \tag{14}$$

The basis for these equations is channel theory, which states that in any given channel, only one fluid is active (Stone 1970). It further assumes that the wetting phase tends to remain largely in small pore spaces, while the non-wetting phases is limited to the large ones, with the

intermediate phase located between the two (Stone 1970). Because of this separation, interactions of the liquid non-wetting phase with water and with gas are separate events (Stone 1970). Curve matching of data from Bertels et al (2001) to Stone (1970) curves is shown in Figure 11. Note that the relative permeability for the gas phase goes above 1.0 at low aqueous phase saturations: this is consistent with Lee et al (2013) who show that at low wetting-phase saturations, the wetting phase can form a lubricating film over which the non-wetting phase flows, resulting in a relative permeability greater than one.

TOUGH3 currently offers only one capillary pressure model for 3-phase systems, that of Parker et al (1987). It utilizes the following equations to calculate the air entry pressure, based on strength coefficients specific to the material and phase interference and residual liquid saturation specific to the fluids:

$$m = 1 - \frac{1}{n} \tag{15}$$

Where *m* is the Van Genuchten Phase interference parameter.

$$\overline{S_a} = \frac{S_a - S_m}{1 - S_m} \tag{16}$$

Where S_a is the aqueous phase saturation, S_m is the residual aqueous phase saturation.

$$\overline{S_l} = \frac{S_a + S_l - S_m}{1 - S_m} \tag{17}$$

Where S_l is the liquid phase saturation.

$$P_{cgl} = -\frac{\rho_a g}{\alpha_{gl}} \left[\overline{S_l}^{-1/m} - 1 \right]^{1/n} \tag{18}$$

P_{cgl} is the capillary pressure between the gas and liquid phases; ρ_a is the density of the aqueous phase; g is the acceleration due to gravity; α_{gl} is a strength coeffient.

$$P_{cga} = -\frac{\rho_a g}{\alpha_{la}} \left[\overline{S_a}^{-1/m} - 1 \right]^{1/n} - \frac{\rho_a g}{\alpha_{gl}} \left[\overline{S_l}^{-1/m} - 1 \right]^{1/n} \tag{19}$$

P_{cga} is the capillary pressure between the gas and aqueous phase; α_{la} is another strength coefficient. Finally, the capillary pressure between the liquid and aqueous phase is defined as:

$$P_{cla} = P_{cga} - P_{cgl} \tag{20}$$

The residual liquid phase saturation and the phase interference parameter derived from curve matching to the Stone model for relative permeability (Figure 11) were used as inputs to the Parker et al (1987) capillary pressure models, in order to insure consistency across models. The strength coefficients for the equations are taken from Parker et al (1987), in which strength

parameters for clays are listed. Clay parameters are assumed to be suitable for these purposes since most CRB fractures are filled with clay (Lindberg 1989). The resulting entry pressure curves for liquid (super-critical) and gas-phase CO_2, which serve as the model for capillary pressure in the homogeneous system, are shown in (Figure 12).

Figure 13 contains the results of the homogeneous flow experiment. As expected, the results show a simple, straight-edged plume of supercritical CO_2 rising from the base, gradually moving further up with time. As the CO_2 penetrates further upward, the fluid pressure increases as well, gradually moving the critical pressure for CO_2 to shallower depths. By the time the simulation reaches ten years, the critical point has moved to just below the top of the domain, and gas phase CO_2 begins to form.

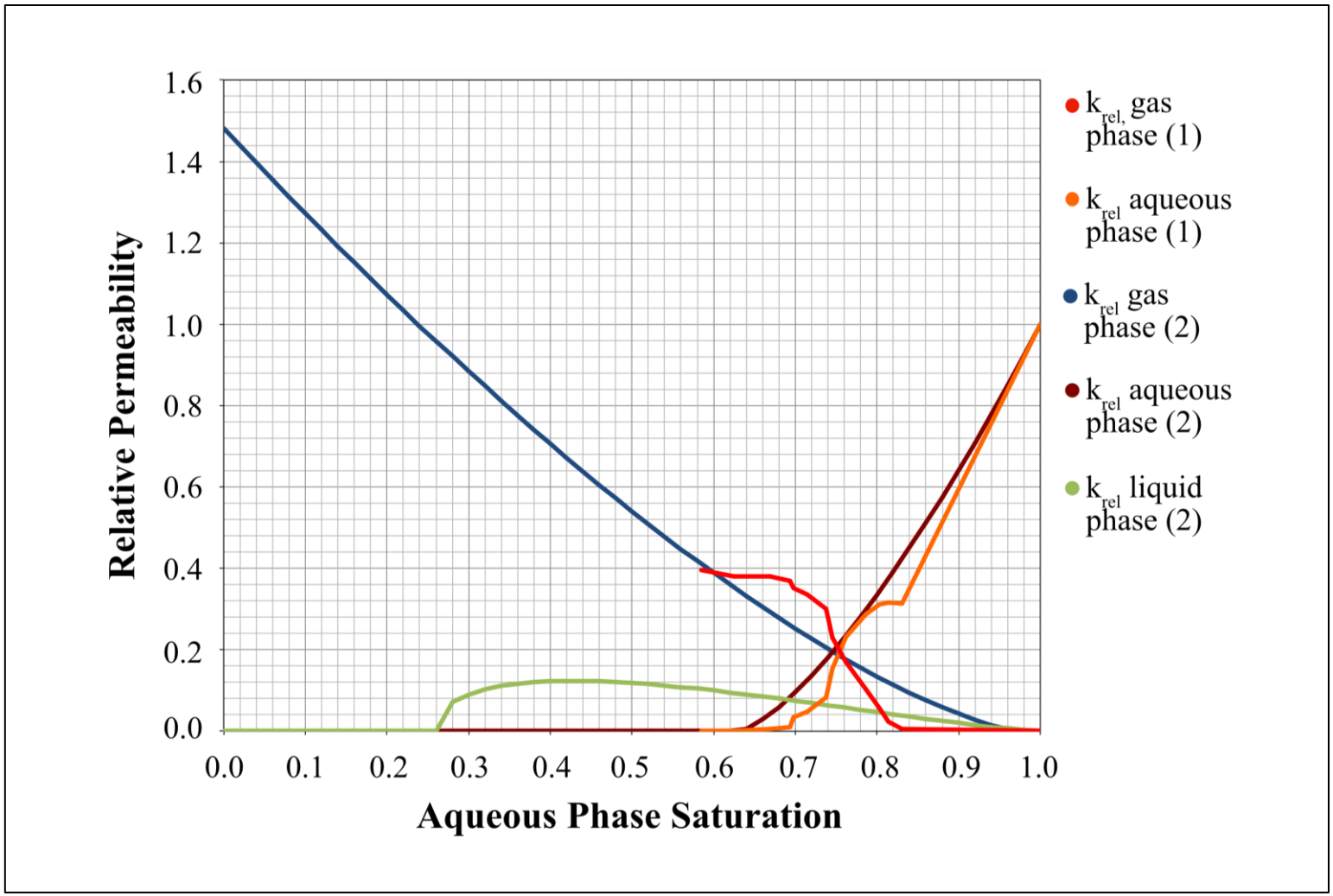

***Figure 11**: Relative permeability curve matching. Data from Bertels et al (2001) labeled as (1), matched curves using Stone (1970) model labeled as (2)*

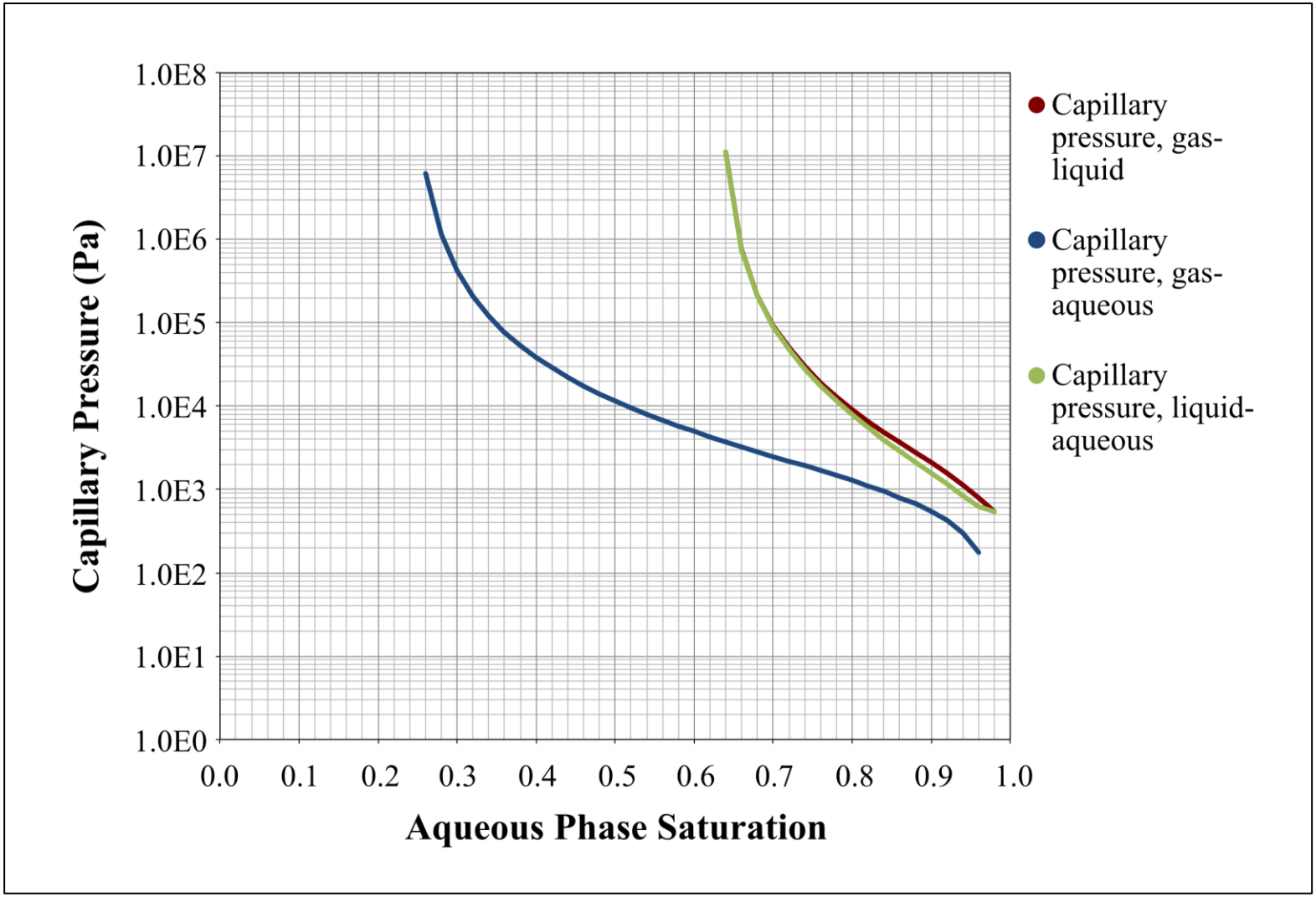

***Figure 12**:Capillary pressure curves computed for model. Parker (1987) capillary pressure curves calculated using curve matching parameters from relative permeability model*

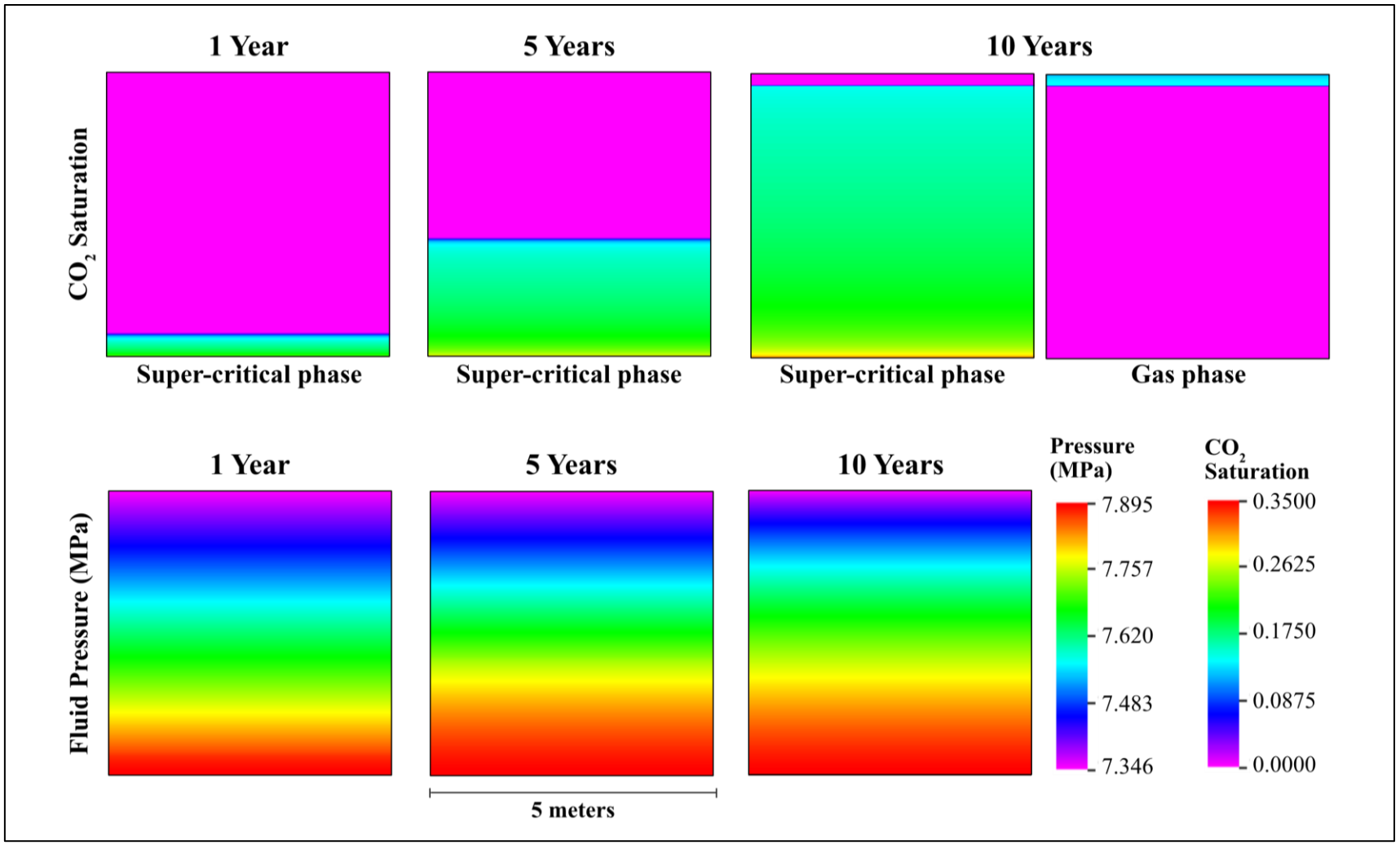

***Figure 13**: Results for homogeneous, isotropic model at 1, 5, and 10 years. CO_2 saturation (above) and fluid pressure (below) indicate phase change occurs at around 10 yeas simulation time.*

Fracture Flow Models with Constant Permeability

Following successful experimentation with the two-dimensional homogeneous, isotropic model, three models of the same dimensions were built in TOUGH3 in which two materials were present. The properties of these materials correspond to those of basalt matrix and basalt fractures, and their distribution corresponds to blocks labeled 'fractured' and 'un-fractured' in each of the three LiDAR-derived fracture maps shown in Figure 7. The initial pressure conditions and boundary conditions remained identical to those used in the homogeneous model, as did the capillary pressure and relative permeability models. CO_2 was introduced in the same way as well, with 0.5 MPa of overpressure at the base. The goal in developing these models was to determine which fracture map could be used to model the most realistic leakage of CO_2.

These models were built using the script 'dualk.sh' in Appendix A, which assigned each grid cell in the TOUGH3 mesh file a rock identity of 'FRACT' (for fractured) or 'BASLT' (for non-fractured), based on the location of fractured and un-fractured cells in the fracture map. In TOUGH3, the rock identity determines the properties a grid cell is assigned from the input file. Input parameters used for each rock identity are listed in Table 2. The initial conditions for one of the models are depicted in Figure 14. The porosity for the basalt was chosen to be very low, reflecting the dense nature of flow interior basalts (McGrail et al 2009). According to several literature sources, fractures in the Columbia River Basalt flow interiors tend to be over 99% filled, primarily with clays (Lindberg 1989). The porosity of the fractured cells was therefore chosen to reflect the porosity of the clay infill.

Table 2 - Parameters for model with constant fracture permeability

Matrix properties:		
Permeability:	1.00E-20 m^2	Doughty (2000), Bertels et al (2001)
Porosity:	0.05	Doughty (2000)
Fracture properties:		
Permeability:	1.00E-16 m^2	Solved value
Porosity:	0.10	Khaleel (1992)

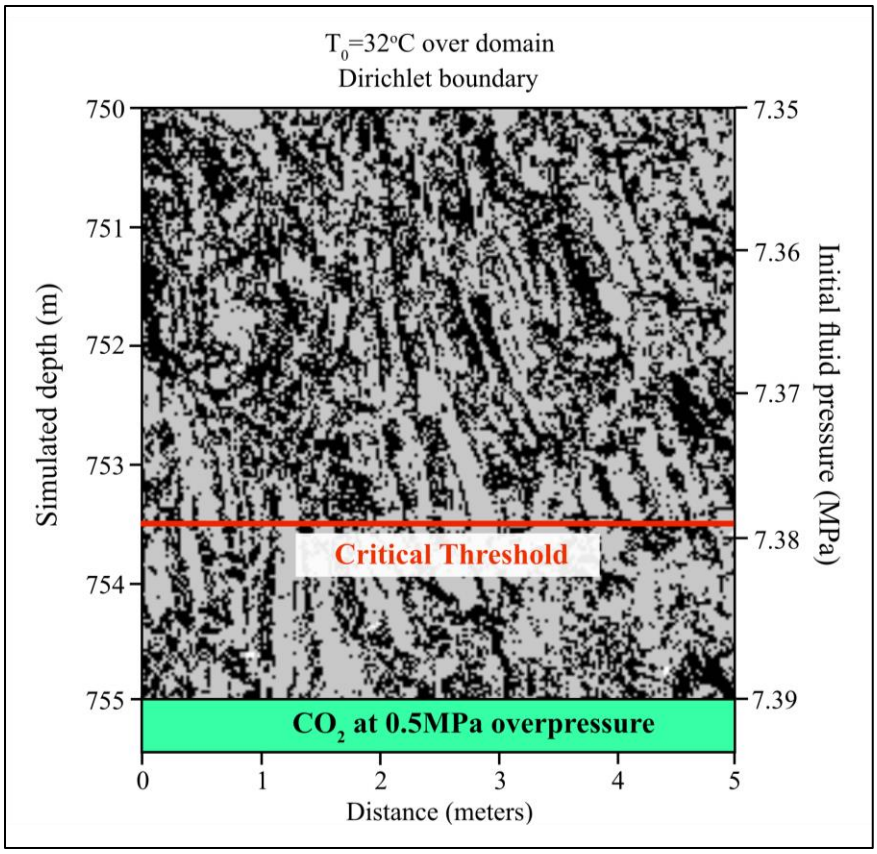

Figure 14: *Initial conditions for model with constant fracture permeability. CO_2 introduced as supercritical fluid, critical pressure initially occurs 1.5 m above model base.*

The permeability of the basalt cells is based on several laboratory tests, which place matrix permeability for the Columbia River Basalt between 5.0E-17 (Doughty 2000) and 1.0E-24 m^2 (Bertels et al 2001). The value of 1.0E-20 m^2 was chosen for the model because it falls in the middle of this range.

Due to the widespread evidence of fracture filling and a general lack of data on the permeability of filled Columbia River Basalt fractures, the permeability for fractured cells was determined by inverting a weighted geometric mean equation for effective permeability to solve for fracture permeability, as follows:

$$k_{eff} = \exp\left(\frac{\sum_{i=1}^{n} w_i lnk_i}{\sum_{i=1}^{n} w_i}\right) \quad (21a)$$

$$lnk_{eff} = \frac{w_m lnk_m + w_f lnk_f}{1} \quad (21b)$$

$$k_f = \exp\left(\frac{lnk_{eff} - w_m lnk_m}{w_f}\right) \quad (21c)$$

In Equations 21a-c, k_{eff} is the effective permeability, approximately 1.0E-18 m^2 (Wood and Fernandez 1988); k_m is the matrix permeability, 1.0E-20 m^2; w_f and w_m are the weights assigned to the fracture and matrix permeability respectively, based on the proportion of the cells in the fracture map marked as fractured (0.42) and un-fractured (0.58); k_f is the fracture permeability, for which the equation is solved. The permeability of filled Columbia River Basalt fractures was thus determined to be on the order of 1.0E-16 m^2.

Using this parameterization, a model was built simulating flow through each of the three fracture networks in Figure 7, in order to determine which model contained enough inter-connected fractures to realistically simulate fracture flow. Figure 15 demonstrates that of the three boxes tested, boxes A and C allow leakage through most of the model. Box C, however, also shows accumulations of super-critical CO_2 at several points along the main flow path. These accumulations are the result of two factors – first, the flow paths are large, up to 0.3 meters wide, which allows CO_2 to travel fairly rapidly along them, and in large quantities. Second, there is a break in the main flow path just over halfway up the model, causing CO_2 to back up at that point.

In contrast, Box A possesses much more realistic flow paths, with few obstructions along the main flow path. While CO_2 does not quite reach the top of the model within 10 years, it does get close, and clearly possesses a path to leakage. Based on these results, Box A was selected as the best prospect for the final stage of the modeling process.

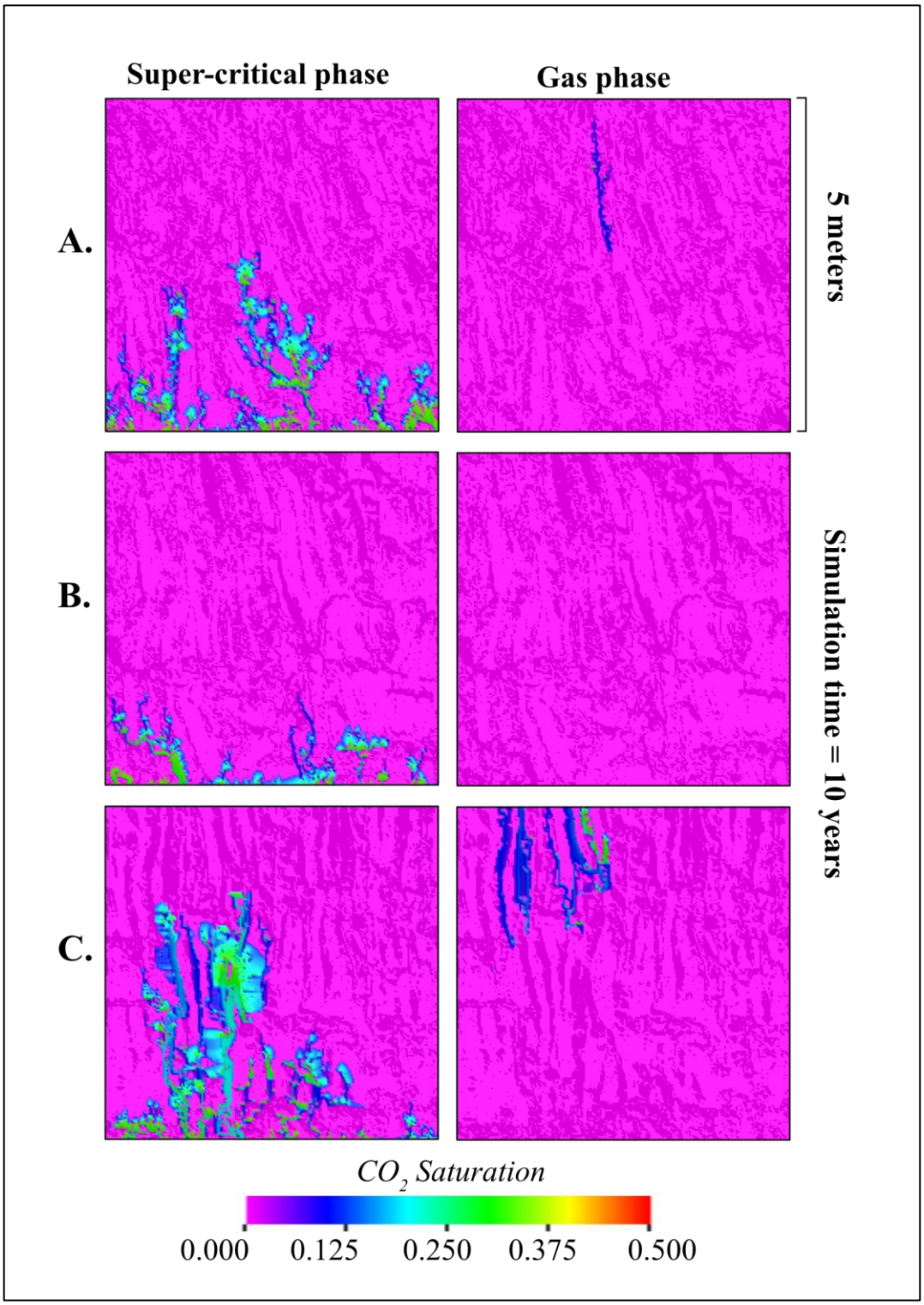

Figure 15: *Results for models with constant fracture permeability at 10 years. A, B, and C correspond to A, B, and C in Figure 7.*

Random Permeability Fracture Model and Monte Carlo Simulations:

The final stage of the model-building process was to modify the permeability of each cell labeled as 'fractured', in the fracture flow models, such that the permeability values of the 'fractured' cells followed a distribution reflecting the natural variability in fracture aperture.

According to numerous sources (Kwicklis and Healy 1993, Nordqvist et al 1992, Long et al 1982, Gale 1987, Renshaw 1995, Hakami 1995, Bertels and DiCarlo 2001, Khaleel 1989, Baghbannan and Jing 2006), aperture measurements of natural fractures tend to follow a lognormal distribution. Lindberg et al (1989) found that fracture apertures in Columbia River Basalt flow interiors follow the same trend. They measured the aperture of approximately 3,200 cooling joints from cores of CRB flow interiors using calipers, and found that the apertures are approximately lognormally distributed, with a mean of 0.226 mm and standard deviation of 0.498 mm (Lindberg et al 1989). Lindberg et al (1989) also tested for spatial correlation of aperture, and found none in the sample collected.

For this study, the Lindberg (1989) aperture distribution forms the basis for establishing a permeability distribution representative of CRBG flow interiors. This distribution constrains fracture permeability in model domain; however, implementing this distribution with spatial variability required a Monte Carlo modeling approach to generate 50 equally probable, randomly distributed fracture permeability sets. This was accomplished using two shell scripts, which can be found in Appendix A. The first one, iperm.py, generates a set of N random numbers with a standard deviation *s* and a mean of *u*. N is user-input as the number of fractured cells, and *s* and *u* are hard-coded, taken from the Lindberg (1989) data. This set of random numbers represents a synthetic aperture sample with properties identical to the Lindberg (1989) measurements. The script then converts the apertures to permeability values using the Local Cubic Law (Witherspoon et al 1980), where permeability (*k)* is uniquely defined by aperture (*b*):

$$k = \frac{b^2}{12} \tag{22}$$

The numbers then represent the permeability values of each fractured cell, assuming that the Local Cubic Law is a good approximation of permeability for these fractures. As determined earlier, however, Columbia River Basalt fractures in the flow interior tend to be up to 99% filled (Gephart et al 1983, Long 1978, Khaleel 1989, Lindberg et al 1989). Therefore, while the standard deviation of these fracture permeability values may be representative of the variation in CRB apertures, the mean as determined by the LCL will not be valid. In order to correct for this,

the random permeability population is translated to correspond with the mean CRB fracture permeability calculated in Equation 21c (1.0E-16 m^2).

Following the generation of these spatially random permeability distributions, a second script, p3rmsh.sh, inserts them into the TOUGH3 mesh file, such that each cell has its own permeability value. For this process, p3rmsh.sh uses constant permeability in the matrix, but fracture permeability is assigned from the lognormal distribution discussed above. The final setup for the model is shown in Figure 16.

In order to test the effects of spatial uncertainty of fracture permeability in such a system, 50 of these simulations were created, in which fracture permeability follows the same distribution, but is spatially random. To accomplish this, 50 random sets of permeability values with the same mean and standard deviation were generated, and then incorporated into 50 different models according to the methods discussed above. Each randomly generated distribution was essentially identical, but where any number occurred in the mesh was totally random.

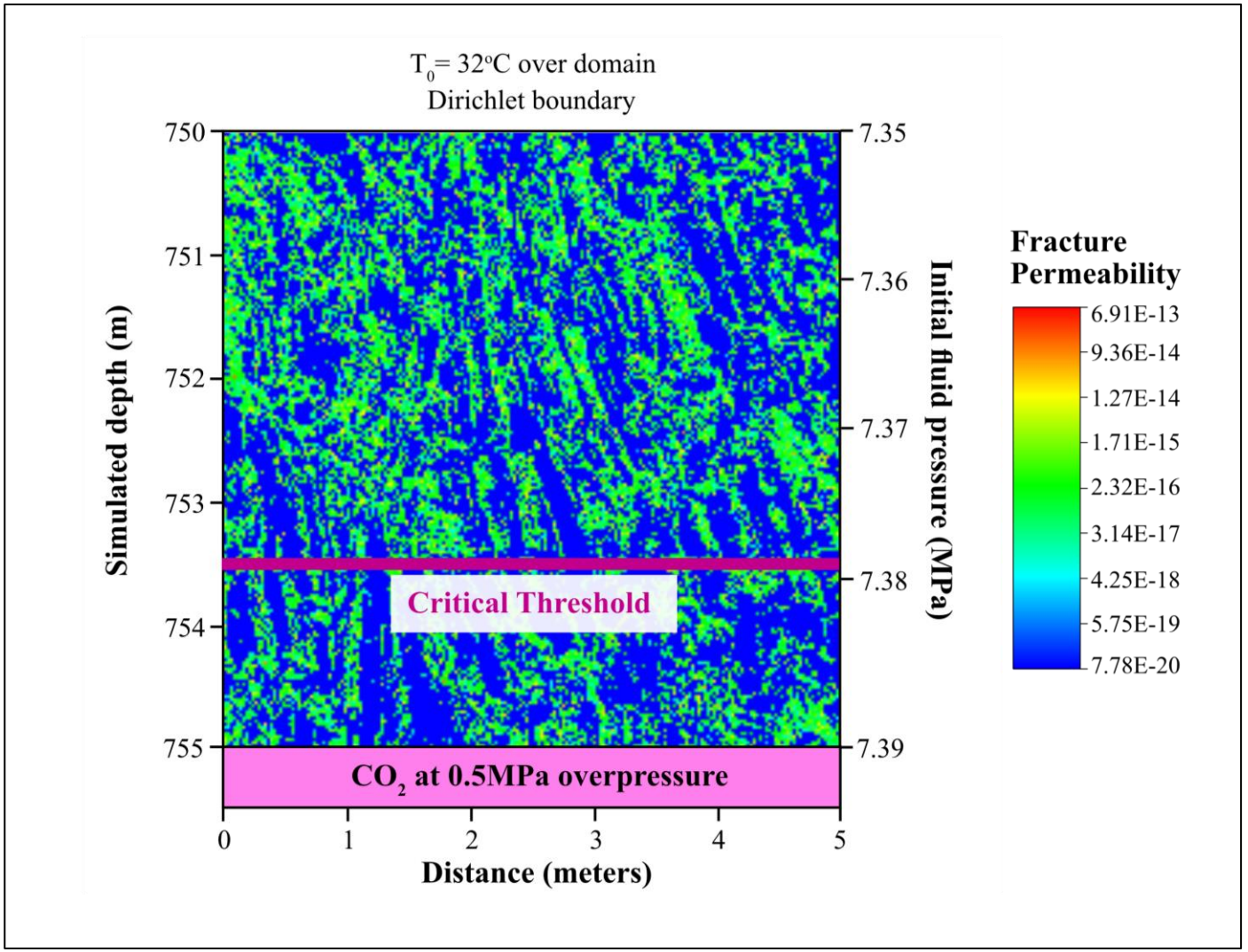

Figure 16: *Initial conditions for model with random fracture permeability. CO_2 introduced as supercritical fluid, critical pressure (7.39 MPa) initially occurs 1.5 m above model base. Matrix permeability is constant at 1.0E-20 m^2, while fracture permeability is randomly assigned to each fractured cell from lognormal distribution of values.*

CHAPTER 3: RESULTS

Data Analysis

Results were output for each run of the Monte Carlo simulation at one, five, and ten years. These time steps offer a look at CO_2 saturation and phase partitioning, as well as fluid pressure, at several very short time-scales relevant to buoyancy trapping of CO_2 by basalt flow interiors. At time-scales beyond ten years, carbonate mineralization is expected to dominate physical trapping processes, rendering non-reactive simulation ineffective. Results for this section are of two basic types. The first type consists of visual comparisons between results of two example runs, Run 39 and Run 46, which represent end-members of model behavior at 10 years. These runs are compared to each other, as well as to a model where fracture permeability is constant. The second type of results consists of E-type analyses of several parameters across all 50 runs. E-type analysis is a statistical method wherein mean and variance are calculated for each grid cell in the domain (Deutsch and Journel, 1998). This method yields an expected result for the ensemble of simulations, as well as a measurement of uncertainty surrounding the modeling experiment. For this study, E-type estimates comprise aggregate results of all 50 simulations. For each time step, an E-type plot of mean and standard deviation of fluid pressure, free-phase CO_2 saturation, and, where applicable, liquid and gas phase CO_2 saturation, is produced.

Results - One Year

Results for the example runs at one year are presented in Figure 17. At this early time, CO_2 saturation is all in the super-critical phase in both the random permeability runs and the bimodal run, rising in several fractures to a maximum depth of 754 meters. CO_2 follows the same pathways across all 3 models with very minor variations in saturation, and a maximum saturation across all three models of around 0.40. Fluid pressure remains consistent across each of the three models as well. Pressure propagates upward through the domain according to the availability of high-permeability conduits. As a result, in each model fluid pressure decreases upward non-linearly, with higher pressures below blockages in the fracture pathways, and lower pressures along clear conduits.

E-type results for one year are presented in Figure 18 and Figure 19. Figure 18 depicts the E-type analysis for liquid-phase CO_2 saturation, while Figure 19 depicts the E-type analysis for fluid pressure. The standard deviation of liquid CO_2 saturation (Figure 18B) is fairly constant, with the standard deviation for most cells around 0.06 to 0.10. Mean liquid saturation (Figure 18 a) closely follows the results for the example runs (Figure 17), with saturation generally around 0.20 and a maximum around 0.36. The standard deviation of fluid pressure (Figure 19B) reflects fairly substantial variation in fluid pressure at early time, with a maximum deviation of 72000 Pa. The most variability seems to occur below constrictions or blockages in the main fracture pathways, suggesting that at early time the permeability at such cells plays a large role in fluid pressure distribution. Additionally, fluid pressure shows no variability within the fractures containing CO_2 at this time (Figure 19B), even as fluid pressure variability around the fractures is at the maximum for the domain. In contrast, CO_2 saturation in the same fractures does show variability. CO_2 therefore enters the fracture network at the same fractures regardless of the permeability distribution, as evidenced by the lack of variability in the fluid pressure at those fractures. However, the saturation of CO_2 at any given point is a function of permeability along the flow path. The mean fluid pressure (Figure 19A) is essentially identical to the example runs in Figure 17, with the same general distribution, and the same minimum and maximum values. All of this together indicates that despite the variability demonstrated in Figures 16B and 17B, model behavior in early time tends to follow the same general patters across all 50 simulations. At 1 year elapsed time, the geometry of the fracture network appears to be the primary control on fluid pressure, while the local fracture permeability values introduce small variations in CO_2 saturation.

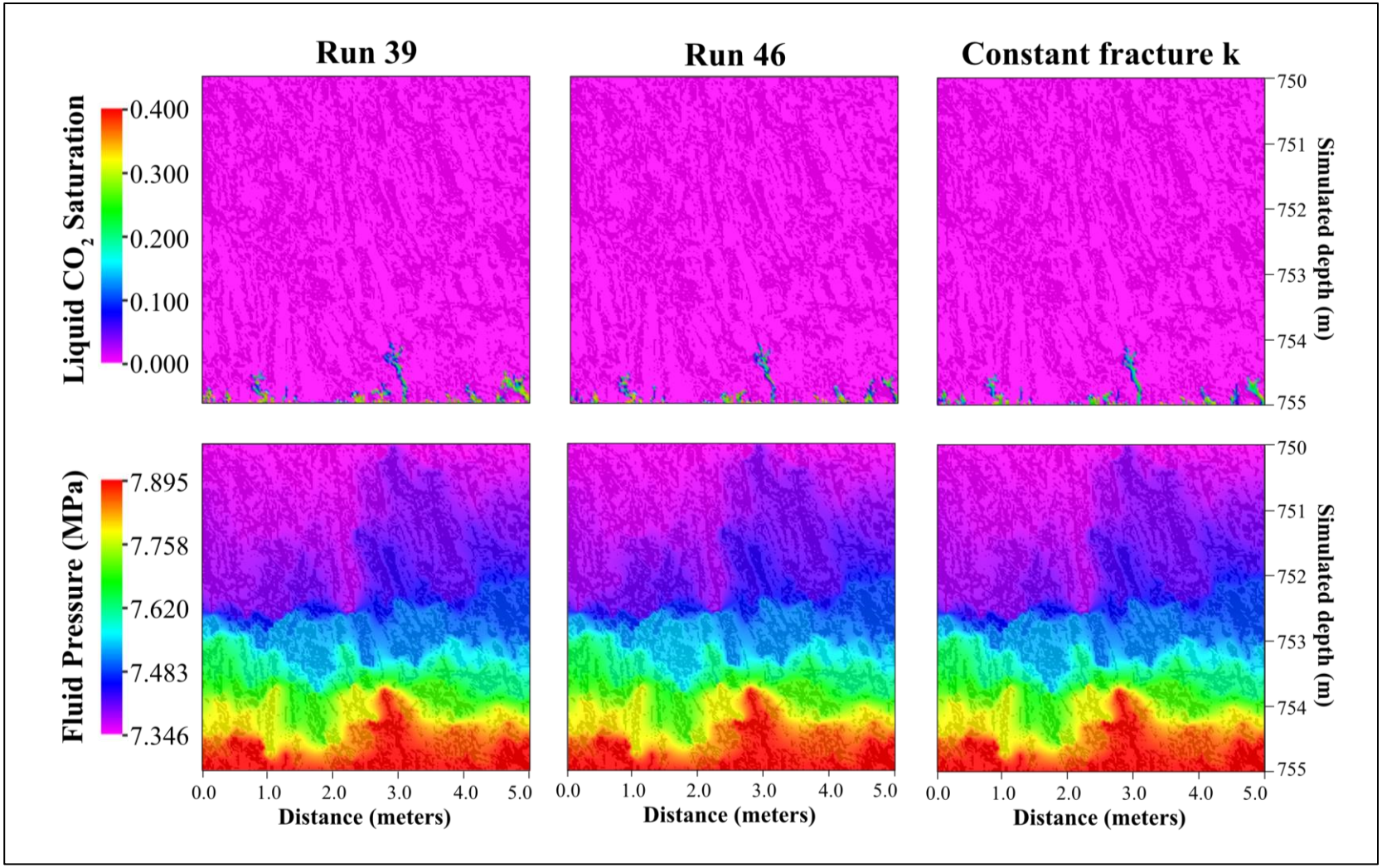

Figure 17: *Results for example simulation runs at 1 year. Fracture permeability is randomly assigned from lognormal distribution for Run 39 and Run 46, and constant in simulation with constant fracture permeability. Top row depicts liquid phase CO_2 saturation, bottom row depicts fluid pressure.*

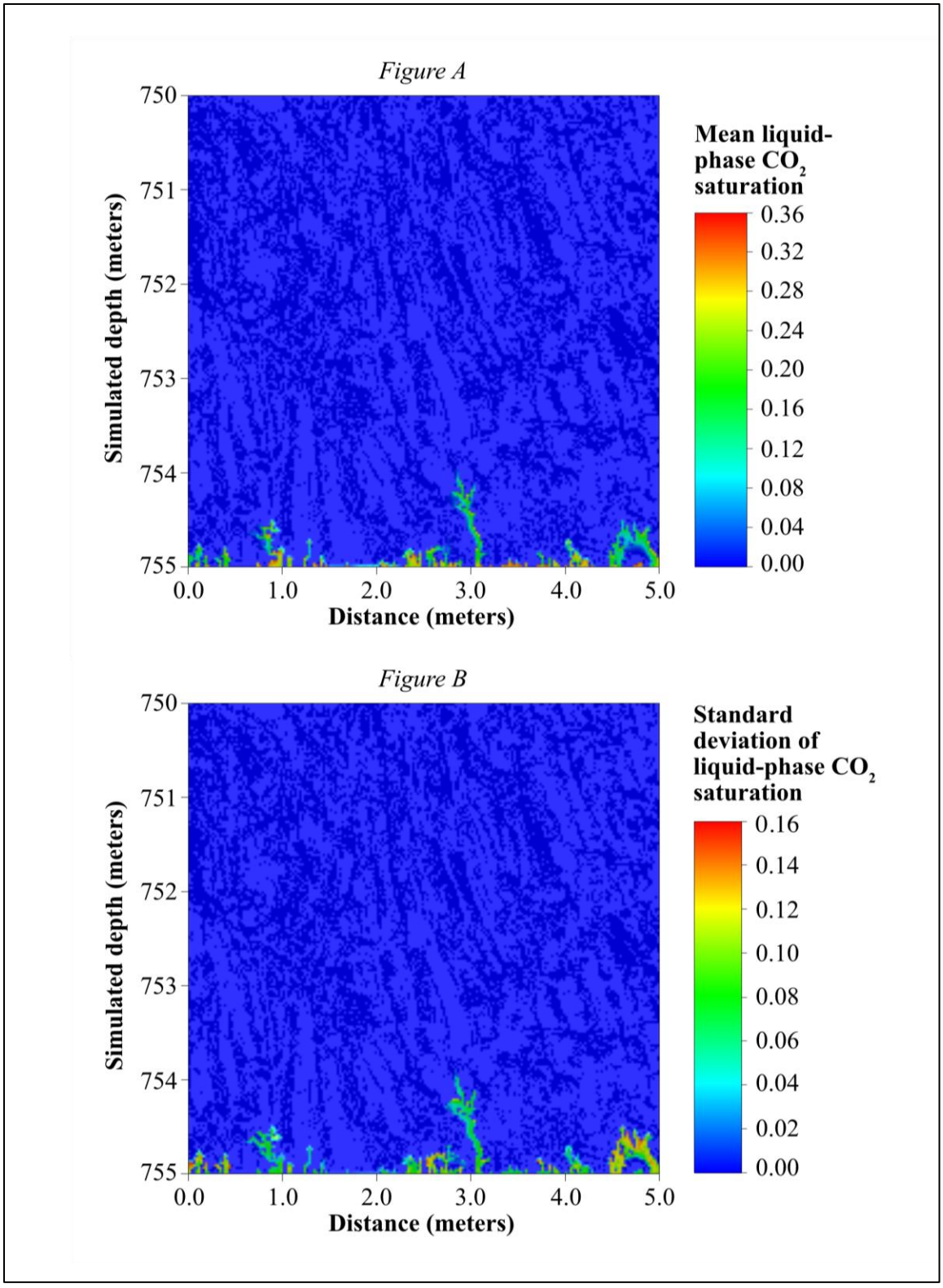

Figure 18: *E-type plots of CO_2 saturation at 1 year. Mean CO_2 saturation shown in Figure A, standard deviation of CO_2 saturation in Figure B.*

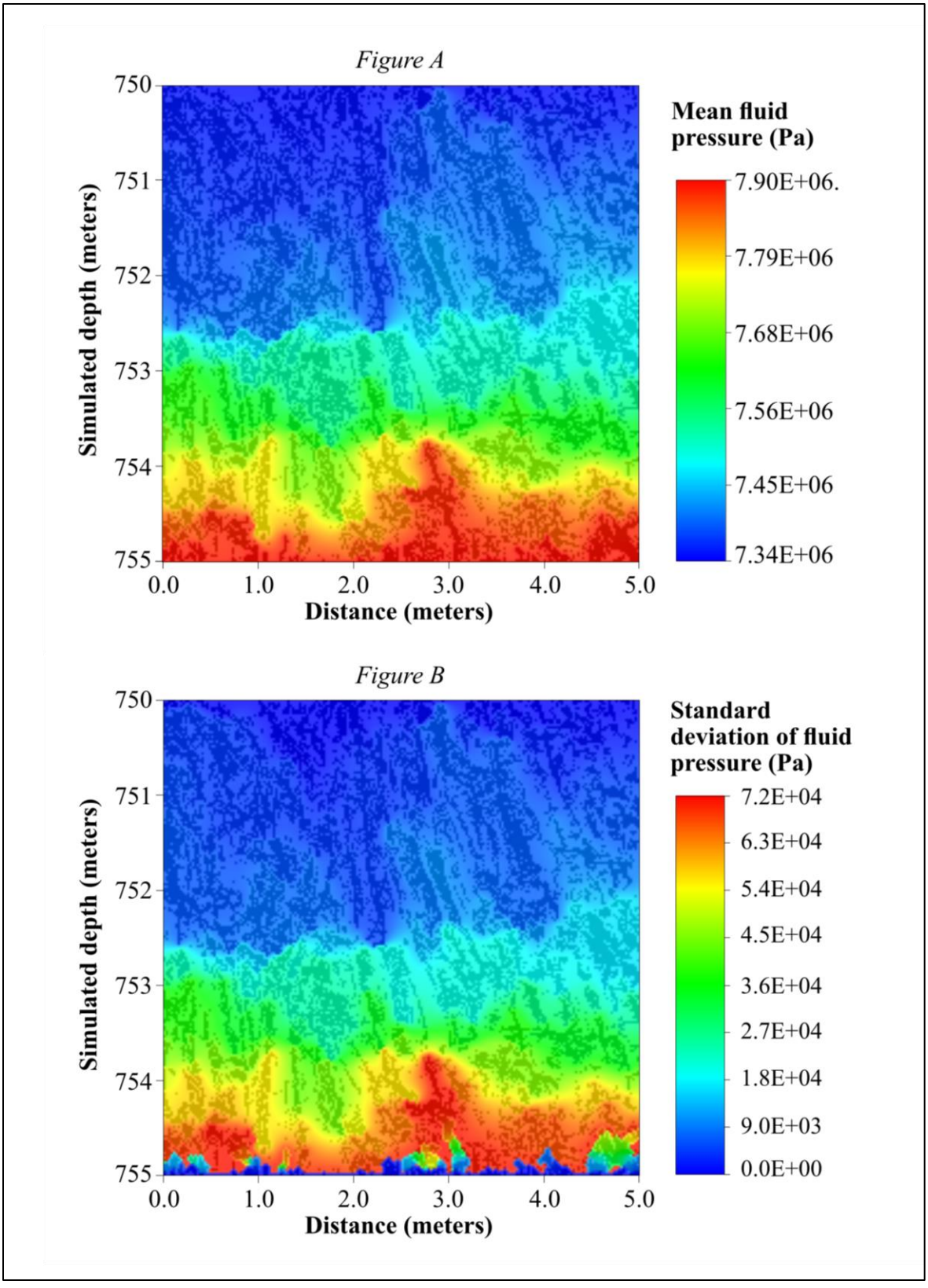

Figure 19: *E-type plots of fluid pressure at 1 year. Mean fluid pressure shown in Figure A, standard deviation of fluid pressure in Figure B.*

Results – Five Years

Results at 5 years for CO_2 saturation and fluid pressure for the example runs and for the model with constant fracture permeability are presented in Figure 20. As with the one-year time-step, the five-year time-step contains only supercritical liquid phase CO_2. In all three models, CO_2 follows similar paths, with several short fracture paths taking fluid to just below 754 meters depth, and two longer paths taking CO_2 higher. The maximum height of CO_2 is about 752.7 meters depth, reached in only the most central fracture channel. In each of the three simulations, the maximum rise of CO_2 occurs just below a dip in the fluid pressure, which is likely present due to the long, unobstructed fracture leading to the top of the domain, along which the pressure dip occurs. An unobstructed fracture path allows fluid pressure to dissipate along it, rather than build up behind a break in the fracture, which is what occurs in the fractures immediately to the left and right of this central passage. This dip is essentially identical between Run 39 and the constant fracture permeability run. However, in Run 46, the fluid pressure in the central fracture passage is slightly higher.

E-type plots for liquid phase CO_2 saturation and fluid pressure are shown in Figure 21 and Figure 22, respectively. The standard deviation of liquid phase saturation (Figure 21B) is fairly consistent, around 0.06-0.10 for most fractured cells that contain CO_2. Standard deviation is slightly higher at a few points due to spatial permeability distribution, but never exceeds 0.18. Mean liquid-phase saturation (Figure 21A) follows the same path as the example runs. Mean liquid saturation is highest at fractures close to the bottom of the model, and fractured cells just below a constriction in the flow path. Values along unobstructed flow paths tend to cluster around 0.20.

The e-type plot of the mean values of fluid pressure (Figure 22A) is similar to the e-type estimates after one year of simulation. Fluid pressure decreases non-linearly towards the top. Spikes in fluid pressure occur below where there is a break or constriction in the fracture pathway. The E-type plot of the standard deviation of fluid pressure (Figure 22B), however, is distinctly different from that of the one-year time step, with several localized zones of higher uncertainty in fluid pressure. All of these zones occur above long (>1.5m) CO_2-conducting channels, and below constrictions in the fracture pathway. The area with the highest deviation in fluid pressure, noted as 1 in Figure 22A, occurs just below a break in the main CO_2 conducting channel. The break only lasts for one or two cells, but the channel is much thinner once it picks

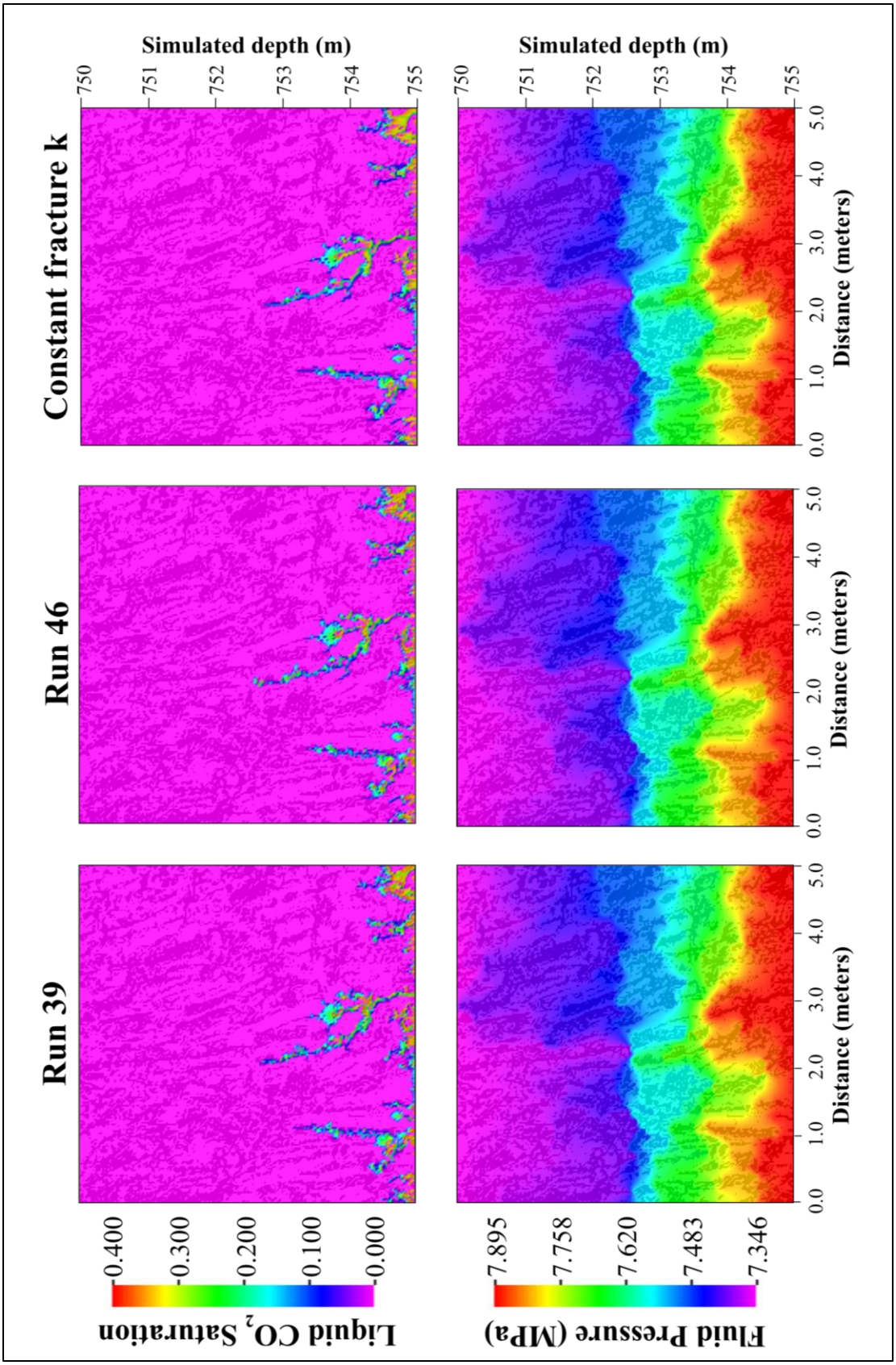

Figure 20: *Results for example simulation runs at 5 years. Fracture permeability is randomly assigned from lognormal distribution for Run 39 and Run 46, and constant for run with constant fracture permeability.*

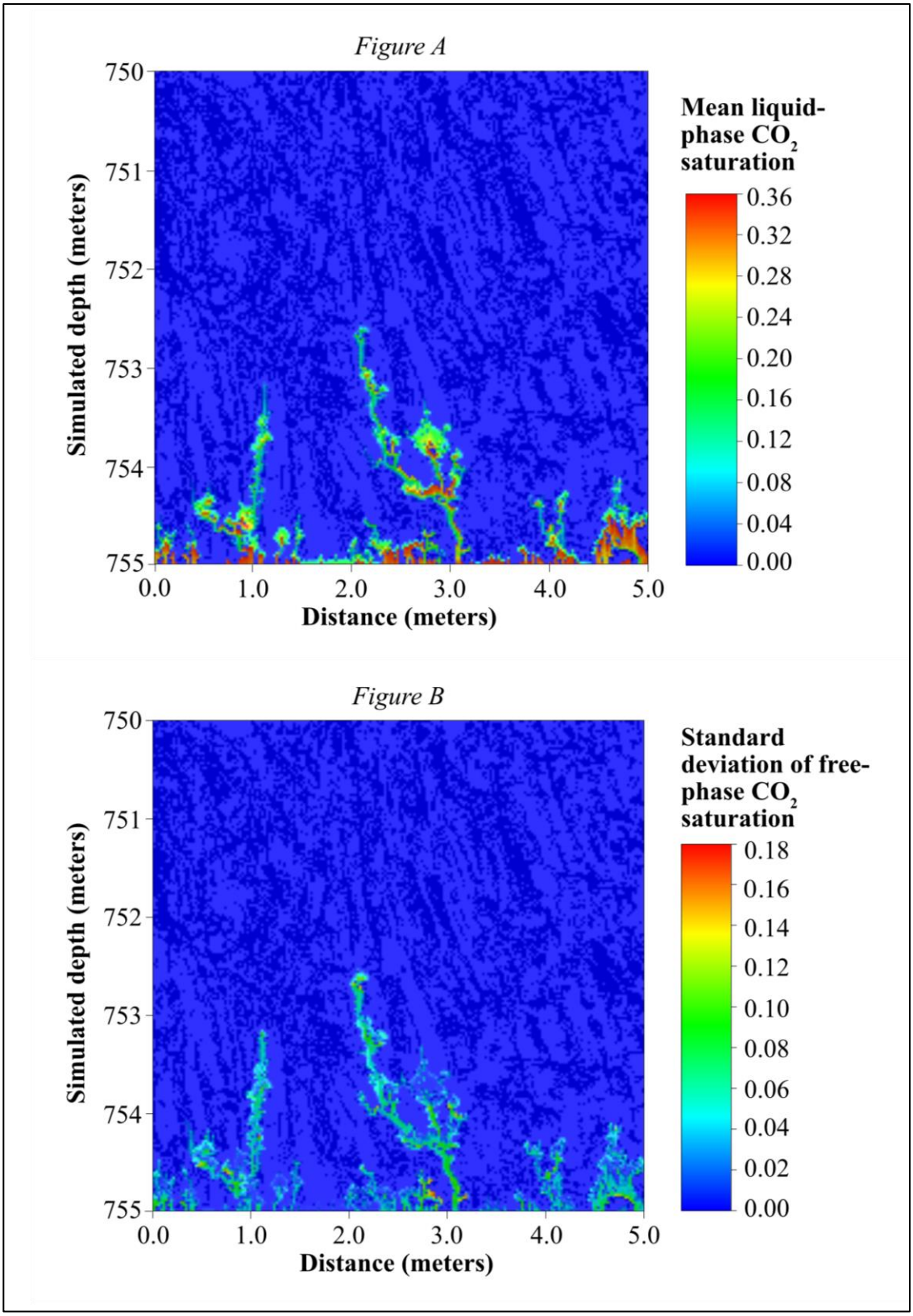

Figure 21: *E-type plots of CO_2 saturation at 5 years. Mean CO_2 saturation shown in Figure A, standard deviation of CO_2 saturation in Figure B.*

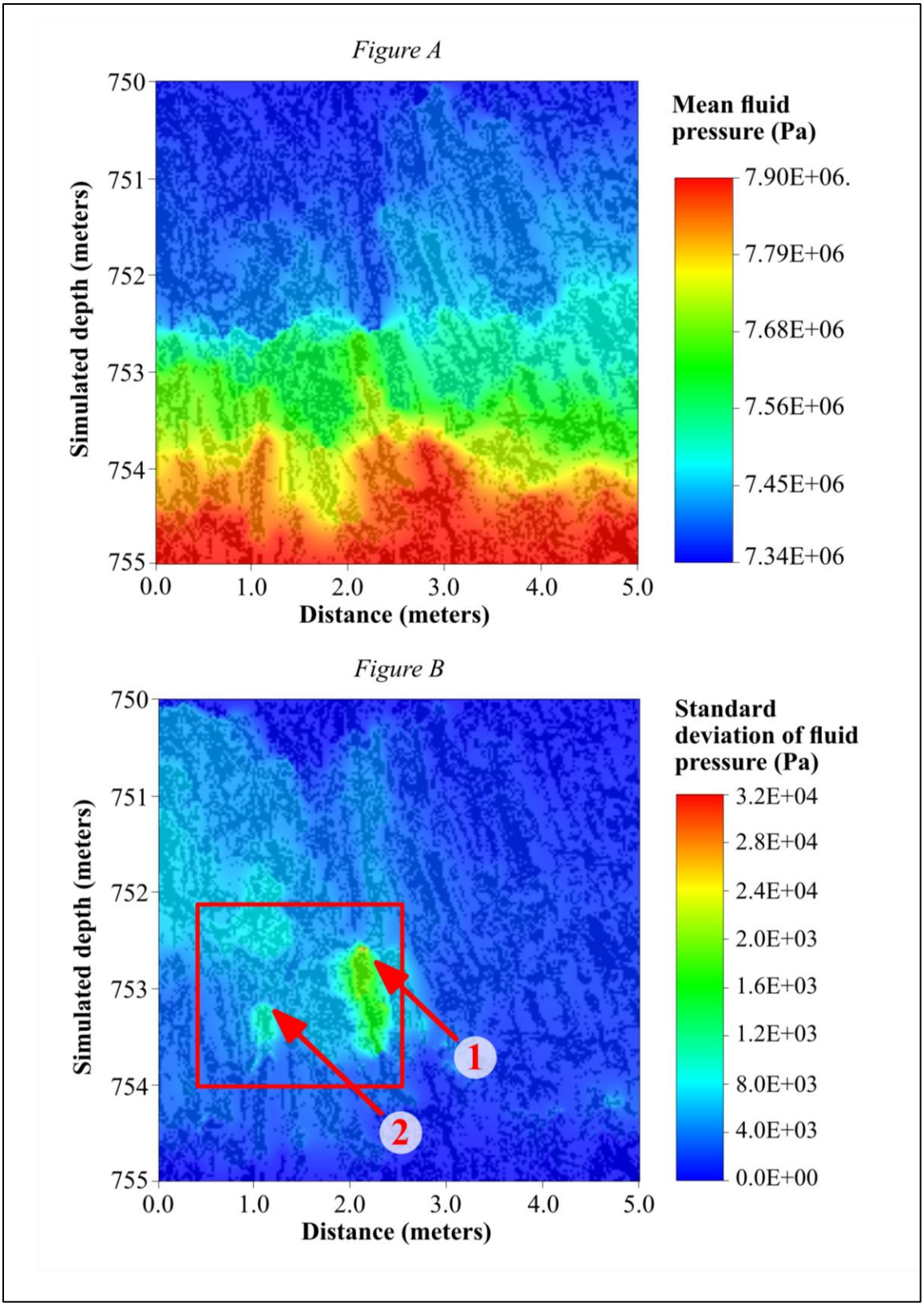

Figure 22: *E-type plots of fluid pressure at 5 years. Mean fluid pressure shown in Figure A, standard deviation of fluid pressure in Figure B. Red selection box highlights zone of maximum fluid pressure uncertainty. Numbered arrows indicate fracture constrictions where fracture permeability influences fluid pressure uncertainty in channel below.*

back up again. Permeability changes in these cells affect the ability for CO_2 to penetrate, and thus the amount of pressure that would accumulate at depth. Alternatively, permeability below the break could determine how much CO_2 arrives from below to pool at the break. The second most uncertain spot lies to the left of the main one, labeled as 2 in Figure 22B. This spot also lies just below a break in the fracture, along a main conducting pathway. The larger, more diffuse zones of uncertainty in the top left of Figure 22B overlie these main conducting pathways, and are sensitive to changes in pressure within those passages caused by changes to the permeability distribution.

Results - Ten Years

CO_2 saturation and fluid pressure for the two example runs and the run with constant fracture permeability for the 10-year time step are presented in Figure 23. After 10 years, three-phase CO_2 conditions exist in all of the models: aqueous, super-critical liquid, and the gas phase. In Run 39, the distribution of these phases is almost the same as the model with constant permeability, with the phase change occurring at about 752.2 meters depth. In Run 46, however, the phase change does not occur until about 750.9 meters depth. This difference in phase partitioning is caused by differences in the fluid pressure distributions of the three models. In Run 39 and the constant fracture permeability run, fluid pressure dips significantly along the central CO_2-conducting fracture pathway, causing the fluid pressure to be at the critical point deeper along this path than in most of the rest of the profile. This dip also occurs in Run 46, but to a much lesser extent – the fluid pressure is above the critical pressure for CO_2 much higher along the fracture pathway, delaying the phase change. The cause of this pressure backup is a constriction in the main CO_2 conducting fracture path just above where the dip occurs in both Run 39 and the constant fracture permeability run. This constriction, shown in Figure 22, blocks the upward migration water as rising CO_2 displaces it from below, then the upward migration of CO_2 as the liquid phase reaches the constriction. This allows pressure to build up behind the constriction, pushing fluid pressure above the critical point. Once the constriction is passed, fluid pressure is below the critical point, and fluid moves easily along an unobstructed fracture pathway to the top of the model. Other than the obvious differences in phase partitioning, however, the path the CO_2 takes to the surface remains similar in each of the three models.

E-type plots for the ten-year time step are presented in Figure 25, and Figure 26. The mean (Figure 25A) of the free-phase CO_2 saturation reflects the most likely path for CO_2 leakage through the model domain. Below about 752.5 meters depth, several paths exist for CO_2 to travel upwards. In most of the fractured cells below this depth, the saturation is around 0.20 to 0.24. In several places, however, notably near the base of the model and below breaks in the flow paths, the saturation is higher, between 0.32 and 0.40. Above 752.5 meters, saturation is generally lower, between 0.16 and 0.10, and CO_2 is confined to a single flow path with only a few very short branches. The standard deviation of free-phase saturation (Figure 25B) shows the same flow paths, with more variation along main flow paths below constrictions. The range of standard deviation is fairly consistent throughout the fracture network, with little difference above and below 2.5 meters above the base of the model. It is notable, however, that with lower mean concentrations above 2.5 meters, the standard deviation makes up a larger proportion of the total saturation in a cell. Additionally, the standard deviation shows a dead-end branch off of the main pathway occurring at around 4.7 meters above the base of the model that does not appear in the plot of mean values. This path therefore appears in a significant number of simulations, but not enough to affect the mean value of saturation in these cells. This kind of behavior may be important in the context of CO_2 leakage because relative permeability effects over longer time scales may permit non-negligible amounts of CO_2 to flow upward through the basalt flow interior. Mean values plotted for liquid and gas phase saturations (Figure 25C and Figure 25E respectively) show essentially the same patterns as the free-phase saturations. Both have lower mean values between 752 and 751 meters depth than the mean of free phase, however, because this zone is occupied by either liquid or gas depending on fluid pressure. Simulations where a phase does not occur in this zone lower the mean saturation of that phase. Plots of the standard deviation of the super-critical liquid (Figure 25D) and gas (Figure 25F) phase further illustrate this zone of overlap between the phases, with standard deviation in this zone between 0.05 and 0.10 for both. While the total CO_2 saturation present in these cells remains fairly consistent, the phase in which it occurs does not. The standard deviation of the free phase saturation in these cells is generally lower than the deviation of the phases separately. As a result, one important finding of this research is that fracture-scale permeability variability exerts a significant control on phase partitioning. Consequently, the vertical extent of this uncertainty is an important

criterion for assessing the trapping potential of basalt flow interiors prior to the onset of widespread mineralization.

The E-type plot of the mean fluid pressure (Figure 26A) for 10 years is overall very similar to the plot for 5 years. Pressure decreases non-linearly upward, with peaks occurring below breaks in fractures. Across all 50 simulations, a for a pressure drop is expected to occur in the central CO_2-conducting fracture, such that pressure in this fracture reaches the critical point at about 751.6 meters depth. The plot of the standard deviation of fluid pressure (Figure 26B) likewise continues the trends present at elapsed time of 5 years. The zone of uncertainty along the main flow path from 5 years remains at 10 years, located below a major discontinuity in the fracture labeled as 1 in Figure 26B. The bottom half of this zone shows more uncertainty than the top, which occurs just below a constriction one cell wide in the fracture path. Another distinct zone of uncertainty labeled as 2 in Figure 26B, occurs below a constriction that is 1-2 cells wide, at which CO_2 must travel at an angle to vertical. A more diffuse zone of uncertainty occurs throughout the fracture network, with highest uncertainty values occurring above fractures filled with CO_2. The highest uncertainty in this zone is located at 3 in Figure 26B, overlying fractures that conduct CO2 to its highest points in the model outside the main flow path.

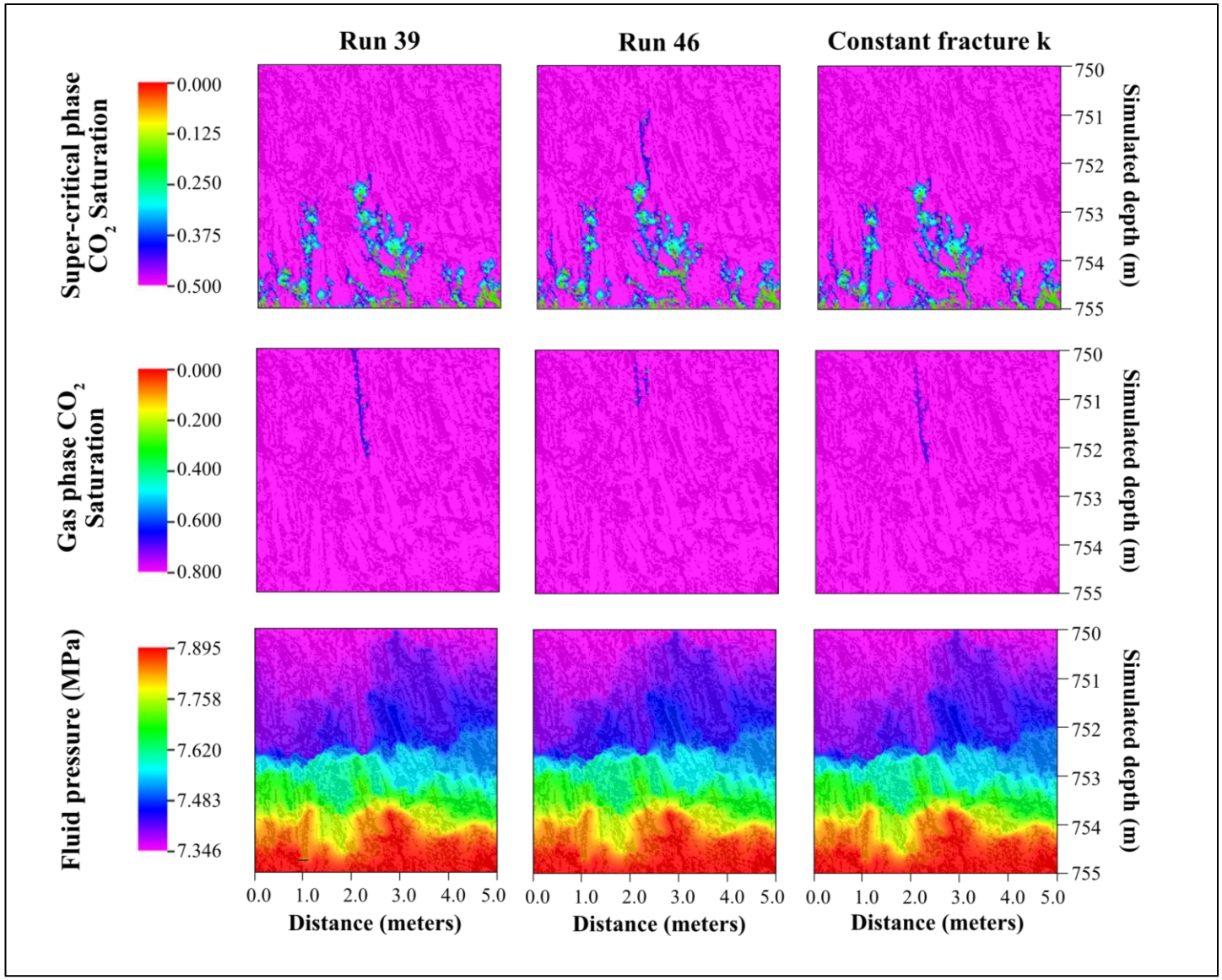

Figure 23: *Results for example simulation runs at 10 years. At this time, CO_2 undergoes a phase change from supercritical liquid to subcritical liquid and/or gas phase (both labeled as 'gas' in TOUGH3-ECO2M) as it reaches the critical pressure (7.39 MPa). Variations in distribution of fracture permeability across the runs affect the depth of the critical pressure.*

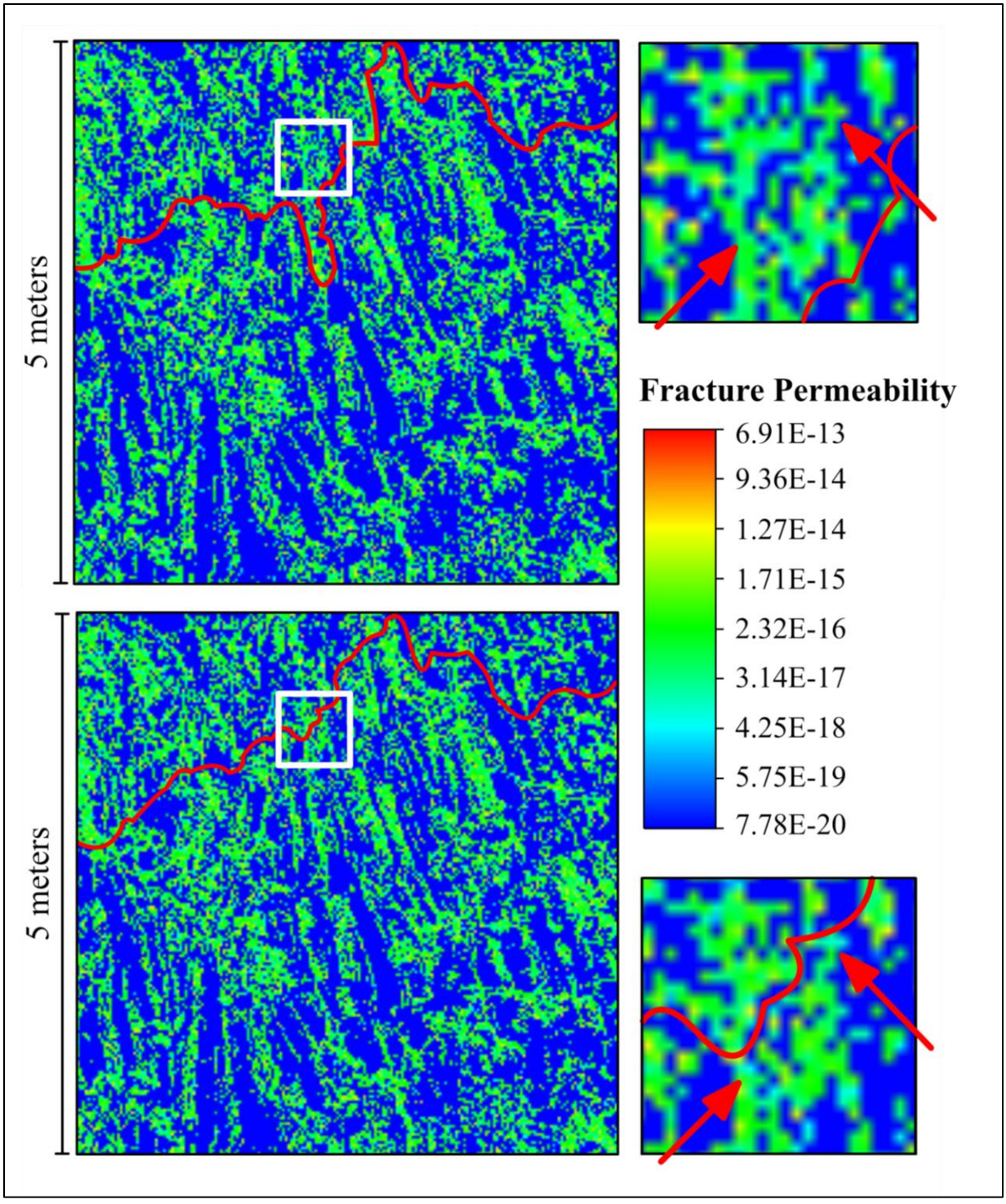

Figure 24: *Comparison of maps of spatial distribution of permeability for example runs. Run 39 shown in upper panels, Run 46 in lower. White boxes on left side are shown expanded on right side. Solid red line represents critical pressure for CO_2, 7.39 MPa. Red arrows indicate cells located at constrictions where fracture permeability is lower in Run 46 than Run 39.*

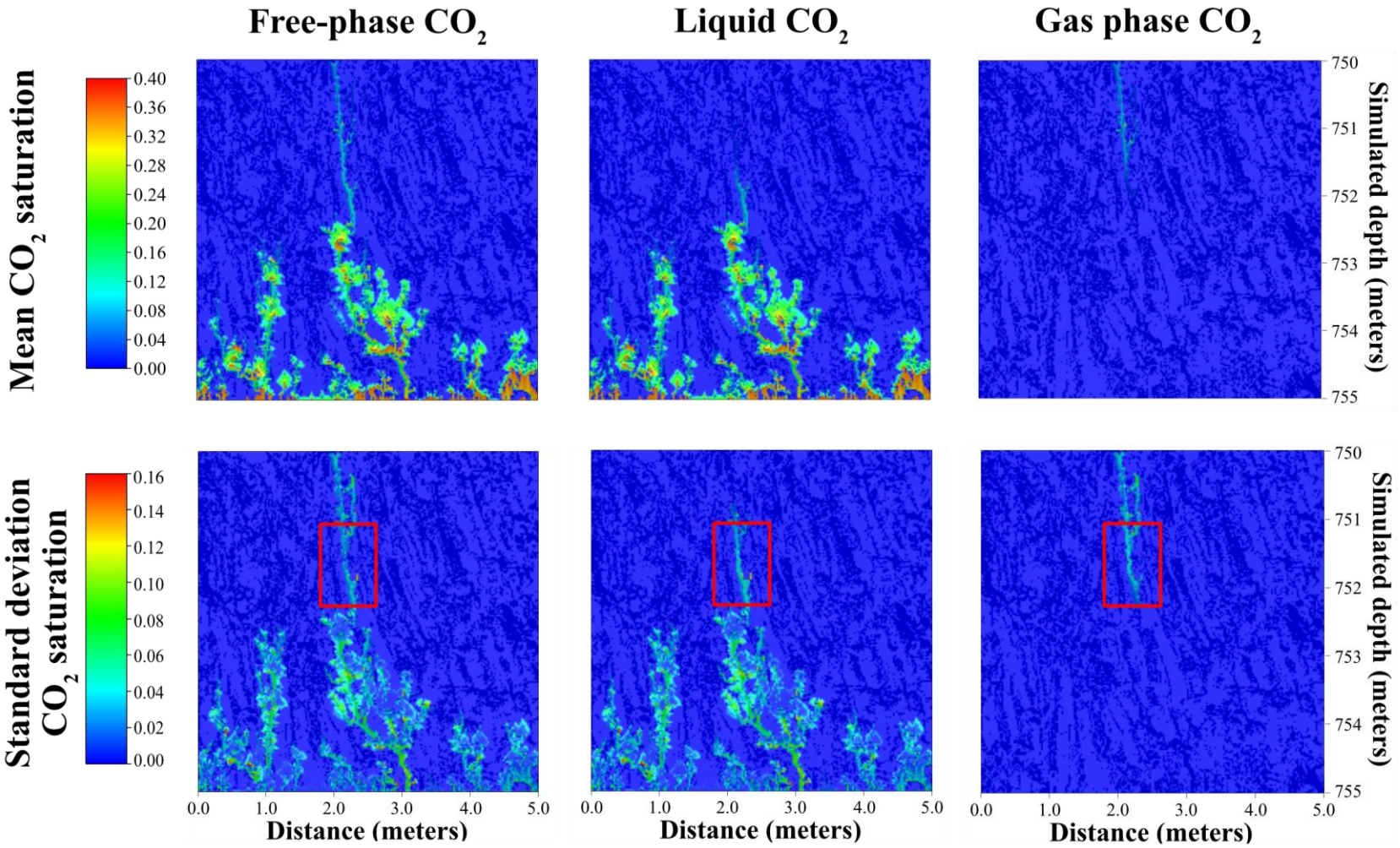

Figure 25: *E-type plots of CO_2 saturation at 10 years. Mean CO_2 saturation shown in upper panels, standard deviation in lower. Free-phase saturation is the sum of liquid phase and gas phase saturation. Red boxes in standard deviation plots indicate the range of depth (approximately 1.5 meters high) over which the phase change occurs across the 50 runs of the Monte Carlo simulation.*

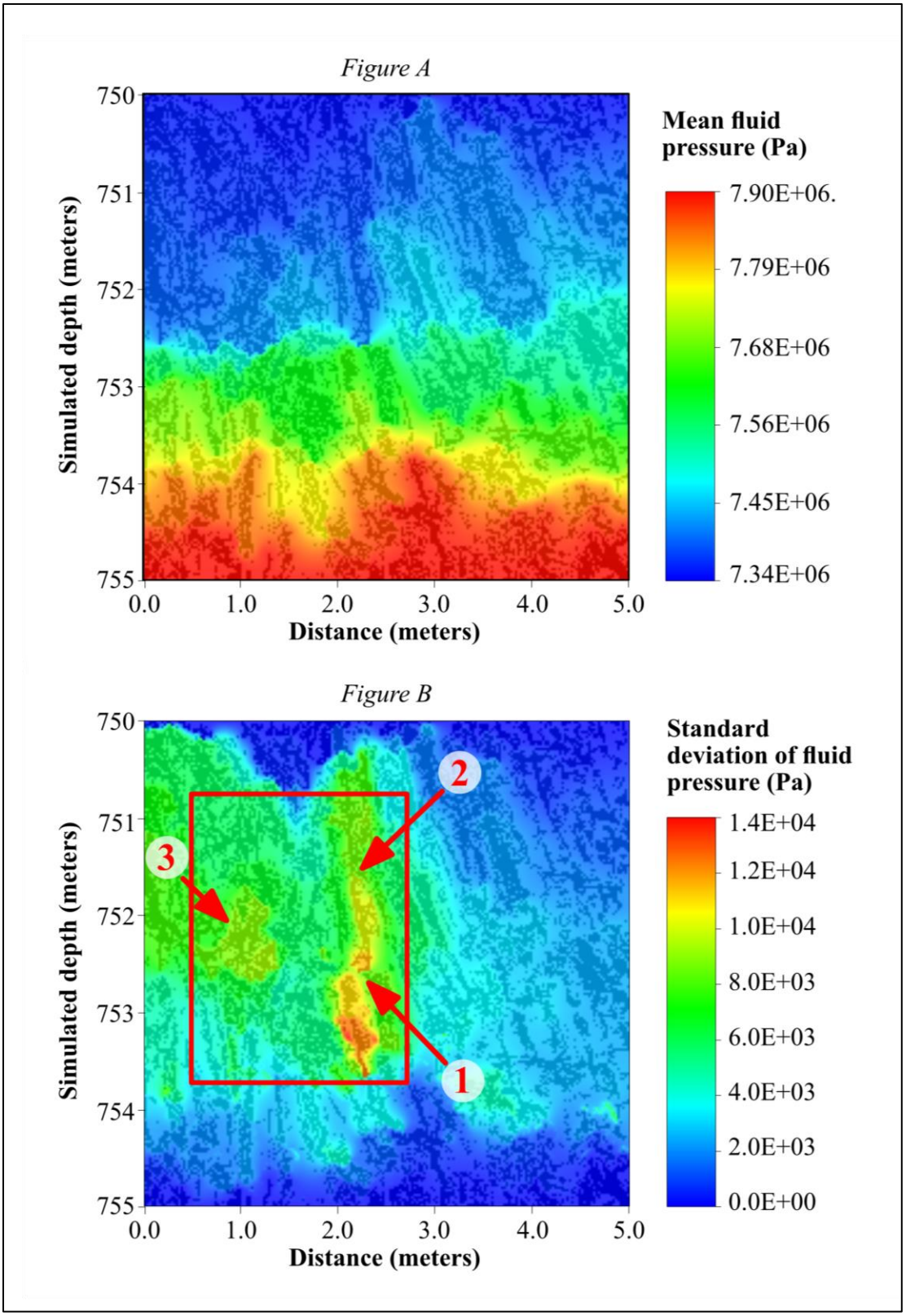

Figure 26: *E-type plots of fluid pressure at 10 years. Mean fluid pressure shown in Figure A, standard deviation in Figure B. Red box in Figure B surrounds zone of maximum fluid pressure uncertainty. Numbered red arrows indicate constrictions in fracture flow path where permeability influences fluid pressure uncertainty in channel below.*

CHAPTER 4: DISCUSSION

The goal of this research is to assess the effects of spatial variations in fracture permeability on estimates of CO_2 flow through a basalt fracture network during GCS. The results presented in the previous chapter indicate that variations in the distribution of fracture permeability affect both the total saturation of CO_2 at any point in the fracture network, and the phases in which that CO_2 occurs. Differences in phase partitioning seem to be largely due to effects of the permeability distribution on fluid pressure, which in turn affects where the critical point for CO_2 occurs in the model. The following discussion focuses on the reasons for this behavior, from the perspective of past studies in unsaturated, fractured basalt, and from the perspective of fluid flow in rough fractures. Variations in saturation and fluid pressure also change with increasing time, and as such the discussion also includes the ways in which temporal effects influence the uncertainty introduced by spatial variability in fracture permeability. The chapter then concludes with some recommendations for future work, and a brief summation of the findings of this study.

CO_2 Saturation

Figure 27 presents the e-type analyses of free-phase CO_2 saturation at 1, 5, and 10 years. Several things are notable about these plots, which agree fairly closely with conclusions drawn from literature (Glass et al 2003, Zhou et al 2006, Carniero 2009, Wood et al 2004, Kwicklis and Healy 1993): much of the network is non-conducting, flow always converges on a single path regardless of permeability distribution, and while the range of mean and variability of CO_2 saturation remain fairly constant with elapsed time, their distribution changes throughout the 10 years of simulation time in interesting ways.

The first important point to note in Figure 27 is that at each time-step, much of the fracture network is not involved in conducting CO_2 through the fracture network. Non-conducting fractures take two forms in this model: fractures that do not conduct CO_2 because they are not connected to CO_2 conducting fractures, and fractures that do conduct CO_2 but are not hydraulically connected to other fractures leading to the surface. The first category, fractures that lack connections to CO_2-conducting fractures, are not directly important to the leakage of CO_2 through the fracture domain. However, they do play a role in the distribution of fluid

pressure within the model, since these fractures still receive water displaced by incoming CO_2 in conducting fractures. Their ability to accept this incoming water without excessive pressure buildup depends on their permeability, and on their connectivity to fractures higher in the domain. Pressure buildup in some of these fractures did occur (Figure 27), however not to the extent where it might induce hydrofracture or fracture dilation. This is perhaps due to fairly high concentration of fractured cells in the zone in question, which allowed fluid pressure to disperse more quickly than it would have in unfractured basalt. While pressure buildup in these fractures was not extreme in these simulations, this is a potential problem that deserves attention, since hydrofracturing is always a concern with injections into geologic formations (Mortezaei and Vahedifard 2015). Should hydrofracturing occur, fractures would become more interconnected, introducing more and potentially faster paths for CO_2 leakage.

The other type of non-conducting fractures in these experiments consisted of fractures that do conduct CO_2, but not along a flow path that leads to the surface. At 10 years, these zones are mainly located from 0.0-2.0 meters and 3.5-5.0 meters on the x-axis. Additional non-connected fractures occur off of the main flow path, and whether or not they contain CO_2 changes depending on the distribution of fracture permeability. One such example appears in the 10-year time step, from 750.2 to 751.2 meters simulated depth along the main flow path. This dead-end fracture conducts fluid in some simulations but not others, as evidenced by the fact that it appears in the plot of standard deviation values but not in the plot of mean values for free-phase CO_2 saturation. While non-globally connected fractures such as this do not contribute to leakage through the basalt formation, they remain an important factor in determining leakage rates by acting as diffusive sinks (Glass et al 2003). This is because non-conducting fractures will divert portions of upwelling CO_2 into dead-end flow paths, where the CO_2 can safely follow the mineralization path outlined in McGrail et al (2006). Entering more of these fractures also increases the reactive surface area to which the CO_2 is exposed, which will further increase mineralization rates. Even without mineralization, however, non-conducting fractures might block a significant portion of upwelling CO_2. For example, in an infiltration experiment in fractured tuff at Yucca Mountain, Zhou et al (2006) observed that while infiltration increased rapidly within the first 30 days, it eventually reached some slower steady state. At this quasi-steady state, only about 10% of water that infiltrated was able to leave the fractured rock, with much of the fluid trapped in fractures that were not globally connected (Zhou et al 2006). While

infiltration is not a precise analogue for buoyant CO_2 entering a fractured rock, much of the same behavior applies, if hydrofracturing does not occur. One might therefore expect similar trapping rates of rising CO_2, with only a small percent of the fluid entering the entablature able to escape on the other side. Increasing the surface area to which CO_2 is exposed also offers the potential of more matrix diffusion for CO_2 that is dissolved in the aqueous phase (Carniero 2009). Diffusion of aqueous-phase CO_2 into the matrix allows more CO_2 to dissolve in the fractures, and slower velocities within the matrix due to lower permeability increase the residence time of CO_2 in the rock (Carniero 2009). Increased residence time of CO_2 allows more time to dissolve cations from the basalt, which would increase mineralization rates. The distribution of fracture permeability, by effectively opening or closing access to dead-end fractures, plays a role in determining what proportion of the fluid entering the formation is able to escape through the dominant leakage pathway. While any amount of leaking CO_2 defeats the purpose of GCS, the fact that flow through the entire entablature tends to be localized is encouraging. If only a few pathways lead to through the confining layer, the confining layer may be more easily sealed by the precipitation of carbonate minerals.

The second major observation about the e-type analyses of free-phase CO_2 saturation shown in Figure 27 is that there does appear to be a single flow path through which CO_2 travels in every simulation. This indicates that in a basalt entablature, connectivity of the fractures plays a larger role in determining flow path than the distribution of permeability within the fractures. This makes sense, given the significant permeability difference between the fracture infill and the unfractured basalt. While the aperture of the fracture may locally increase or decrease the velocity of the fluid, its direction is ultimately governed by boundaries that are more difficult to cross, the fracture walls. The existence of a single flow path is also consistent with experimental results in fractured rock, which suggest that flow through a fracture network tends to converge on a single path during infiltration (Wood et al 2004). Again, infiltration is not a perfect analogy, and convergence in this case is more likely due to the position of fractured cells as governed by the roughness map. However, this suggests that this single flow path may be a realistic representation of how fluid would flow through an entablature network, with conditions along a single primary path governing much of fluid behavior. This is an important connection to draw, because while the distribution of fracture permeability had little effect on the paths taken by upwelling CO_2, it did affect phase and pressure conditions within those paths.

The final points to consider in analyzing the e-type plots of free-phase CO_2 saturation are the ways in which the distribution of the average and standard deviation of CO_2 saturation within the network changed with time. Analysis of mean CO_2 saturation at 1, 5, and 10 years in Figure 27 reinforce the fact that in all 50 simulations, CO_2 travelled along roughly the same flow paths. From the first year, the most dominant flow path is located at about 3.0 meters on the x-axis, with secondary paths at 1.0 meters and 4.8 meters. At 5 years the CO_2 reaches the highest points in fractures located at 3.0 meters and 1.0 meters on the x-axis; finally, at 10 years, the fractures beginning at 3.0 meters on the x-axis become the dominant flow path, with CO_2 travelling all the way to the top of the domain. At this time, the secondary path in which CO_2 travels the highest is the one located at 1.0 meters on the x-axis, reaching the simulated depth of about 752.8 meters below ground surface. At each time-step, the highest mean values of saturation occur in these fractures below blockages in the fracture, where matrix cells briefly interrupt a path of fractured cells, or below fracture intersections. Interruptions in the fracture flow path by matrix cells block the upward movement of CO_2, forcing CO_2 to pool behind the blockage until it reaches sufficient pressure to overcome the barrier. This behavior is not necessarily physically realistic, since CO_2 is not expected to readily flow through the matrix of dense basalt. However, these blockages are analogous to sharply constricted apertures, which certainly occur in a real fracture network. CO_2 also tends to pool behind fracture intersections, which is consistent with infiltration studies of water into unsaturated fractures (Wood et al 2004, Glass et al 2003). Glass et al (2003) found that infiltrating water proceeds in narrow fingers into an unsaturated network until it reaches an intersection, where it backfills to the full width of the fracture and piles up until force is sufficient to overcome the capillary barrier of the intersection. Wood et al (2004) performed a similar study, finding that overcoming capillary barriers at intersections resulted in pulses of fluid. In the results shown in Figure 27, at several points it is difficult to separate the effects of fracture interruptions from capillary barriers at intersections, since many intersections also contain interruptions. However, the location of high mean saturation values at intersections is logical, regardless of which mechanism is causing them. Other high mean values are located in fractures that are not globally connected. As mentioned previously, these fractures play an important role in reducing leakage, and perhaps encouraging matrix diffusion.

The plots of standard deviation of free-phase CO_2 saturation show some variation throughout nearly the entire flow path of CO_2 in the model. This demonstrates the fact that the

response at any given point is dependent on the properties of the entire flow path (Doughty 2000). While CO_2 takes roughly the same path in each case, the saturation value at any given point is dependent on the permeability along the entire path it takes to get to that point. Since permeability varies randomly in space, there will be some degree of variation in saturation throughout the model at all points along the flow path. The amount of variation, however, in many cases decreases the longer a fracture is occupied by CO_2. Most fractures occupied by CO_2 at 1 year have lower standard deviation at 5 years, and most fractures occupied at 5 years have slightly lower standard deviation at 10 years. That variation in saturation between simulations would decrease with time is logical, since the flow path becomes longer with time, meaning that extremely high and low permeability values along it have less effect on the overall permeability of the path. This idea is also borne out by the standard deviation of CO_2 saturation along the main flow path from about 752.5 to 750 meters simulated depth, which represents the longest uninterrupted section of CO_2-conducting fractured cells. Standard deviation of free-phase CO_2 saturation is generally low within this zone, indicating an averaging effect of permeability values along this long flow path. Another feature present at 5 and 10 years is that the areas with highest mean free-phase saturation generally have the lowest standard deviation. The lower standard deviation in fractures with high mean saturation also makes sense, given high mean values correspond to features that are always present in the model, fracture interruptions and fracture intersections. Overall, these results agree with previous studies of flow in a network with variable aperture, which find that flux tends to vary spatially within a network of variable aperture, even at conditions of steady flow (Kwicklis and Healy 1993). From Figure 27, it is clear that this variation occurs throughout all of the conducting fractures in this model, although the extent of the variation changes both spatially and temporally.

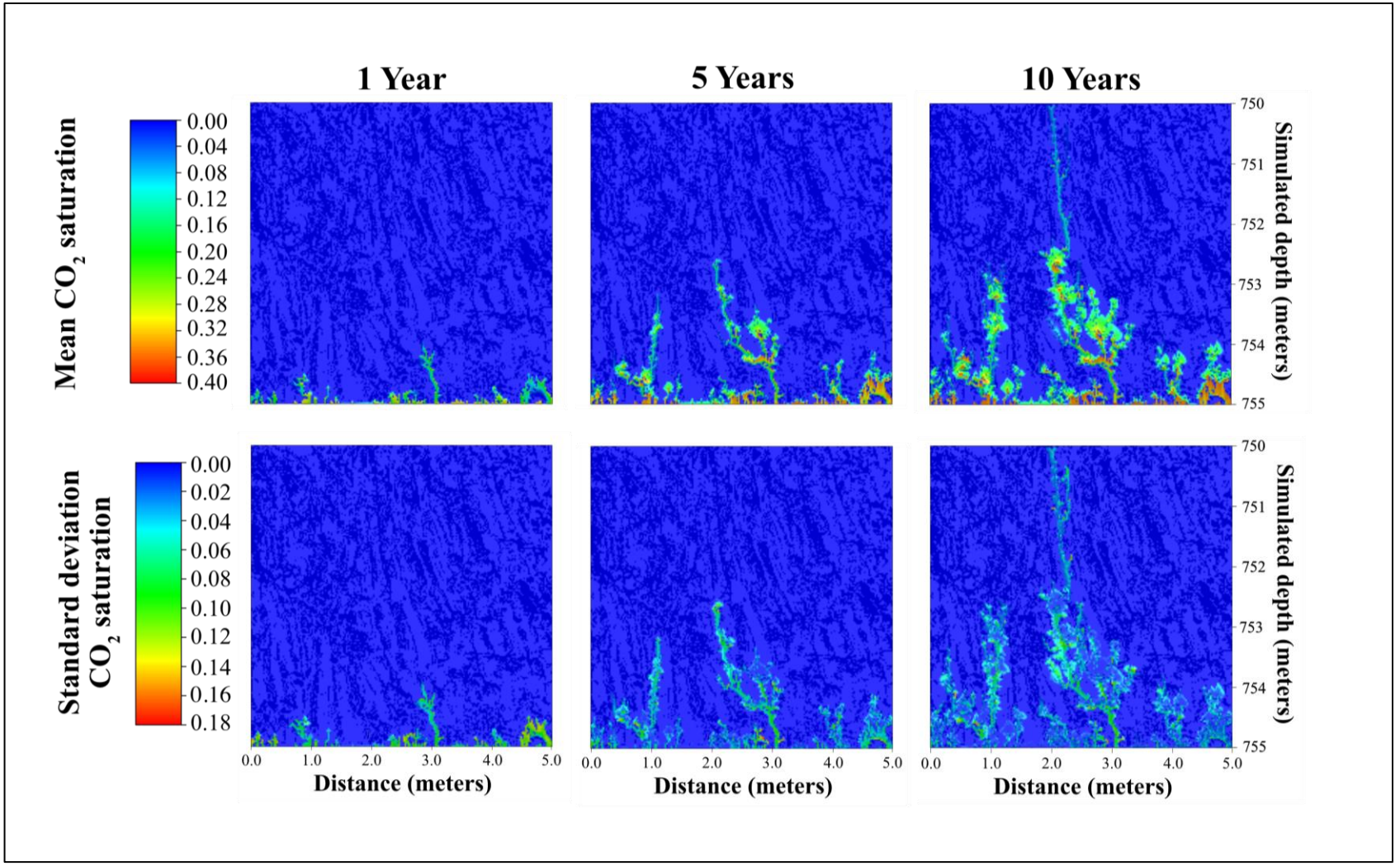

Figure 27: *Mean and standard deviation of free-phase CO_2 saturation at 1, 5, and 10 years. Free phase refers to the sum of super-critical liquid phase and gas phase CO_2.*

Fluid Pressure

Figure 28 presents the e-type analyses of fluid pressure at each time step, 1, 5, and 10 years. Both the mean and standard deviation of fluid pressure are shown, presenting a picture of the variability in fluid pressure over time due to uncertainty in the distribution of fracture permeability. Several features on these plots are notable, including the evolution of the mean fluid pressure with time, the evolution of the standard deviation in fluid pressure with time, and the relationship between fluid pressure and the path that CO_2 takes traversing the model domain.

Throughout the 10 year run of this model, the mean fluid pressure profile remains fairly consistent – pressure always decreases towards the top of the model, with the elevated fluid pressure values occurring just below interruptions in CO_2-conducting fractures. Conversely, fluid pressure tends to be lower below sections with high concentrations of fractured cells, or especially below long, unobstructed fractures. This pattern results in a jagged appearance to fluid pressure contours, and is logical considering that CO_2 and formation waters displaced by CO_2 will back up behind the low-permeability matrix cells, and move more freely through higher-permeability fractured cells. While the mean fluid pressure profiles for 1, 5, and 10 years are more similar than not, the overall profile does evolve somewhat. As more fluid is displaced by incoming CO_2, pressure below fracture interruptions increases slightly from 1 year to 5 years in the lower quarter of the domain, and very slightly throughout the domain from 5 years to 10 years. The range of mean fluid pressure values remains essentially the same throughout the 50 simulations. This striking similarity over the course of the simulation time indicated that despite local differences visible in comparing individual simulations, or in the plots of standard deviation, the distribution of fluid pressure over time was governed to a greater extent by the distribution of fractured cells than by the distribution of fracture permeability.

To say that the distribution of fractured cells has more effect on the fluid pressure than the distribution of permeability within the fractured cells does not negate the variation introduced by fracture permeability. As is clearly visible in Figure 28, the variation in fracture permeability does have and effect on the fluid pressure – up to 0.072 MPa at 1 year, 0.032 MPa at 5 years, and 0.014 MPa at 10 years. These values are relatively small compared to the range of mean fluid pressure, which covers 0.56 Mpa, but they are enough to affect the depth at which the phase change occurs. The evolution of standard deviation of fluid pressure with time is therefore useful in examining the effects of spatial permeability uncertainty in this fracture network. At 1 year,

for example, simulations already exhibit variability from the mean. This early in the simulation, deviation in fluid pressure is high, and very diffuse throughout the model. With extremely short flow paths, rising fluid is greatly affected by extremely high or low permeability values along the fracture, and these differences result in more variation in pressure. For example, the highest variation in fluid pressure at this time occurs just above CO_2-conducting fractures, and decreases upwards. As formation water is displaced over short distances by the short rise in CO_2 (less than 1 meter rise), the variation in permeability has a large effect on the deviation in fluid pressure. Interestingly, the standard deviation of fluid pressure within CO_2-conducting fractures is lower than the surrounding area, because flow is more localized. Even within this zone of lower deviation, however, standard deviation increases higher in the flow path. Once again this makes sense, since the entire flow path affects the conditions at any point in the fracture (Doughty 2000). These fractures are long enough to experience variation due to fracture permeability, but not long enough for averaging effects to draw their fluid pressure values closer together.

As time progresses in the model, deviation in fluid pressure becomes less diffuse, with deviation converging to zero in much of the domain. Instead of following the same trend as mean fluid pressure, as it did at 1 year, deviation at 5 years is localized mainly in a few areas. As discussed in the results section, the most concentrated zones of uncertainty occur along the main and secondary flow paths, just below interruptions in CO_2-conducting fractures. This deviation is most likely due to variations in permeability along the path leading up to the interruption, with different amounts of CO_2 arriving at the barrier by 5 years simulation time to exert different amounts of pressure. The maximum standard deviation occurs at the very tip of this zone, in a fractured cell located in the middle of the interruption in the fracture pathway. This cell has the highest uncertainty because its fluid pressure depends on whether the fluid pressure along the pathway leading up to it is sufficient to force CO_2 through matrix cells to reach it, and whether the fluid pressure of arriving CO_2 is sufficient to force flow from this point to the other side. The maximum deviation in fluid pressure is lower at 5 years than at 1 year, most likely due to the fact that fluid is displaced over greater distances, so that local variations in permeability have less of an effect. The more diffuse zone of permeability in the upper left-hand section of the domain reflects formation water displaced vertically from the secondary flow path, with a smaller contribution from the primary flow path. Pressure deviation is lower in this zone than it is in the

actual flow paths, however, due to fairly good hydraulic connection between fractured cells in this zone.

These trends continue at the 10-year time step, with high uncertainty confined almost exclusively to the main flow path, and an expansion of the diffuse uncertainty zone from the 5-year time step to cover much of the left side of the model. This expansion reflects the continuing displacement of formation water as CO_2 continues to fill fractured cells in the secondary pathway, and begins to intrude into matrix cells (Figure 28). The uncertainty along the main flow path is caused by several factors: the permeability of cells in the path leading up to interruptions in the fractured cells, the permeability of cells at certain key points, and the presence of a phase transition within the fracture. The first factor controls the fluid pressure in about the bottom third of the zone, and is the same one responsible for the uncertainty in the same area at 5 years: variable amounts of CO_2 reach the interruption located at about 752.8 meters simulated depth, controlled by the permeability along the flow path to that point. The second factor is likely the primary control on uncertainty in the upper two-thirds of the zone. This zone may be divided roughly in half, into a lower zone with higher uncertainty ending at about 751.6 meters simulated depth, and an upper zone with lower uncertainty ending at about 750.8 meters simulated depth. Both zones are located below constrictions one cell wide in the fracture – these single-cell fracture openings have a disproportionate influence on the fluid pressure in the cells below them. If permeability is low in these cells, they can block upward-moving fluid, causing pressure to build up behind them. Figure 24 demonstrates this behavior in two example runs. In one run, permeability is lower at the constrictions, causing pressure to back up behind them, and in the other, higher permeability allows fluid to proceed freely, and no such pressure buildup is seen. While Figure 24 only demonstrates this behavior for the uppermost uncertainty zone in Figure 28, the same thing likely occurs in the middle one. This behavior also likely dictates the elevated uncertainty in the yellow part of the diffuse uncertainty zone located in the top left of the model, except instead of blocking upward-mobile CO_2, the constrictions are blocking displaced formation waters. The final cause of uncertainty in the main fracture pathway is the presence of a phase change, and is a major contributor to the uncertainty in the middle third of the main uncertainty zone at 10 years. At this time, as seen in Figure 25, CO_2 occurs in this zone as either super-critical liquid phase CO_2, or as gas phase CO_2, which may include both sub-critical liquid and gas phase CO_2. The result of this phase change is an expansion of CO_2 over this interval,

which will increase fluid pressure (Pruess 2005). Not only does the expansion of the CO_2 affect fluid pressure, but the presence of a 3-phase zone may further block upward-mobile CO_2, causing buildup behind it (Pruess 2005). Therefore, the presence of the phase change in the middle portion of the uncertainty zone not only affects the fluid pressure within that section, but may also play a role in the uncertainty present in the zone directly below. It is difficult to separate the effects of these various factors; however, the fact that such uncertainty exists is a clear indication that the spatial distribution of fracture permeability does affect the fluid pressure during leakage of CO_2 through an entablature network. The permeability of the fracture along the path dictates the fluid pressure below an interruption in the fracture, the permeability of cells at constrictions in the fracture affect the fluid pressure below the constriction, and the fluid pressure, as determined by these factors, determines the position of the phase change. Where the phase change occurs in turn affects the fluid pressure in the segment in which it occurs, and in the segment directly below.

The results presented above, both in terms of the distribution of free-phase CO_2 saturation and fluid pressure, suggest that at the small scale, spatial uncertainty in fracture permeability introduces variations in simulated leakage through basalt flow interiors at short (< 10 year) time-scales. While fracture geometry is more important to both the ability of CO_2 to fully penetrate a flow interior and the paths it may take, spatial permeability distribution exerts some control on which non-globally connected fractures will conduct CO_2, and on the location of the phase change within the flow interior. This has important implications for field-scale modeling, since non-globally connected fractures control how much CO_2 is physically trapped in the rock with no path upward. Furthermore, the location of the three-phase zone influences fluid pressure above and below it (Pruess 2005), and the phase of the CO_2 will potentially alter its ability to penetrate tight fractures (Edlmann et al 2013). Trapping within non-interconnected fractures will increase CO_2 residence time within the flow interior, thus encouraging mineralization. Additionally, alteration of fluid pressure within interconnected flow paths due to the presence of the phase change will move the 3-phase zone upward, further changing the fluid pressure distribution (Pruess 2005). Since permeability variations along a flow path have less effect in longer flow paths, further research should focus on the effects of permeability uncertainty in a larger fracture set, in order to determine whether variations in fluid pressure introduced by fracture permeability still affect the location of the phase change at a larger scale.

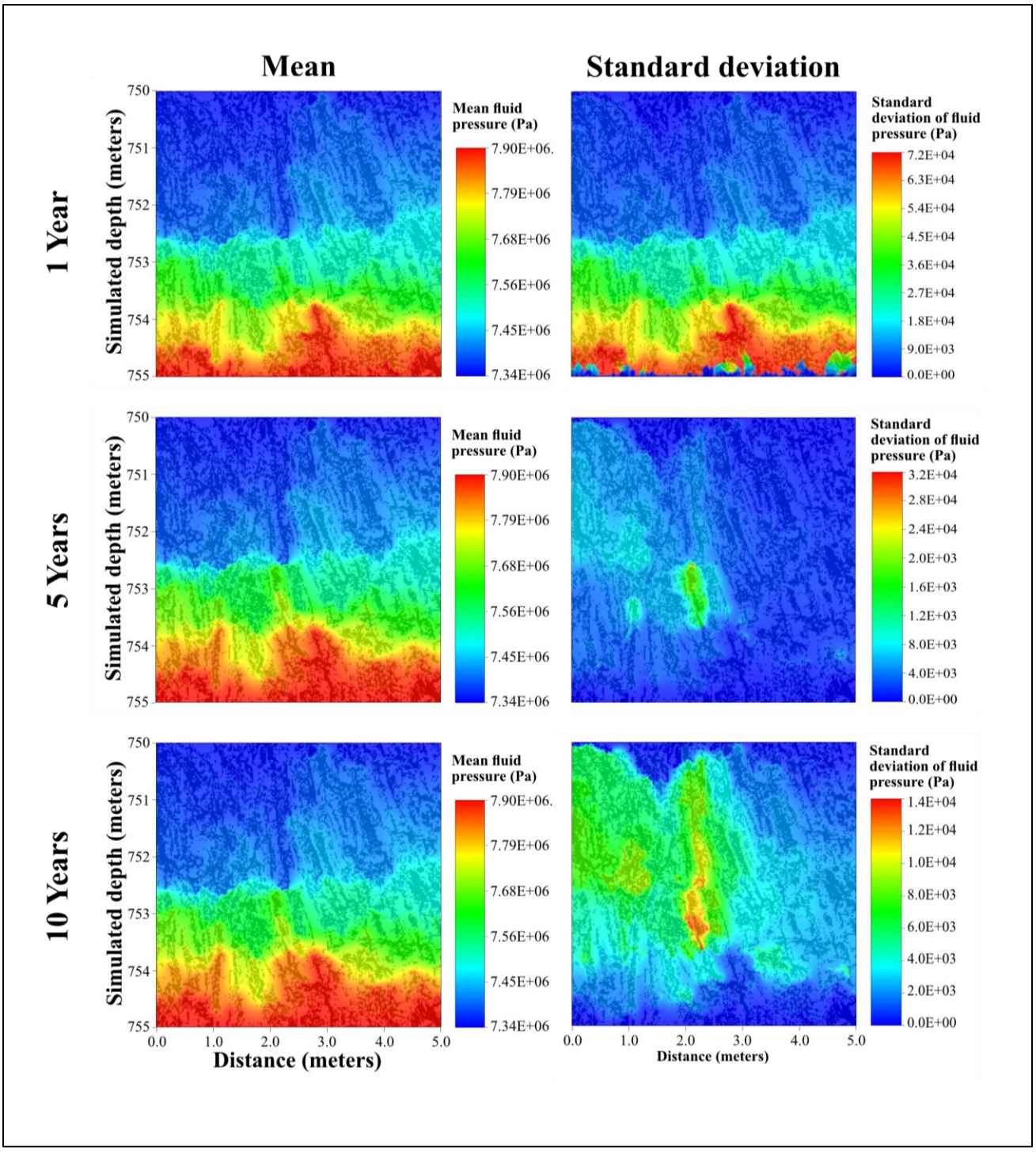

Figure 28: *Mean and standard deviation of fluid pressure at 1, 5, and 10 years. Mean shown on left, standard deviation on right.*

Recommendations for Future Work

Future work involving spatial fracture permeability uncertainty should attempt to refine model parameters in order to better understand the time-scales at which the types of variation demonstrated in this thesis are relevant. Additional future work should include the influence of chemical reactions at the time-scale of this experiment. The following section begins with a brief discussion of the model parameters most in need of refinement, including the mean value of fracture permeability at depths relevant to GCS, the permeability of the basalt matrix, and the relative permeability of 3-phase CO_2 in basalt fractures. It concludes with recommendations for including reactive chemistry in future models.

The first parameter used in this study that should be investigated further for future research is the mean value of fracture permeability in CRBG flow interiors at GCS reservoir depths. This thesis approximated that value using the best available data, by reversing a weighted geometric mean equation for effective permeability, using data from pump tests (effective permeability) and lab tests (matrix permeability). Measurements chosen for the equation, however, were selected from a range of values reported in literature. Literature values of matrix permeability ranged over several orders magnitude, as did literature values of effective permeability. Additionally, the weighting parameters for the weighted geometric mean equation were chosen based on the LiDAR-derived fracture maps, the development of which is partly a subjective process. As a result, there is considerable uncertainty in the mean value of fracture permeability used in this experiment, which could introduce differences between predicted and real leakage rates through the fracture network. If the real mean fracture permeability is higher than the one used in this study, leakage might occur much faster. This would affect confinement potential of CRB flow interiors, since slow leakage is desirable to allow time for mineralization of CO_2 to occur. Faster leakage would also allow CO_2 to reach the critical pressure at an earlier time, which would shift the leakage risks due to fluid pressure changes from late time, where CO_2 is more likely to have been trapped in minerals, to early time, where leakage risks are greatest. Conversely, if the actual mean value of fracture permeability in CRBG flow interiors is lower than the value predicted in this thesis, flow will proceed more slowly, and leakage through the fracture network would be highly unlikely on time-scales less than those required for CO_2 to be trapped in minerals. If the results of this study are to be used to in modeling real behavior of

3-phase CO_2 during GCS, better constraints should be placed on the value of mean fracture permeability at storage depths.

The second parameter used in this study that warrants more study is the permeability of the basalt matrix. As mentioned previously, measurements of CRBG matrix permeability found in the literature range over several orders of magnitude. In addition to affecting the value calculated for mean fracture permeability in this experiment, matrix permeability could alter the results by changing interactions between fractured and matrix cells. If matrix permeability were lower, CO_2 would not be able to pass through matrix cells, which it does at several points in the simulation grid used in this experiment. This would prevent CO_2 from fully penetrating the fracture network unless hydrofracturing or dissolution of the matrix block occurred, and simulating such an event would require a different code selection. If matrix permeability were higher, however, CO_2 would freely enter matrix blocks, resulting in less channelized, more homogeneous flow through the simulated flow interior layer.

The final parameter that should be refined for future work related to this study is the relative permeability of 3-phase CO_2 in basalt fractures, which is not currently well constrained. The data set used for curve matching in this experiment measures only the relative permeability of water and nitrogen gas in a basalt fracture, and thus provides an approximation of vapor phase CO_2 interactions with water, but does not provide good data on the relative permeability of supercritical liquid CO_2 and water. When matching curves for a 3-phase relative permeability model, it is desirable to have relative permeability data for all relevant phases (Parker et al 1987). A better curve match for the relative permeability model would allow better estimation of the phase interference and residual saturation values for the phases concerned, parameters that have been shown to influence CO_2 behavior at the reservoir scale (Pollyea 2016). Further constraints on phase interference and residual saturation would also refine the capillary pressure model, since these same parameters are also used in developing 3-phase capillary pressure curves (Parker et al 1987). Capillary pressure is highly important to predicting the behavior of CO_2 within a network, since it controls entry pressure, and thus the ability of CO_2 to enter a new cell.

In addition to parameter refinement, future work extending from this research should account for chemical reactions between CO_2 and basalt. This research has demonstrated that in the absence of chemical reactions, CO_2 can leak through a basalt network on the order of 10 years, but that leakage is influenced by the spatial distribution of fracture permeability.

Furthermore, it has shown that the permeability of cells at key points along the fracture path can have a disproportionate influence on fluid pressure. Since chemical reactions leading to the dissolution of basalt minerals and precipitation of carbonate minerals occur at time-scales shorter than 10 years (Schaef et al 2011, McGrail et al 2006, 2016, Matter et al 2016), permeability reduction and enhancement due to chemical reactions will have a large influence on CO_2 leakage though a basalt fracture network. Permeability alteration at key points, such as narrow fractures, will also influence the fluid pressure distribution during leakage, causing the phase change to occur shallower or deeper than would otherwise be expected. Results of such a model could then be used to inform reactive models at the reservoir scale, and thus better predict the confinement potential of CRBG rocks during GCS.

Conclusions

The goal of this research was to assess the effects of uncertainty in the spatial distribution of fracture permeability on the behavior of CO_2 as it leaks through a CRB flow entablature near the critical point of CO_2. To accomplish this, a Monte Carlo simulation was developed using LiDAR-derived fracture maps of a real outcrop in combination with a permeability distribution from the literature. Matrix cells on the fracture map were assigned a constant permeability based on laboratory tests, and fractured cells were randomly assigned a permeability value from a lognormal distribution based on fracture aperture values and pump test data. Through e-type analysis, the uncertainty introduced to the saturation of CO_2 and the fluid pressure within the model was assessed. Although uncertainty in fracture permeability has some effect on the spatial distribution of CO_2 within the fracture network, the effect is not large. The primary control on the path CO_2 travels through the network appears to be fracture geometry. Minor changes introduced by spatial variation in fracture permeability to the distribution of CO_2 within the network can, however, control the number of small, non-conducting fractures that CO_2 might enter. These fractures, while not globally connected, are important for storage of CO_2 through physical and chemical means. Spatial permeability uncertainty seems to have a larger effect on the distribution of fluid pressure, and thus the location of the phase transition from super-critical to sub-critical. Changes in overall distribution of fluid pressure, even in areas not conducting CO_2, have implications for the risk of hydrofracture, which could open new pathways for non-mineralized CO_2 to escape. At the outcrop scale, variability in fracture permeability generally governs the depth at which phase change occurs. This suggests that local grid refinement is likely necessary in site-scale numerical models of CO_2 sequestration when phase change is being taken into account. Moreover, this work implies that dual continuum representation of basalt flow interiors is likely necessary to account for dramatically different behavior in the basalt fractures and matrix.

References:

Adams, L.H., Gibson, R.E., 1926, The compressibilities of dunite and of basalt glass and their bearing on the composition of the earth: Proceedings of the National Academy of Sciences, v. 12, p. 275-283.

Ambrose, W.A., Lakshminarasimhan, S., Holtz, M.H., Núñez-López, V., Hovorka, S.D., Duncan, I., 2008, Geologic factors controlling CO_2 storage capacity and permanence: case studies in oil and gas reservoirs applied to CO_2 storage: Environmental Gology, v. 54, p. 1619-1633, doi: 10.1007/s00254-007-0940-2.

Aradóttir, E.S.P., Sonnenthal, E.L., Jónsson, H., 2012, Development and evaluation of a thermodynamic dataset for phases of interest in CO_2 mineral sequestration in basaltic rocks: Chemical Geology, v. 304-305, p. 26-38, doi: 10.1016/j.chemgeo.2012.01.031.

Aradóttir, E.S.P., Sonnenthal, E.L., Björnsson, G., Jónsson, H., Multidimensional reactive transport modeling of CO_2 mineral sequestration in basalts at the Hellisheidi geothermal field, Iceland: International Journal of Greenhouse Gas Control, v. 9, p. 24-40, doi: 10.1016/j.ijggc.2012.02.006.

Bachu, S., 2008, CO_2 storage in geologic media: Role, means, status, and barriers to deployment: Progress in Energy and Combustion Science, v. 34, p. 254-273, doi: 10.1016/j.pecs.2007.10.001.

Bachu, S., Bennion, B., 2008, Effects of in-situ conditions on relative permeability characteristics of CO_2-brine systems: Environmental Geology, v. 54, p. 1707-1722, doi: 10.1007/s00254-007-0946-9.

Bacon, D.H., Ramanathan, R., Schaef, H.T., McGrail, B.P., 2014, Simulating geologic co-sequestration of carbon dioxide and hydrogen sulfide in a basalt formation: International Journal of Greenhouse Gas Control, v. 21, p. 165-176, doi: 10.1016/j.ijggc.2013.12.012.

Baghbanan, A., Jing, L., 2006, Hydraulic properties of fractured rock masses with correlated fracture length and aperture: International Journal of Rock Mechanics and Mining Sciences, v. 44, p. 709-719, doi: 10.1016/j.ijrmms.2006.11.001.

Benito, P.H., Cook, P.J., Faybishenko, B., Freifeld, B., Doughty, C., 1999, Cross-well air-injection packer tests for the assessment of pneumatic connectivity in fractured, unsaturated basalt: Proceedings of the 37th U.S. Rock Mechanics Symposium, v. 2, p.843-850.

Bertels, S.P., DiCarlo, D.A., Blunt, M.J., 2001, Measurement of aperture distribution, capillary pressure, relative permeability, and in situ saturation in a rock fracture using computed tomography scanning: Water Resources Research, v. 37, no. 3, p. 649-662.

Burns, E.R., Morgan, D.S., Peavler, R.S., and Kahle, S.C., 2011, Three-dimensional model of the geologic framework for the Columbia Plateau Regional Aquifer System, Idaho, Oregon, and Washington: U.S. Geological Survey Scientific Investigations Report 2010-5246, 44 p., http://pubs.usgs.gov/sir/2010/5246.

Burns, E.R, Snyder, D.T, Haynes, J.V., and Waibel, M.S., 2012, Groundwater status and trends for the Columbia Plateau Regional Aquifer System, Washington, Oregon, and Idaho: U.S. Geological Survey Scientific Investigations Report 2012–5261, 52 p., http://pubs.er.usgs.gov/publication/sir20125261.

Burns, E.R., Williams, C.F., Ingebritsen, S.E., Voss, C.I., Spane, F.A., DeAngelo, J., 2015, Understanding heat and groundwater flow through continental flood basalt provinces: insights gained from alternative models of permeability/depth relationships for the Columbia Plateau, USA: Geofluids, v. 15, p. 120-138, doi: 10.1111/gfl.12095.

Camp, V.E., 1995, Mid-Miocene propagation of the Yellowstone mantle plume head beneath the Columbia River basalt source region: Geology, v.23, no. 5, p. 435-438.

Carneiro, J.F., 2009, Numerical simulations on the influence of matrix diffusion to carbon sequestration in double porosity fissured aquifers: International Journal of Greenhouse Gas Control, v. 3, p. 431-443, doi: 10.1016/j.ijggc.2009.02.006.

Clauser, C., Huenges, E., 1995, Thermal Conductivity of Rocks and Minerals: Rock Physics & Phase Relations: A Handbook of Physical Constants, p. 105-126, Ed. T. J. Ahrens. American Geophysical Union, Washington, DC.

Deutsch, C.V., Journel, A.G., 1998, GSLIB: Geostatistical Software Library and Resource Guide, 2nd Edition. New York: Oxford University Press.

Doughty, C., 2000, Numerical model of water flow in a fractured basalt vadose zone: Box Canyon site, Idaho: Water Resources Research, v. 36, no. 12, p. 3521-3534.

Doughty, C, Pruess, K., 2004, Modeling supercritical carbon dioxide injection in heterogeneous porous media: Vadose Zone Journal, v. 3, p. 837-847.

Durand, S.R., Sen, G., 2004, Preeruption history of the Grande Ronde Formation lavas, Columbia River Basalt Group, American Northwest: Evidence from phenocrysts: Geology, v. 32, no. 4, p. 293-296, doi: 10.1130/G20109.1.

Edlmann, K., Haszeldine, S., McDermott, C.I., 2013, Experimental investigation into the sealing capability of naturally fractured shale caprocks to supercritical carbon dioxide flow: Environmental Earth Science, v. 70, p. 3393-3409, doi: 10.1007/s12665-013-2407-y.

Eppelbaum, L., Kutasov, I., Pilchin, A., 2014, Chapter 2: Thermal properties of rocks and density of fluids p. 99-149 in Applied Geothermics, Springer-Verlag Berlin, Heidelberg, Germany.

Faybishenko, B., Witherspoon, P.A., Doughty, C., Geller, J.T., Wood, T.R., Podgorney, R.K., 2001, Multi-scale investigations of liquid flow in a fractured basalt vadose zone *in* Geophysical Monograph 42, Flow and Transport Through Unsaturated Fractured Rock, 2nd Edition: p. 161-182, American Geophysical Union, Washington, D.C.

Forbes, A.E.S., Blake, S., Tuffen, H., 2014, Entablature: fracture types and mechanisms: Bulletin of Volcanology, v. 76, 820, doi: 10.1007/s00445-014-0820-z.

Gale, J.E., 1987, Comparison of coupled fracture deformation and fluid flow models with direct measurements of fracture pore structure and stress-flow properties: 28th U.S. Symposium on Rock Mechanics, p. 1213-1222.

Garg, A., Shukla, P.R., 2009, Coal and energy security for India: Role of carbon dioxide (CO_2) capture and storage (CCS): Energy, v. 34, p. 1032-1041, doi: 10.1016/j.energy.2009.01.005.

Ge, S., 1997, A governing equation for fluid flow in rough fractures: Water Resources Research, v. 33, no. 1, p. 53-61.

Gephart, R.E., Price, S.M., Jackson, R.L., Myers, C.W., 1983, Geohydrologic factors and current concepts relevant to characterization of a potential nuclear waste repository site in Columbia River Basalt, Hanford site, Washington: Materials Research Society Symposia Proceedings, v. 26, p. 85-94.

Gislason, S.R., Broekecker, W.S., Gunnlaugsson, E., Snæbjörnsdóttir, S., Mesfin, K.G., Alfredsson, H.A., Aradöttir, E.S., Sigfusson, B., Gunnarsson, I., Stute, M., Matter, J.M., Anarson, M.Th., Galeczka, I.M., Gudbrandsson, S., Stockman, G., Wolff- Boenisch, D., Stefansson, A., Ragnheidardottir, E., Flaathen, T., Gysi, A.P., Olssen, J., Didriksen, K., Stipp, S., Menez, B., Oelkers, E.H., 2014, Rapid solubility and mineral storage of CO_2 in basalt: Energy Procedia, v. 63, p. 4561-4574, doi: 10.1016/j.egypro.2014.11.498.

Glass, R. J., Nicholl, M.J., Rajaram, H., Wood, T.R., 2003, Unsaturated flow through fracture networks: Evolution of liquid phase structure, dynamics, and the critical importance of fracture intersections: Water Resources Research, v. 39, p. 1352-1365, doi:10.1029/2003WR002015.

Guttikunda, S.K., Jawahar, P., 2014, Atmospheric emissions and pollution from coal-fired thermal power plants in India: Atmospheric Environment, v. 92, p. 449-460, doi: 10.1016/j.atmosenv.2014.04.057.

Hakami, E., 1995, Aperture distribution of rock fractures [Ph.D. Thesis]: Royal Institute of Technology, Stockholm, Sweden, 32p.

Hooper, P.R., Binger, G.B., Lees, K.R., 2002, Ages of the Steens and Columbia River flood basalts and their relationship to extension-related calc-alkalic volcanism in eastern Oregon: GSA Bulletin, v. 114, no. 1, p. 43-50.

Hou, Z., Rockhold, M.L., Murray, C.J., 2012, Evaluating the impact of caprock and reservoir properties on potential risk of CO_2 leakage after injection: Environmental Earth Science, v. 66, p. 2403-2415, doi: 10.1007/s12665-011-1465-2.

Hou, D., Benson, S.M., An experimental investigation of stress-dependent permeability and permeability hysteresis behavior in rock fractures, 2015, *in* Geophysical Monograph 210, Dynamics of fluids and transport in complex fractured-porous systems, p. 99-114.

IEA (2012) Energy technology perspectives. International Energy Agency, Paris

Jung, Y., Pau, G.S.H., Finsterle, S., Pollyea, R.M., *in press*, TOUGH3: A new efficient version of the TOUGH suite of multiphase flow and transport simulators: Computers & Geosciences, doi: 10.1016/j.cageo.2016.09.009.

Kahle, S.C., Morgan, D.S., Welch, W.B., Ely, D.M., Hinkle, S.R., Vaccaro, J.J., and Orzol, L.L., 2011, Hydrogeologic framework and hydrologic budget components of the Columbia Plateau Regional Aquifer System, Washington, Oregon, and Idaho: U.S. Geological Survey Scientific Investigations Report 2011–5124, 66 p.

Kapila, R.V., Haszeldine, R.S., 2009, Opportunities in India for carbon capture and storage as a form of climate change mitigation: Energy Procedia, v. 1, p. 4527- 4534, doi: 10.1016/j.egypro.2009.02.271.

Khaleel, R., 1989, Scale dependence of continuum models for fractured basalts: Water Resources Research, v. 25, no. 8, p. 1847-1855.

Khaleel, R., 1992, Equivalent porosity estimates for colonnade networks: Water Resources Research, v. 28, no. 10, p. 2783-2791.

Khaleel, R., 2001, Flow and transport parameters for colonnade networks, *in* Geophysical Monograph 42, Flow and Transport Through Unsaturated Fractured Rock, 2nd Edition: p. 151-160. American Geophysical Union, Washington D.C.

Klimczak, C., Schultz, R.A., Parashar, R., Reeves, D.M., 2010, Cubic law with aperture-length correlation: implications for network scale fluid flow: Hydrogeology Journal, v. 18, p. 851-862, doi: 10.1007/s10040-009-0572-6.

Konzuk, J.S., Kueper, B.H., 2004, Evaluation of cubic law based models describing single-phase flow through a rough-walled fracture: Water Resources Research, v. 40, 17 p., doi: 10.1029/2003WR002356.

Kumar, A., Noh, M., Pope, G.A., Sepehrnoori, K., Bryant, S., Lake, L.W., 2004, Reservoir simulation of CO_2 storage in deep saline aquifers: Society of Petroleum Engineers Fourteenth Symposium on Improved Oil Recovery, 10 p.

Kwicklis, E.M., Healy, R.W., 1993, Numerical investigation of steady liquid water flow in a variably saturated fracture network: Water Resources Research, v. 29, no.12, p. 4091-4102.

Lee, H.B., Yeo, I.W., Lee, K.K., 2013, The modified Reynolds equation for non-wetting fluid flow through a rough-walled rock fracture: Advances in Water Resources, v. 53, p. 242-249, doi: 10.1016/j.advwatres.2012.12.005.

Lindberg, J.W., 1989: A numerical study of cooling joint width and secondary mineral infilling in four Grande Ronde Basalt flows of the central Columbia Plateau, Washington, *in* Reidel, S.P., and Hooper, P.R., eds., Geological Society of America Special Paper 239, Volcanism and tectonism in the Columbia River flood-basalt province, p. 169-185. Geological Society of America, Boulder CO.

Long, P.E., 1978, Characterization and recognition of intraflow structures, Grande Ronde Basalt: Informal report, Rockwell International, Rockwell Hanford Operations, 80 p. Prepared for U.S. Department of Energy under contract EY-77-C-06-1030.

Long, P.E., Wood, B.J., 1986, Structures, textures, and cooling histories of Columbia River basalt flows: Geological Society of America Bulletin, v. 97, p. 1144-1155.

Long, J.C.S., Remer, J.S., Wilson, C.R., Witherspoon, P.A., 1982, Porous media equivalents for networks of discontinuous fractures: Water Resources Research, v. 18, no. 3, p. 645-658.

Magnuson, S.O., 1995, Inverse modeling for field-scale hydrologic and transport parameters of fractured basalt: Report, Lockheed Idaho Technologies Company, 64 p. Prepared for U.S. Department of Energy under contract DE-AC07-94ID13223.

Marini, L., 2007, Developments in Geochemistry 11: Geological Sequestration of Carbon Dioxide - Thermodynamics, Kinetics, and Reaction Path Modeling. Elsevier, Amsterdam Netherlands.

Matter, J.M., Takahashi, T., Goldberg, D., 2007, Experimental evaluation of *in situ* CO_2-water-rock reactions during CO_2 injection in basaltic rocks: Implications for geologic CO_2 sequestration: Geochemistry, Geophysics, Geosystems, v. 8, no. 2, doi: 10.1029/2006GC00147.

Matter, J.M., Stute, M., Snæbjörnsdottir, S.Ó., Oelkers, E.H., Gislason, S.R., Aradöttir, E.S., Sigfusson, B., Gunnarsson, I., Sigurdardottir, H., Gunnlaughsson, E., Axelsson, G., Alfredsson, H.A., Wolff-Boenisch, D., Mefsin, K., Fernandez de la Reguera Taya, D., Hall, J., Dideriksen, K., Broecker, W.S., 2016, Rapid carbon mineralization for permanent disposal of anthropogenic carbon dioxide emissions: Science, v. 352, p. 1312-1314).

McGrail, B.P., Schaef, H.T., Ho, A.M., Chien, Y.J., Dooley, J.J., Davidson, C.L., 2006, Potential for carbon dioxide sequestration in flood basalts: Journal of Geophysical Research, v. 111, 13 p., doi: 10.1029/2005JB004169.

McGrail, B.P., Sullivan, E.C., Spane, F.A., Bacon, D.H., Hund, G., Thorne, P.D., Thompson, C.J., Reidel, S.P., Colwell, F.S., 2009, Topical report – preliminary hydrogeologic characterization results from the Wallula basalt pilot study: Report, 357 p., prepared by Battelle for National Energy Technology Laboratory, Cooperative Agreement DE-FC26-05NT42587.

McGrail, B.P., Freeman, C.J., Beeman, G.H., Sullivan, E.C., Wurstner, S.K., Brown, C.F., Garber, R.D., Tobin, D., Steffensen, E.J., Reddy, S., Gilmartin, J.P., 2010, Final Scientific/Technical Report: Capture and Sequestration of CO_2 at the Boise White Paper Mill: Report, 61 p., prepared by Battelle for National Energy Technology Laboratory, Cooperative Agreement DE-FE0001992.

McGrail, B.P., Spane, F.A., Amonette, J.E., Thompson, C.R., Brown, C.F., 2014, Injection and monitoring at the Wallula basalt pilot project: Energy Procedia, v. 63, p. 2939-2948, doi: 10.1016/j.egypro.2014.11.316.

McGrail, B.P., Schaef, H.T., Spane, F.A., Cliff, J.B., Qafoku, O., Horner, J.A., Thomson, C.J., Owen, A.T., Sullivan, C.E., 2016, Field validation of supercritical CO_2 reactivity with basalts: Environmental Science and Technology Letters, doi: 10.1021/asc.estlett.6b00387.

Mokhtari, M., Tutunco, A.N., Boitnott, G.N., 2015, Intrinsic anisotropy in fracture permeability: Interpretation, v. 3, no. 3, 11 p., doi: 10.1190/INT-2014-0230.1.

Mortezaei, K., Vahedifard, F., 2015, Numerical simulation of induced seismicity in carbon capture and storage projects: Geotechnical and Geological Engineering, v. 33, p. 411-424, doi: 10.1007/s10706-015-9859-7.

Nichols, E.M., Weissmann, G.S., Wawrzyniec, F., Frecheitte, J.D., Klise, K.A., 2011, Processing of outcrop-based LIDAR imagery to characterize heterogeneity for groundwater models: SEPM concepts in Sedimentology and Paleontology No. 10, p. 239-247.

Nordqvist, A.W., Tsang, Y.W., Tsang, C.F., Dverstorp, B., Andersson, J., 1992, A variable aperture fracture network model for flow and transport in fractured rocks: Water Resources Research, v. 28, no. 6, p. 1703-1713.

Olsson, R., Barton, N., 2001, An improved model for hydromechanical coupling during shearing of rock joints: International Journal of Rock Mechanics & Mining Sciences, v. 38, p. 317-329.

Pascala, S., Socolow, R., 2004, Stabilization wedges: solving the climate problem for the next 50 years with current technologies: Science, v. 305, p. 968-972.

Parker, J.C., Lenhard, R.J., Kuppusamy, T., 1987, A parametric model for constitutive properties governing multiphase flow in porous media: Water Resources Research, v. 23, no. 4, p. 618-624.

Pollyea, R.M., Fairley, J.P., 2011, Estimating surface roughness of terrestrial laser scan data using orthogonal distance regression: Geology, v. 39, no. 7, p. 623-626, doi: 10.1130/G32078.1.

Pollyea, R.M., Fairley, J.P., 2012, Implications of spatial reservoir uncertainty for CO_2 sequestration in the east Snake River Plain, Idaho (USA): Hydrogeology Journal, v. 20, p. 689-699, doi: 10.1007/s10040-012-0847-1.

Pollyea, R.M., Fairley, J.P., Podgorney, R.K., Mcling, T.L., 2014, Physical constraints on a geologic CO_2 sequestration in low-volume basalt formations: Geological Society of America Bulletin, v. 126, p. 344-351, doi: 10.1130/B30874.1.

Pollyea, R.M., 2016, Influence of relative permeability on injection pressure and plume configuration during CO_2 injections in a mafic reservoir: International Journal of Greenhouse Gases, v. 46, p. 7-17, doi: 10.1016/j.ijggc.2015.12.025.

Prasad, P.S.R., Srinivasa Sarma, D., Sudhakar, L., Basavaraju, U., Singh, R.S., Begum, Z., Archana, K.B., Chavan, C.D., Charan, S.N., 2009, Geological sequestration of carbon dioxide in Deccan basalts: preliminary laboratory study: Current Science, v. 96, no. 2, p. 288-291.

Pruess, K., Oldenburg, C., Moridis, G., 1999, TOUGH2 User's Guide, Version 2.0: Report LBNL-43134, 210 p.

Pruess, K., 2005, Numerical simulations show potential for strong nonisothermal effects during fluid leakage from a geologic disposal reservoir for CO_2 *in* Geophysical Monograph Series 162, Dynamics of Fluids and Transport in Fractured Rock: p. 81-89, American Geophysical Union, Washington D.C.

Pruess, K., 2011, ECO2M: A TOUGH2 Fluid Property Module for Mixtures of Water, NaCl, and CO_2, Including Super- and Sub-critical Conditions, and Phase Change Between Liquid and Gaseous CO_2. Report LBNL-4590E, 93 p.

Ramos, F.C., Wolff, J.A., Tollstrup, D.L., 2005, Sr isotope disequilibrium in Columbia River flood basalts: Evidence for rapid shallow-level open-system processes: Geology, v. 33, no. 6, p. 457-460, doi: 10.1130/G21512.1.

Reidel, S.P., Camp, V.E., Tolan, T.L., Martin, B.S., 2013, The Columbia River flood basalt province: Stratigraphy, areal extent, volume, and physical volcanology, *in* Reidel, S.P., Camp, V.E., Ross, M.E., Wolff, J.A., Martin, B.S., Tolan, T.L, and Wells, R.E., eds., The Columbia River Flood Basalt Province: Geological Society of America Special Paper 497, p. 1–43, doi:10.1130/2013.2497(01).

Reidel, S.P., 2015, Igneous Rock Associations 15. The Columbia River Basalt Group: A flood basalt province in the Pacific Northwest, USA: Geoscience Canada, v. 42, no. 1, p. 151-168.

Renshaw, C.E., 1995, On the relationship between mechanical and hydraulic apertures in rough-walled fractures: Journal of Geophysical Research, v. 100, no. B12, p. 24629-24636.

Rosenbauer, R.J., Thomas, B., Bischoff, J.L., Palandri, J., 2012, Carbon sequestration via reaction with basaltic rocks: Geochemical modeling and experimental results: Geochemica et Cosmochemica Acta, v. 89, p. 116-133, doi: 10.1016/j.gca.2012.04.042.

Sagar, B., Runchal, A., 1982, Permeability of fractured rock: Effect of fracture size and data uncertainties: Water Resources Research, v. 18, no. 2, p. 266-274.

Schaef, H.T., McGrail, B.P., Owen, A.T., 2011, Basalt reactivity variability with reservoir depth in supercritical CO_2 and aqueous phases: Energy Procedia, v. 4, p. 4977-4984.

Spane, F.A., Webber, W.D., 1995, Hydrochemistry and hydrogeologic conditions within the Hanford site upper basalt confined aquifer system. Report, 78 p., prepared for the U.S. Department of Energy at Pacific National Laboratory under contract DE-AC06-76RLO 1830.

Spane, F.A., McGrail, B.P., Sullivan, E.C., Goldberg, D.S., McLing T.L., Weeks, R.S., Smith, R.W., 2007, Field Activity Plan: Characterization test for CO_2 sequestration in the Columbia River Basalt Group. Report, 33 p., prepared for Big Sky Regional Carbon Partnership under contract 49051 with Battelle Pacific Northwest Division.

Spycher, N., Pruess, K., 2005, CO_2-H_2O mixtures in the geologic sequestration of CO_2. II. Partitioning in chloride brines at 12-100 °C and up to 600 bar, Geochemica et Cosmochima Acta, v. 69, no.13, p. 3309-3320, doi: 10.1016/j.gca.2005.01.015.

Stone, H.L., 1970, Probability model for estimating three-phase relative permeability: Journal of Petroleum Technology, v. 22, no. 2, p. 214-218.

Strait, S.R., Spane, F.A., Jackson, R.L., Pidcoe, W.W., 1982., Hydrologic testing methodology and results from deep basalt boreholes. RHO-BW-SA--189, Rockwell Hanford Operations, Richland, Washington.

Sullivan, E.C., Hardage, B.A., McGrail, B.P., Davis, K.N., 2011, Breakthroughs in seismic and borehole characterization of basalt sequestration targets: Energy Procedia, v. 4, p. 5615-5622, doi: 10.1016/j.egypro.2011.02.551.

Takaya, Y., Nakamura, K., Kato, Y., 2013, Geological. Geochemical and social-scientific assessment of basaltic aquifers as potential storage sites for CO_2: Geochemical Journal, v. 47, p. 385-396.

Tsang, Y.W., Tsang, C.F., 1987, Channel model of flow through fractured media: Water Resources Research, v. 23, no. 3, p. 467-479.

Unger, A.J.A., Faybishenko, B., Bodvarsson, G.S., Simmons, A.M., 2004, Simulating infiltration tests in fractured basalt at the Box Canyon Site, Idaho: Vadose Zone Journal, v. 3, p. 75-89.

United States Geological Survey, 2013, National Assessment of Geologic Carbon Dioxide Storage Resources – Summary. Fact Sheet 2013-3020, Version 1.1.

Van Genuchten, M.T., 1980, A closed-form equation for predicting the hydraulic conductivity of unsaturated soils: Soil Science Society of America Journal, v. 44, p. 892-898.

Vialle, S., Druhan, J.L., Maher, K., 2016, Multi-phase flow simulation of CO_2 leakage through a fractured caprock in response to mitigation strategies: International Journal of Greenhouse Gas Control, v. 44, p. 11-25, doi: 0.1016/j.ijggc.2015.10.007.

Viebahn, P., Höller, S., Vallentin, D., Liptow, H., Villar, A., 2011, Future CCS implementation in India: a systematic and long-term analysis: Energy Procedia, v. 4, p. 2708-2715, doi: 10.1016/j.egypro.2011.02.172.

Vye-Brown, C., Self, S., Barry, T.L., 2013, Architecture and emplacement of flood basalt flow fields: case studies from the Columbia River Basalt Group, NW USA: Bulletin of Volcanology, v. 75, 21 p., doi: 10.1007/s00445-013-0697-2.

Wang, L., Cardenas, M.B., Slottke, D.T., Ketcham, R.A., Sharp, J.M., 2015, Modification of the Local Cubic Law of fracture flow for weak inertia, tortuosity, and roughness: AGU Publications, Water Resources research article 10.1002/2014WR015815.

Witherspoon, P.A., Wang, J.S.Y., Iwai, K., Gale, J.E., 1980, Validity of Cubic Law for fluid flow in a deformable rock fracture: Water Resources Research, v. 16, no. 6, p. 1016-1024.

Wood, W.W., Fernandez, L.A., 1988, Volcanic Rocks *in* Back, W., Rosenshein, J.S., and Seaber, P.R., eds., Hydrogeology: Boulder, Colorado, Geological Society of America, The Geology of North America, v. O-2.

Wood, T.R., Glass, R.J., McJunkin, T.R., Podgorney, R.K., Laviolette, R.A., Noah, K.S., Stoner, D.L., Starr, R.C., Baker, K., 2004, Unsaturated flow through a small fracture-matrix network: Part 1. Experimental observations: Vadose Zone Journal, v. 3, p. 90-100.

Z+F Laser (n.d.), Z+F Imager 5010x [Fact Sheet]. Retrieved from: http://www.zf-laser.com/fileadmin/editor/Datenblaetter/Z_F_IMAGER_5010X_System_Requirements_E_FINAL.pdf.

Zoller + Fröhlich (Z+F). 2014. Z+F LaserControl Manual v.8.6, Wangen im Allgäu, Germany.

Zakharova, N.V., Goldberg, D.S., Sullivan, E.C., Herron, M.M., Grau, J.A., 2012, Petrophysical and geochemical properties of the Columbia River flood basalt: Implications for carbon sequestration: Geochemistry Geophysics Geosystems, v. 13, no. 11, 22 p., doi: 10.1029/2012GC004305.

Zhou, Q., Salve, R., Liu, H., Wang, J.S.Y., Hudson, D., 2006, Analysis of a mesoscale infiltration and water seepage test in unsaturated fractured rock: Spatial variables and discrete fracture patterns: Journal of Contaminant Hydrogeology, v. 87, p. 96-122, doi: 10.1016/j.jconhyd.2006.05.001.

Zimmerman, R.W., Bodvarsson, G.S., 1996, Hydraulic conductivity in rock fractures: Transport in Porous Media, v. 23, p. 1-30.

Zoback, M.D., Gorelick, S.M., 2012, Earthquake triggering and large-scale geologic storage of carbon dioxide: Proceedings of the National Academy of Sciences, v. 109, no. 26, p. 10164-10168, doi: 10.1073/pnas.1202473109.

Appendix A: Scripts

Script 1: dualk.sh

```
#! /bin/bash

# Putting binary rock id's into TOUGH3 mesh
# A.O. Gierzynski, Virginia Tech Geosciences 2016
# Version 2016 03 04
        # 2016 03 28
        # 2016 03 29
        # 2016 05 10

sed -n '/A11 1   /,/LH1 2   /p' MESH.meshm > ELEME
# INPUT FIRST AND LAST ELEMENT ID

awk 'NR>9 {print $1, $2, $3, $7}' 15b6c.bin > box.tmp
# INPUT BINARY FILE NAME IN ABOVE LINE

awk '{print $1+6, $2, $3-10, $4}' box.tmp | sort -k1n -k3rn > sort.tmp
# INPUT -MINX for $1, -MAXZ for $3

awk '{print $4}' sort.tmp > bin.tmp

sed -i 's/\-9999/1/' bin.tmp

sed -e 's/0/BASLT/' -e 's/1/FRACT/' bin.tmp > rocks.tmp

paste -d, ELEME rocks.tmp | sed -e '/BASLT/s/    1/BASLT/' -e '/FRACT/s/    1/FRACT/' |
sed -e 's/,BASLT//' -e 's/,FRACT//' > repl.tmp

sed -n '/^ /,$p' MESH.meshm > CONNE
```

```
cat repl.tmp CONNE > MESH.tmp

sed -i '1i\'"ELEME0  NX= 200  NY=   1  NZ= 200" MESH.tmp

#sed -e '/-0\.01250/s/BASLT/BOUND/' -e '/-0\.01250/s/FRACT/BOUND/' MESH.tmp >
MESH.new

#sed -i '/BOUND/s/E-04/E+50/' MESH.new

#rm *.tmp ELEME CONNE

exit 0
```

Script 2: iperm.py

```
#! /usr/bin/python3

# Alec O Gierzynski
# Rev0 feb16 2016
# Rev1 feb23 2016
# Rev3 apr05 2016
# Rev4 apr19 2016
# Rev5 sep02 2016

# GENERATING PERMEABILITY MODIFIERS (PERMX) FOR USE IN TOUGH3
FROM RANDOMLY GENERATED APERTURE WIDTH POPULATIONS WITH
KNOWN STATISTICAL PROPERTIES BASED ON REAL SAMPLES

# INPUTS:
      # log(mean) in mm
      # log(standard deviation) in mm
      # desired population size - input on command line, ie ./iperm.py N
# OUTPUTS:
            # pmx.dat: file containing N random permeability modifiers such  that k(rand) =
            PMX*uk(rand)
      # b.dat: file containing random aperture values in m
      # stats.txt: text file containing mean, standard deviation, N, minimum, and
maximum for aperture width (m), permeability (m^2), and       PMX (m)

import numpy as np
import statistics as stats
import csv
import sys
```

```
arg1 = sys.argv[1]
N = []
N.append(float(arg1))
apps = np.random.lognormal(-1.945, 0.896, N[0])
appy = np.array(apps)
b = apps/1000
# Generate lognormal sample with known properties - input=(logmean, logstdev, N) also converts width from mm to m

ub = stats.mean(b)
sdb = stats.stdev(b)
Nb = np.count_nonzero(b)
minb = np.amin(b)
maxb = np.amax(b)
# Generate and store mean (ub), stdev (sdb), N (Nb), min (minb), and max (maxb) for the random aperture population

bsq = np.power(b, 2)
k = bsq/12
# Convert random aperture width (m) to random permeability values (m^2) using equation k = (b^2)/12

uk = stats.mean(k)
sdk = stats.stdev(k)
Nk = np.count_nonzero(k)
mink = np.amin(k)
maxk = np.amax(k)
# Generate and store mean (uk), stdev (sdk), N (Nk), min (mink) and max (maxb) for random permeability population

lnk = np.log(k)
```

```
meanlnk = stats.mean(lnk)
geomeank = np.exp(meanlnk)
# Creates arrays of ln(b, k, PMX) and normalizes them

PMX = k / uk
# Converts k valuse to PMX, permeability modifier in TOUGH3, where PMX = k/kmean

uPMX = stats.mean(PMX)
sdPMX = stats.stdev(PMX)
NPMX = np.count_nonzero(PMX)
minPMX = np.amin(PMX)
maxPMX = np.amax(PMX)
# Generates and stores stats for PMX population

labels= ['ub', 'sdb', 'Nb', 'minb', 'maxb', 'uk', 'sdk', 'Nk', 'mink', 'maxk', 'uPMX', 'sdPMX',
'NPMX', 'minPMX', 'maxPMX', 'geomeank']
stats= [ub, sdb, Nb, minb, maxb, uk, sdk, Nk, mink, maxk, uPMX, sdPMX, NPMX,
minPMX, maxPMX, geomeank]
zip(labels, stats)
with open('stats.csv', 'w') as m:
    writer = csv.writer(m)
    writer.writerows(zip(labels, stats))
m.close()
# Generates a file containing stats for aperture (m) permeability (m^2), and PMX (m)
populations

np.savetxt('pmx.dat', np.c_[PMX], fmt = '%1.4E')
# Makes file pmx.dat containing N PMX values


exit(0)
```

Script 3: p3rmsh.sh

NOTE: con.inj file referred to in script is a text file containing 200 connections, those between the constant CO_2 overpressure cell at the base and the bottom row of cells. Created separately using sed and awk.

```
#! /bin/bash

# Putting permeability modifiers into TOUGH3 mesh
# A.O. Gierzynski, Virginia Tech Geosciences 2016
# Version 2016 03 04
      # 2016 03 28
      # 2016 03 29
      # 2016 05 10
      # 2016 05 19
      # 2016 05 24
      # 2016 06 23
# INPUTS:
     # MESH, binary roughness file, con.inj and iperm.py must be in
present working directory
          # Must manually input name of binary roughness file in line 5 of          code
# OUTPUTS:
     # MESH.new - MESH file with PERMX values in proper positions


sed -n '/ELEME/,/^ /p' MESH > ELEME

sed -i 's/    1/ROCKS/' ELEME

awk '{print $1, $2}' ELEME | sed 's/ROCKS.*//' | sed '1d' > elids.tmp
```

```
sed -n '/ROCKS/p' ELEME | cut -c 16-80 > ELEME.tmp

awk 'NR>9 {print $1, $2, $3, $7}' 15b6c.bin > box.tmp
# INPUT BINARY FILE NAME IN ABOVE LINE

awk '{print $1+6, $2, $3-10, $4}' box.tmp | sort -k1n -k3rn > sort.tmp
# INPUT -MINX for $1, -MAXZ for $3

awk '{print $4}' sort.tmp | sed 's/\-9999/1/' | sed -e 's/0/BASLT/' -e 's/1/FRACT/' >
rocks.tmp

N=$(grep -c 'FRACT' rocks.tmp)

./iperm.py $N

paste -d, ELEME.tmp rocks.tmp | sed -e '/BASLT/s/ROCKS/BASLT/' -e
'/FRACT/s/ROCKS/FRACT/' | sed -e 's/,BASLT//' -e 's/,FRACT//' > repl.tmp

grep 'FRACT' repl.tmp > fract.tmp

grep 'BASLT' repl.tmp > baslt.tmp

paste -d, fract.tmp pmx.dat | sed 's/,/ /' > fmods.tmp

awk '{print $1, $5, $2, $3, $4}' fmods.tmp > mfract.tmp

sed -i 's/          /     0     /' baslt.tmp

cat baslt.tmp mfract.tmp | sort -k3n -k5rn > bfsort.tmp

sed -i 's/     0     /XXXXXXXXXX/' bfsort.tmp
```

```
sed -i 's/XXXXXXXXXX/1.0000E+00  /' bfsort.tmp

sed -i '/FRACT/s/ /     /g' bfsort.tmp

sed -e '/FRACT/s/     //' -e '/BASLT/s/ //' bfsort.tmp > FIX.tmp

sed -i '/BASLT/s/        /          /' FIX.tmp

sed -e '/FRACT/s/     /   /' -e '/FRACT/s/     /   /' FIX.tmp > 2FIX.tmp

sed -i '/FRACT/s/     /  /' 2FIX.tmp

paste -d, elids.tmp 2FIX.tmp | sed -e 's/ ,/          /' -e 's/,/          /' > ELEME.fr

sed -n '/CONNE/,$p' MESH > CONNE

sed -i '79602d' CONNE

cat ELEME.fr CONNE con.inj  > MESH.tmp

sed -i '1i\"'ELEME----1----*----2----*----3----*----4----*----5----*----6----*----7----*----8"
MESH.tmp

sed -i '40002i\"'INJ00          INJCT0.3125E+500.0000E+001.0000E+00   2.48750
0.01250  -5.01250" MESH.tmp

sed -e '/-0\.01250/s/BASLT/BOUND/' -e '/-0\.01250/s/FRACT/BOUND/' MESH.tmp >
MESH.new

sed -i '/BOUND/s/E-04/E+50/' MESH.new
```

```
rm *.tmp ELEME CONNE ELEME.fr

exit 0
```